UNIVERSITY OF CALIFORNIA

Los Angeles

Patient-Specific Hemodynamic Modeling of Cerebral Blood Flow: 1-D Mathematical Model

A dissertation submitted in partial satisfaction

of the requirements for the degree

Doctor of Philosophy in Mechanical Engineering

by

Jingyi Kang

2023

ABSTRACT OF THE DISSERTATION

Patient-Specific Hemodynamic Modeling of Cerebral Blood Flow: 1-D Mathematical Model

by

Jingyi Kang
Doctor of Philosiphy in Mechanical Engineering
University of California, Los Angeles, 2023
Professor Jeff D. Eldredge, Chair

Ischemic stroke is one of the leading causes of death in the US. It is estimated that intracranial stenosis, which refers to the narrowing of the blood vessels within the brain, accounts for 30% - 50% of ischemic strokes. Typical intracranial stenosis includes narrowing of arteries such as the middle cerebral artery (MCA) and the internal carotid artery (ICA). Among all types of intracranial stenosis, middle cerebral artery (MCA) stenosis poses a higher risk for ischemic stroke. Collateral circulation occurs when occlusion happens and plays a vital role in sustaining cerebral blood flow during ischemic strokes. However, the factors leading to the formation of collateral circulation remain unclear and are difficult to observe through image data alone. The imaging data provides only a snapshot, thereby limiting our understanding of stenosis development and the formation of collateral circulation. This work developed a computational tool that integrates patient-specific image data with fluid dynamics to investigate the development of MCA stenosis and explore possible causes of collateral circulation between MCA and PComm.

The hemodynamic data of arterial segments is extracted from individual computed tomography angiography (CTA) scan. The extracted network includes parent arterial segment ICA and daughter arterial segments MCA, ACA and PComm. The inlet blood flow profile

is calibrated using color-coded duplex ultrasound from young, healthy volunteers, while a three-element Windkessel outlet boundary condition is attached to the end of each daughter arterial segment to simulate artificial wave reflection from the downstream vascular network. Our findings demonstrate that increases in area reduction increase the pressure of the unobstructed pathway and decrease the pressure of the obstructed pathway, which becomes significant after 90% of the MCA area is occluded, aligning with clinical observations. Wave Intensity Analysis (WIA) results reveal that the forward expansion wave (FEW) accelerates the pressure and blood flow from the downstream vascular network, particularly when MCA is highly occluded (90% cross-sectional area is occluded). The pressure/blood flow and WIA results show that the formation of collateral circulation is closely related to the high resistance of the upstream large artery, which aligns with the clinical hypothesis.

Furthermore, this work compares the two types of outlet boundary conditions: the three-element Windkessel 0-D outlet boundary condition and the 1-D binary tree outlet boundary condition. To assess their impact on the pressure and blood flow waveform of the upstream large artery, both types of outlet boundary conditions are connected to the upstream large artery. The findings reveal that the two types of outlet boundary conditions exhibit minimal differences in affecting the pressure/blood flow of upstream large artery. However, it should be noted that the utilization of the 1-D outlet boundary conditions is limited in the presented model due to the long-wave approximation.

This work introduces a novel model that includes one parent arterial segment connected to three daughter arterial segments. It is the first time that the collateral circulation between MCA and PComm through the downstream vascular network is investigated. Additionally, the WIA method is employed for the first time to study the relationship between MCA stenosis and the formation of collateral circulation.

In summary, a computational tool is developed to understand the evolution of hemodynamic changes in cerebral blood flow and to reveal pathology of collateral circulation and MCA

stenosis.

The dissertation of Jingyi Kang is approved.

David S. Liebeskind

Ann R. Karagozian

Xiaolin Zhong

Tyler R. Clites

Jeff D. Eldredge, Committee Chair

University of California, Los Angeles

2023

TABLE OF CONTENTS

LIST OF FIGURES

LIST OF TABLES

LIST OF SYMBOLS

Symbols	Description	Units
q	blood flow rate	cm^3/s
P	blood pressure	mmHg
P_0	blood pressure of undeformed vessel wall	mmHg
A	vessel cross-sectional area	cm^2
A_p/A_d	parent /daughter vessel cross-sectional area	cm^2
A_0	cross-sectional area of undeformed vessel wall	cm^2
r	vessel radius	cm
r_p/A_d	parent/daughter vessel radius	cm
r_0	vessel radius of undeformed vessel wall	cm
δ	boundary layer of blood flow	cm
h	vessel wall thickness	cm
E	young's modulus of vessel wall	$\mathrm{g\,cm/s}^2$
ρ	blood flow density	$\mathrm{g/cm}^3$
ν	kinematic viscosity	cm^2/s
R_1	first resistance of 0-D outlet boundary condition	$\mathrm{g/cm\,s}^4$
R_2	second resistance of 0-D outlet boundary condition	$\mathrm{g/cm\,s}^4$
C_t	compliance of 0-D outlet boundary condition	$\mathrm{cm}^4\mathrm{s}^2/\mathrm{g}$
$\bar{Z}$	impedance in frequency domain	N/A
$\tilde{z}$	impedance in time domain	N/A

Symbols	Description	Units
c	wave speed	$\mathrm{cm\,s^{-1}}$
C	compliance of vessel wall	$\mathrm{cm\,s^2/g}$
μ	blood flow viscosity	$\mathrm{g/cm\,s}$
l_{rr}	length-to-radius ratio of 1-D outlet boundary condition	N/A
α	Womersley number	N/A
T	time period	s
ω	angular velocity	rad/s
dI_+/dI_-	positive/negative wave intensity	$\mathrm{W/m^2}$
k_v	viscous loss	N/A
k_u	inertial force loss	N/A
k_t	turbulence loss	N/A
A_P	unobstructed vessel cross-sectional area of stenosis model	$\mathrm{cm^2}$
A_s	obstructed vessel cross-sectional area of stenosis model	$\mathrm{cm^2}$
r_P	unobstructed vessel radius of stenosis model	cm
r_s	obstructed vessel radius of stenosis model	cm
L_s	stenosis length	cm

ACKNOWLEDGMENTS

I am really grateful and would like to express my sincere gratitude to the following individuals and organizations who have contributed significantly to the completion of this dissertation.

I am profoundly grateful to Prof. Jeff Eldredge for his unwavering support and invaluable guidance throughout my journey in completing this PhD thesis. Also, I really appreciate him for providing me with the opportunity to collaborate with the foremost researchers in the world. I am deeply appreciative of Prof. David Liebeskind for their invaluable mentorship, which not only guided me to explore the intricate realm of collateral circulation but also illuminated a fascinating area for me to pursue in my doctoral research.

Additionally, my heartfelt gratitude goes to my thesis committee members: Prof. Ann Karagozian, Prof. Xiaolin Zhong, and Prof. Tylor Clites, for their invaluable insights and constructive suggestions that have significantly enriched the content of my Ph.D. thesis. I am particularly indebted to Prof. Ann Karagozian for her course, which provided a robust bedrock for my subsequent Ph.D. endeavors. Likewise, I extend my sincere appreciation to Prof. Xiaolin Zhong for imparting a strong foundational understanding of computational fluid dynamics through his courses.

To my cherished family, your encouragement, boundless patience, and understanding have served as a constant wellspring of motivation. Your unwavering support has played an indispensable role in guiding me through the intricate pathways of this demanding academic journey.

Also, I would like to express my sincere gratitude to Prof. Steve Bennoun and Prof. Matteo Pellegrini. I would like to extend my appreciation to Prof. Niema Pahlevan for illuminating

the realm of cardiovascular physics of fluids and sparking a deep and lasting enthusiasm for this field within me.

For my personal growth throughout this journey, I am really appreciate this opportunities and experience that have shaped and molded me in the past several years.

VITA

2011.9 - 2015.7	**B.S.** in Vehicle Engineering
	SouthWest Jiaotong University, Chengdu
2016.1 - 2017.12	**M.S.** in Mechanical Engineering
	University of Southern California, Los Angeles
2018.9 - 2023.9	**Ph.D.** in Mechanical Engineering
	University of California, Los Angeles

Chapter One

Introduction

1.1 Cerebral Blood Flow Modeling: Motivation

Cardiovascular disease (CVD) is one of the leading causes of death around worldwide [1]. In 2019, nearly one-third of deaths in the United States were attributed to CVD. Among all types of CVD, stroke emerges as the third most common cause of fatality [2]. Also, it is the leading cause of severe and long-term disabilities within the United States. 87% of stroke is ischemic stroke, resulting from either thrombosis or arterial embolism that obstructs brain arteries [2]. The primary causes of ischemic stroke include narrowing head and neck arteries and general hypoperfusion. It has been estimated that intracranial stenosis may contribute to 30% - 50% of ischemic strokes and middle cerebral artery (MCA) stenosis have a higher risk of ischemic stroke among intracranial artery stenosis [3].

Collateral circulation refers to the alternative pathway that maintains residual blood flow to the brain when a large artery is blocked [4]. It plays a pivotal role in the pathophysiology of cerebral ischemia [5]. The formation of collateral circulation is crucial if the patients recover from cerebral ischemia. However, due to the limitations of image processing techniques, the collateral circulation vessel network cannot be extracted directly from medical images. Moreover, the cause of the formation of collateral circulation channels remains unknown.

Computational methods have emerged as powerful tools in hemodynamic simulation, enabling the prediction of blood flow, pressure, and vessel deformation, as well as the inves-

tigation of cerebrovascular diseases. A sophisticated and accurate numerical method is in demand for disease application, surgical planning, and medical device design. This work employs various computational methods in fluid dynamics to uncover the underlying pathology of diseases.

We aim to investigate the collateral circulations when MCA is occluded using computational methods in fluid dynamics. Also, two types of outflow boundary conditions are discussed in this work and connected to the upstream large artery to provide wave reflections originating from the downstream vascular network.

1.2 Cerebral Artery: Background

1.2.1 Circle of Willis (CoWs)

The circulation of the brain was first described by Thomas Willis in 1664, named after Willis, which is called the Circle of Willis (CoWs). The CoWs is the joining area of several large arteries. The two internal carotid arteries (ICA) and the vertebral arteries (VB) supply the oxygenated blood through the COWs, where ICA supplies 80% of the cerebral blood flow and VB supplies 20% of the cerebral blood flow [6]. The two vertebral arteries come together intracranially in the basilar artery (BA). The CoWs begin to form when the two internal carotid arteries (ICA) enter the cranial cavity and they branch into two main branches: the anterior cerebral arteries (ACA) and the middle cerebral artery (MCA) [7]. Two ACA are connected by the anterior communicating artery (ACom), which is a "connecting vessel". The posterior cerebral arteries (PCA) are the terminal branches of the VB. PCAs connect the MCAs at the same side and ICAs via the posterior communicating artery (PComm). The PComm connects to the ICAs and MCAs anteriorly and communicates with the PCA posteriorly. The two systems, ICAs and PCAs, supply the blood to the brain, and they are connected by the PComm. Figure 1.1 demonstrates the structure of CoWs.

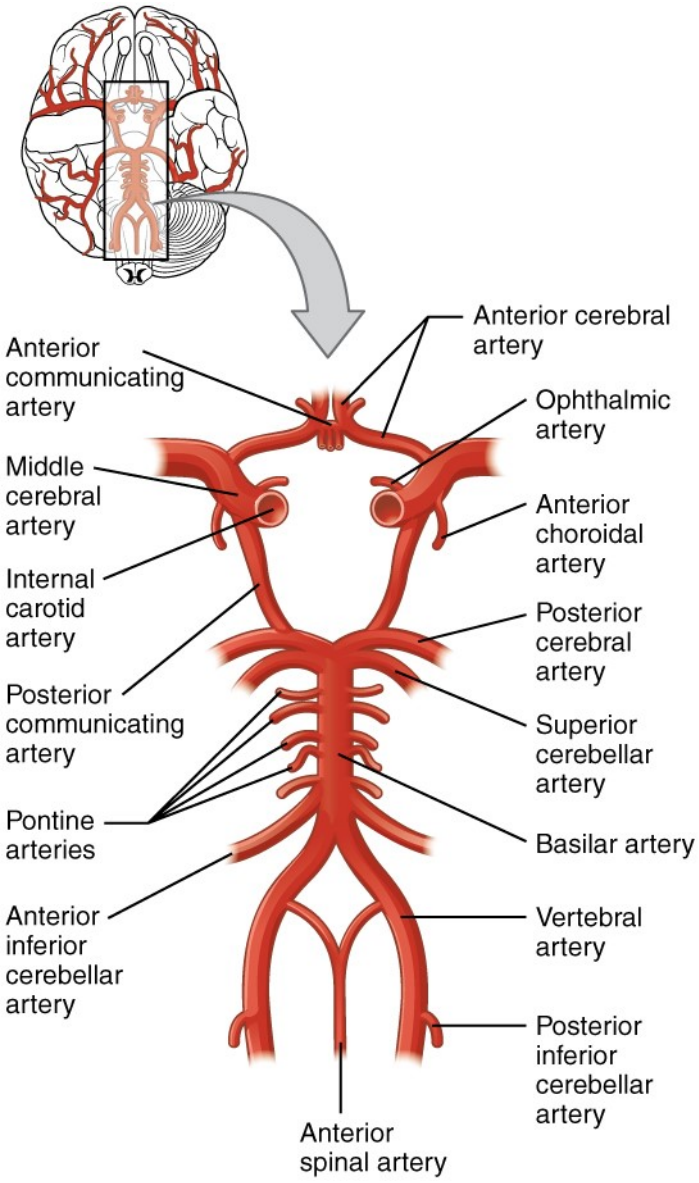

Figure 1.1 Schematic of Circle of Wills [8]

1.2.2 Collateral Circulation

Collateral circulation refers to an alternative pathway that develops around a blocked artery, which is not present in a healthy brain. The exact mechanisms behind collateral circulation formation remain unclear, but they are believed to be closely related to high vascular resistance and ischemic conditions [5].Nevertheless, the existence of collateral circulation has

been well-documented and can be clearly observed through CTA scans. Moreover, collateral circulation can explain why many patients can survive and completely recover from occlusive cerebral vascular disease [9].

There are many channels for collateral circulation and they are commonly divided into primary and secondary collateral pathways. Primary collaterals include the arterial segments of the circle of Willis (CoWs), whereas the ophthalmic artery and leptomeningeal vessels constitute secondary collaterals [5].

The CoWs is a ring-like structure at the base side of the brain, which also serves as a backup system for collateral circulation. When the artery supporting the CoWs is blocked or narrowed, the system preserves cerebral perfusion to prevent the occurrence of ischemia [6]. This system provides primary collaterals in the cerebral circulation and it includes AComm (communication arteries and part of CoWs), PComm (communication arteries and part of CoWs), and ophthalmic artery via external carotid artery [10]. For primary collaterals, the most often occurring communication is between the anterior and MCA via AComm and between the posterior and MCA via PComm. For healthy brains, there is no net flow of blood across the PComm and AComm [10]. However, to maintain patency and prevent thrombosis, there is to- and fro-flow of blood inside the PComm and AComm. The primary collaterals appear when a pressure gradient develops between large arteries connected to the PComm and AComm. This work focuses on the primary collateral circulation between the posterior and MCA via PComm.

When cerebral arterial is occluded, systemic blood pressure may need to be increased to augment collateral blood flow. If primary collateral pathways are not available, either because of the patient's anatomy (such as lack of right ICA) or because of therapeutic intervention, secondary collaterals are available that bridge adjacent major vascular territories. These pathways are known as the pia-to-pia collateral or leptomeningeal pathways, representing the secondary collateral circulation [11].

The secondary collaterals mainly include the ophthalmic artery and leptomeningeal collaterals, which play a vital role in acute stroke scenarios. For leptomeningeal collaterals, collateral flow occurs through surface connections that bridge pial arteries [10]. These connections bridge major arterials between ACA and PCA, ACA and MCA (Figure 1.2(a)), MCA and PCA (Figure 1.2(b)). TThe most marvel characteristic of leptomeningeal collateral is that the blood fluid can flow in both directions, enabling retrograde perfusion of adjacent territories and preventing cellular death due to ischemia [5]. Final infarct size [12, 13] and functional outcome deficit [14, 15] vary with the presence or absence of the collateral circulation of stroke patients based on angiographic data.

The collateral circulation confused scientists for centuries. The underlying causes of collateral blood flow and the occurrence of reverse blood flow are still not fully understood. Normal blood flow is piped from proximal large arteries to the distal small arteries by the high-pressure blood flow from the ventricle and the resistance to flow peripheral. In collateral circulation, the blood flow is allowed to flow from distal small arteries to large cerebral arteries when occlusive occurs. Understanding the mechanisms behind this reversed blood flow and the factors that drive collateral blood flow remains an area of ongoing research.

To gain insights into the complex nature of collateral circulation and the compensatory function of the posterior communicating artery (PComm), a simplified hemodynamic model has been proposed in this work. The proposed model aims to investigate the collateral circulation and the role played by the PComm in compensating for occlusions or disruptions in the normal blood flow pathways. By studying the simplified model, it is expected to unravel the underlying principles governing collateral circulation and its physiological significance.

1.2.3 Systemic Circulation

Systemic circulation is of great importance psychologically, which contains two parts: the arterial part and the venous part. The arterial part transports oxygenated blood to all tissues,

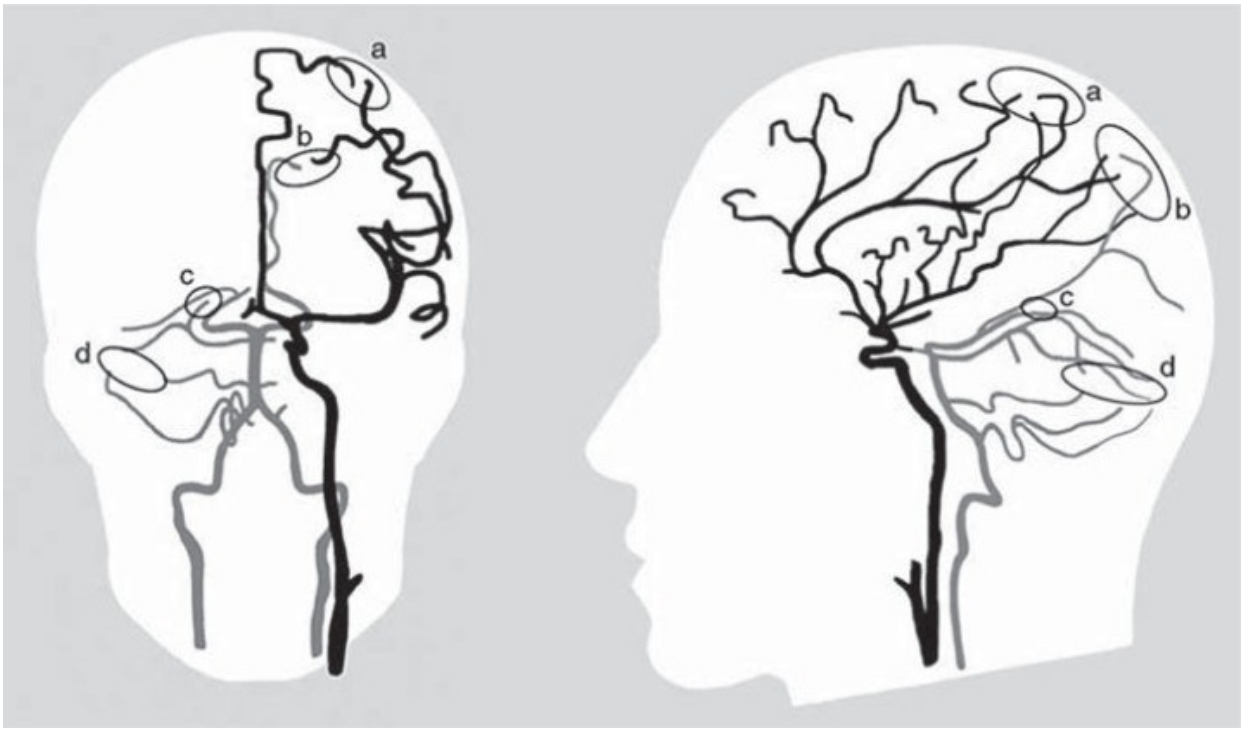

Figure 1.2 Diagram of leptomeningeal collaterals, bridging the anterior and middle cerebral arteries (a), the posterior and middle cerebral arteries (b), the superior and posterior cerebral arteries (c), and the major cerebellar hemispheric arteries (d)[5]

while the venous part transports the deoxygenated blood back to the heart for reoxygenation [16].

The heart ejects blood into the aorta and then distributes the blood flow throughout the body via systemic circulation. The larger arteries that arise from the aorta then branch into much smaller arterial vessels. Then the smaller arteries branch into arterioles, and the arterioles branch into much smaller vessels and become capillaries. In the end, the capillaries then join together to form veins and veins continue to join together to form the vena cava and bring the blood back into the heart as shown in Figure 1.3.

The systemic arteries include the large arteries, small arteries and arterioles, which form a vast network together. The lumen diameter (cross-section) changes from 400 to 4 cm^2 from

the aorta to the arterioles. Due to the limitation of imaging processing technique, obtaining precise geometric parameters of these vessels can be challenging. For computational simplification, the arteries and large arterioles are often represented as a 1-D binary tree structure or a 0-D three-element Windkessel boundary, which will be discussed in Chapter 2.1. The smaller arterioles are not considered in these models as they have multiple branches and loops [17].

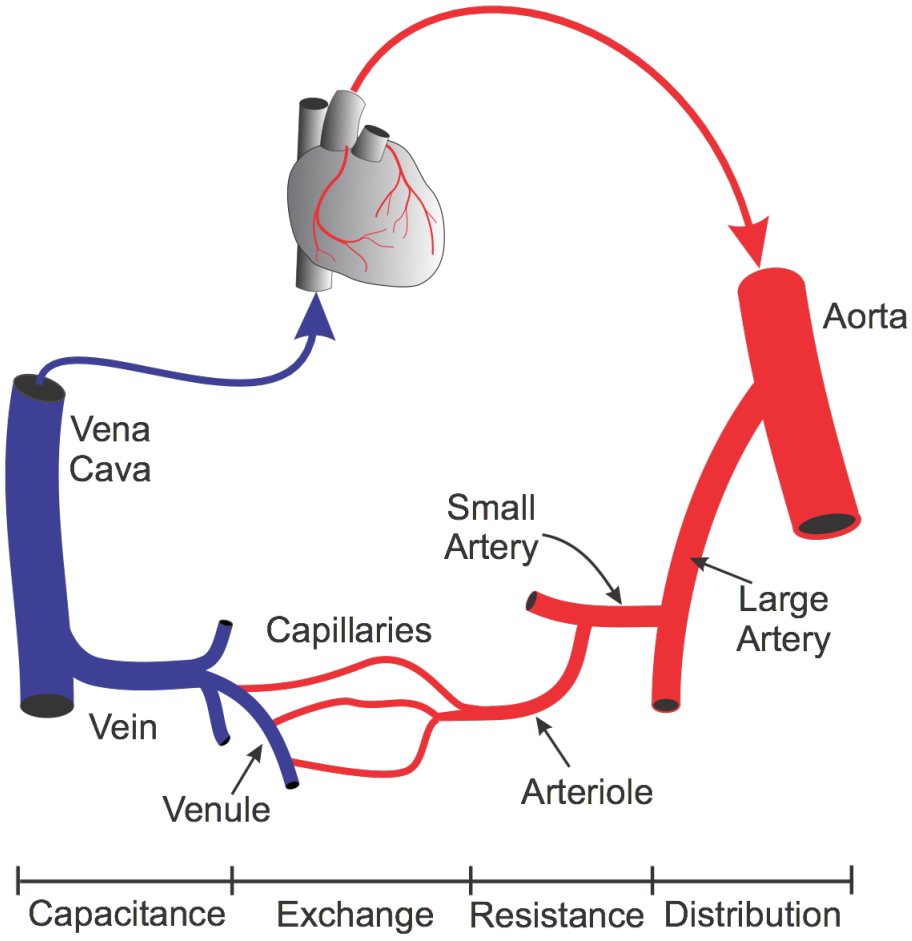

Figure 1.3 The structure of an artery wall [18]

1.2.4 Wave Propagation and Reflection in Arteries System

The blood is pumped into the aorta, the pressure rises, and the aorta wall is stretched. When the cardiac ejection slows down, the pressure falls back and the aorta wall relaxes. The inertial of the blood flow keeps it moving forwards after the driving difference has fallen. This causes the initial segment of the artery wall to overshoot its equilibrium position, leading to oscillations as the wall gradually approaches equilibrium. Simultaneously, the following segment of the wall becomes distended. As it recoils, the fluid-driven outflow causes further distension in the subsequent section of the wall, which also recoils, and so on [19]. The process of recoil and distension creates the disturbance that propagates along the arterial system. The balance between the restoring force provided by the elasticity of the artery walls and the inertia of the blood sustains the pressure wave.

The pressure wave in the artery can propagate in both upstream and downstream directions, composing positive and negative waves. For systemic arteries, only the wave that originates at the heart and is reflected from the periphery is considered. Other waves, that may lack physiological evidence and have no influence on blood pressure and velocity, are not considered in this study.

Every point of change along the arteries system will cause partial pressure reflection. There are many slight bends and unevenness along the arteries. However, the most significant wave reflection is from the junctions of the vessels. In this work, we will discuss the bifurcation effect and construct the bifurcation model. Additionally, constructing the boundary conditions is constructing artificial wave reflection from downstream systemic arteries.

Chapter Two

Cerebral Hemodynamics Modeling

2.1 Cerebral Blood Flow Modeling

Like all fluid systems, blood flow obeys mass, momentum, and energy conservation laws. Researchers employ 1-D to 3-D computational fluid dynamic (CFD) models to simulate the cerebral system, depending on the specific problem they are working on, and high accuracy is desired. For 1-D to 3-D blood flow models, Navier-Stokes equations (partial differential equations), without neglecting nonlinear terms, are used to acquire blood pressure and velocity [20]. The 1-D blood flow model is relatively simple and can be connected to the complex downstream vascular network. The computational efficiency and convenience of investigating the effect of the vascular network on upstream large arteries make 1-D blood flow models the most commonly utilized choice. In 2-D blood flow models, the 2-D axisymmetric fluid/shell element is employed to represent blood flow and vessel walls. The 2-D blood flow models can significantly reduce computation complexity compared to 3-D models while still capturing blood flow patterns [20]. The 3-D blood flow model is used to analyze complex flows in certain regions, such as flow separation at the vessel junctions and turbulence flow caused by placing stent and cerebral aneurysm [20].

The aim of this study is to explore the blood flow patterns in the brain under various conditions using 0-D and 1-D computational fluid dynamics (CFD) models. As the 3-D model results provide similar results that the 1-D model offers [21], it suggests that the 1-D model

is adequate when one is interested in blood pressure/flow at specific points along the vessels.

2.1.1 Blood Flow Properties

Blood is composed of plasma with red (erythrocytes), white (leucocytes) blood cells, and platelets (thrombocytes) in suspension [17]. Blood can be treated as a liquid with a suspension of flexible particles. The Newtonian viscous fluid is a type of fluid for which the shear stress is linearly proportional to the strain rate [22]. It can be applied to most homogeneous liquids, including blood flow. For large arteries, it is reasonable to regard the blood flow as a Newtonian fluid since the vessel diameters are significantly larger than the individual cell diameters [17].

2.1.2 Cerebral Blood Flow Modeling

The axial component of the 2-D Navier-Stokes equation, expressed in cylindrical coordinates, is utilized to describe the blood flow within the cerebral vascular network. This blood flow can be assumed as incompressible, inviscid Newtonian flow [23]. The z-momentum equation and the continuity equation can be simplified as Eqs. (2.1) and (2.2), respectively, based on the following assumptions: (i) the vessel is treated as an axisymmetric cylindrical tube and there is no dependence on θ ; (ii) the no-slip boundary condition is held is on the vessel wall ;(iii)in the transverse direction, the fluid moves with the vessel wall, resulting in $u_r|_{r=R} = \frac{\partial R}{\partial t}$[24, 25].

$$\frac{\partial u_z}{\partial t} + u_r \frac{\partial u_z}{\partial r} + u_z \frac{\partial u_z}{\partial z} = -\frac{1}{\rho}\frac{\partial p}{\partial z} + \frac{\mu}{\rho}\left[\frac{1}{r}\frac{\partial}{\partial r}\left(r\frac{\partial u_z}{\partial r}\right) + \frac{\partial^2 u_z}{\partial z^2}\right] \tag{2.1}$$

$$\frac{1}{r}\frac{\partial}{\partial r}\left(r u_r\right) + \frac{\partial u_z}{\partial z} = 0 \tag{2.2}$$

The blood flow rate $q(z,t)$ and the cross-sectional area $A(z,t)$ are defined as follows,

$$A\left(z,t\right) = \pi R\left(z,t\right)^2 \tag{2.3}$$

$$q(z,t) = 2\pi \int_0^{R(z,t)} u_z(z,r,t) r \, dr \tag{2.4}$$

where $R(z,t)$ is the radius of the vessel. The higher-order term $\frac{\partial^2 u_z}{\partial z^2}$ can be neglected aas dimensional analysis reveals its insignificance compared to other terms. We integrate the governing equations over the cross-sectional area $A(z,t)$ of the vessel. The governing equations can be expressed in terms of $A(z,t)$ and $q(z,t)$ as follows,

$$\frac{\partial A}{\partial t} + \frac{\partial q}{\partial z} = 0 \tag{2.5}$$

$$\frac{\partial q}{\partial t} + 2\pi \int_0^R \frac{\partial (u_z)^2}{\partial z} r \, dr = -\frac{A}{\rho}\frac{\partial p}{\partial z} + 2\pi \frac{\mu}{\rho} R \left[\frac{\partial u_z}{\partial r}\right]_R \tag{2.6}$$

To further simplify the viscous and nonlinear term of the Navier-Stokes equation, we assume that there is a boundary layer with a thickness δ near the wall. The velocity u_z along the long axis of the vessel can be approximated as a flat velocity [23].

$$u_z = \begin{cases} u, & r \leq R - \delta \\ \frac{u(R-r)}{\delta}, & R - \delta < r \leq R \end{cases} \tag{2.7}$$

The second term of Eq. (2.6) can be eliminated by integrating Eq. (2.7) across the cross-sectional area. Now, the governing equations are expressed in the following form.

$$\frac{\partial A}{\partial t} + \frac{\partial q}{\partial z} = 0 \tag{2.8}$$

$$\frac{\partial q}{\partial t} + \frac{\partial}{\partial z}\left(\frac{q^2}{A}\right) = -\frac{A}{\rho}\frac{\partial p}{\partial z} - \frac{2\pi \nu q R}{\delta A} \tag{2.9}$$

The vessel wall can be treated as an elastic thin shell and the deformation is axisymmetric [26]. The constitutive relationship used to model the elasticity of the vessel wall is given as follows [24].

$$p - p_0 = \frac{4}{3}\frac{Eh}{r_0}\left(1 - \sqrt{\frac{A_0}{A}}\right) \tag{2.10}$$

where p_0 and A_0 are the blood pressure and cross-sectional area of the undeformed vessel wall, respectively; h denotes the average thickness of the vessel wall [27]; A corresponds to the cross-sectional area of the deformed vessel wall under pressure. The nonlinear relationship

between the pressure and cross-section area is used to capture the biological characteristic of the vessel wall. Eq. (2.10) reveals that the blood pressure is dependent on the cross-sectional area A and the undeformed radius r_0 [28]. $\frac{\partial p}{\partial z}$ can be expanded into two terms $\frac{\partial p}{\partial A}\frac{\partial A}{\partial z}$ and $\frac{A}{\rho}\frac{\partial p}{\partial r_0}\frac{\partial r_0}{\partial z}$, respectively. Further discussion on the governing equation will be presented in Chapter 2.3.

2.2 Cerebral Artery Wall Modeling

2.2.1 Cerebral Artery Wall Overview

The blood vessels can be divided into five groups: arteries, arterioles, capillaries, venules, and veins [23]. Arteries carry oxygenated blood from the heart gradually branching and narrowing into arterioles. The arterioles supply capillaries, and the capillaries empty into the venules. The venules in turn drain into the veins that lead back to the heart. In this dissertation, only the arteries and arterioles are considered.

Different types of blood vessels have slightly different structures, but they have some general features. Typically, the artery wall has three layers (See Figure 2.1). The outer layer of an artery is known as tunica externa, which is made of collagen fibers and elastic tissue. The inside layer is the tunica media, which is made up of smooth muscle cells, elastic tissue and collagen fibers [29]. The inner layer is known as tunica intima. The hollow cavity where the blood flow goes through is known as the lumen.

All arteries have relatively thick walls to hold high blood pressure. Particularly, the arteries close to the heart have the thickest wall and contain more elastic fibers in all three of their tunics, which are called “elastic arteries”. This property of elastic arteries allows them to expand when the blood pumped from the ventricles passes through them, and to recoil and drive the blood to smaller arteries [30]. The store and release ability of arteries is known as ‘compliance’. Further from the heart, the concentration of the elastic fiber decreases and

muscle fiber increases in the tunica media in relatively smaller arteries, which is known as the "muscle artery" [30]. The arterioles are very small arteries that lead to the capillaries and it is very important in slowing down or resisting the blood flow, thus the blood pressure and velocity are changed, which is known as "resistance" [30].

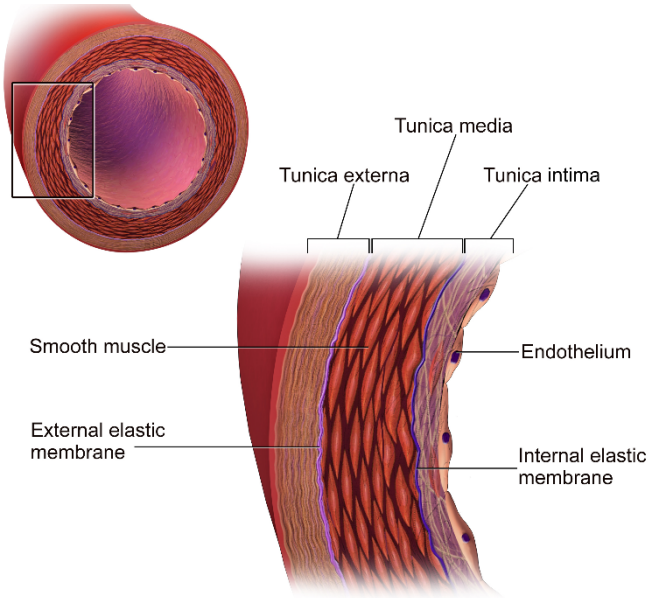

Figure 2.1 The structure of an artery wall [18]

2.2.2 Cerebral Vessel's Young's Modulus

The behavior of an artery wall should be characterized as viscoelastic, anisotropic, and inhomogeneous material. For computational simplification, only inhomogeneous property is included in the study. The Young's modulus E of the cerebral artery wall is varying with undeformed vessel radius r_0, as shown in Figure 2.2 [31].

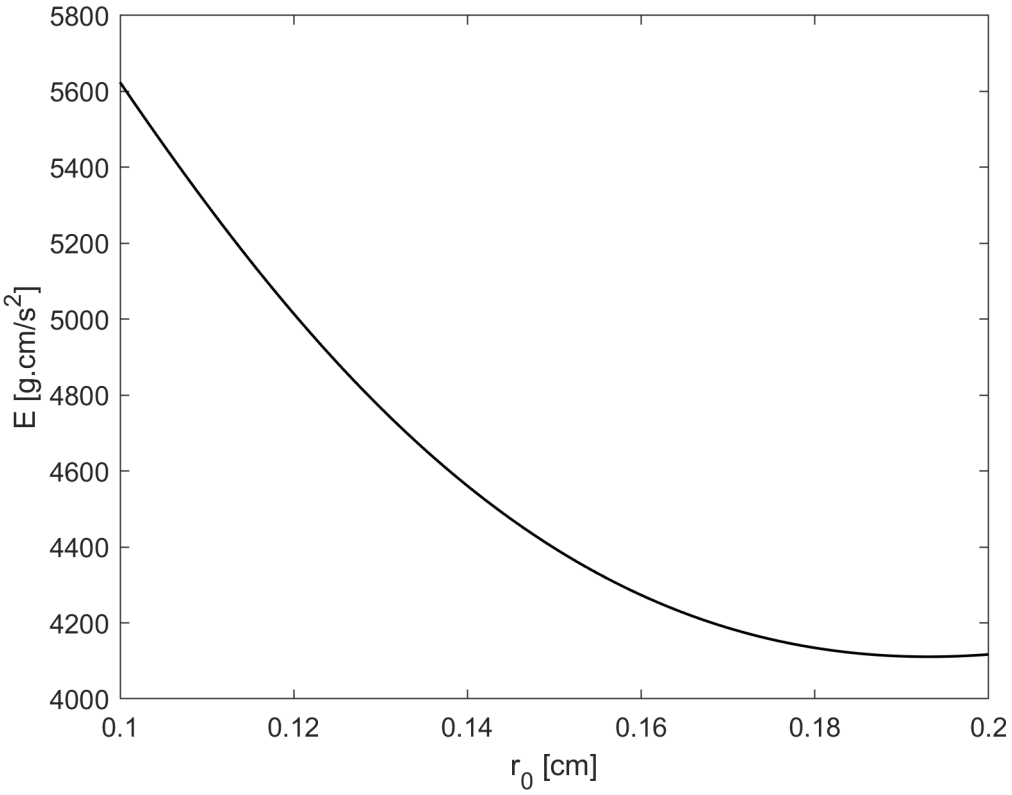

Figure 2.2 Young's modulus of cerebral vessel wall

2.2.3 Cerebral Artery Geometry Model

The vessel cross-sectional area is not consistent from upstream to downstream. Typically, the change of radius follows an exponential curve based on dog vessel experiments and human arterial systemic measurements [23, 32, 33]. In this study, the mean radius of the large cerebral artery is tapered along the long axis, which follows the exponential curve as shown in Eq. (1) [34].

$$r(z) = r_{top} \exp(-kz) \tag{2.11a}$$

$$k = \frac{\log\left(\frac{r_{bottom}}{r_{top}}\right)}{L} \tag{2.11b}$$

where k is the tapering factor that matches the measured geological data from each vessel.

2.3 Nondimensionalization

For facilitate computational convenience, the governing equations are nondimensionalized with the characteristic radius $r_c = 1$ cm, the characteristic blood flow $q_c = 10$ cm^3/s and the characteristic blood flow density $\rho_c = 1.06$ g/cm^3. Other nondimensional parameters of blood flow are provided in Table 2.1.

Table 2.1 Characteristics parameters

Displacement	$\widetilde{z} = \frac{z}{r_c}$
Radius	$\widetilde{r} = \frac{r}{r_c}$
Flow	$\widetilde{q} = \frac{q}{r_c}$
Kinematic viscosity	$\widetilde{\nu} = \frac{\nu r_c}{q_c}$
Time	$\widetilde{t} = \frac{t q_c}{r_c^3}$
Cross-sectional area	$\widetilde{A} = \frac{A}{r_c^2}$
Pressure	$\widetilde{p} = \frac{p r_c^4}{\rho q_c^2}$
Boundary layer	$\widetilde{\delta} = \frac{\delta}{r_c}$

The characteristic parameters listed in Table 2.1 are applied to nondimensionalize the governing governing equations (Eq. 2.8) and (2.9).

$$\frac{\partial(\tilde{A}r_c^2)}{\partial\left(\frac{\tilde{t}r_c^3}{q_c}\right)} + \frac{\partial\left(\tilde{q}q_c\right)}{\partial\left(\tilde{z}r_c\right)} = 0 \tag{2.12}$$

$$\frac{\partial(\tilde{q}q_c)}{\partial\left(\frac{\tilde{t}r_c^3}{q_c}\right)} + \frac{\partial}{\partial(\tilde{z}r_c^2)}\left(\frac{\tilde{q}^2q_c^2}{\tilde{A}r_c^2}\right) = -\frac{\tilde{A}r_c^2}{\rho}\frac{\partial\left(\frac{p\rho q_c^2}{r_c^2}\right)}{\partial\left(\tilde{z}r_c\right)} - \frac{2\pi\nu\tilde{q}q_c\tilde{r}r_c}{\tilde{\delta}r_c\tilde{A}r_c^2} \tag{2.13}$$

The above equations can be further simplified by introducing Reynold's number $Re = \frac{\rho q_c}{\mu r_c}$.

$$\frac{\partial A}{\partial t} + \frac{\partial q}{\partial z} = 0 \tag{2.14}$$

$$\frac{\partial q}{\partial t} + \frac{\partial}{\partial z}\left(\frac{q^2}{A}\right) = -\frac{A}{\rho}\frac{\partial p}{\partial z} - \frac{2\pi qr}{\delta ARe} \tag{2.15}$$

As discussed in Chapter 2.1, the blood pressure idepends on the deformed cross-sectional area A and the undeformed radius r_0. The term $\frac{\partial p}{\partial z}$ can be expanded into two terms $\frac{\partial p}{\partial A}\frac{\partial A}{\partial z}$ and $\frac{A}{\rho}\frac{\partial p}{\partial r_0}\frac{\partial r_0}{\partial z}$ respectively, as illustrated in Eq. (2.16).

$$\frac{\partial q}{\partial t} + \left(\frac{2q}{A}\right)\frac{\partial q}{\partial z} + \left(-\frac{q^2}{A^2} + \frac{A}{\rho}\frac{\partial p}{\partial A}\right)\frac{\partial A}{\partial z} = -\frac{A}{\rho}\frac{\partial p}{\partial r_0}\frac{\partial r_0}{\partial z} - \frac{2\pi qr}{\delta ARe} \tag{2.16}$$

For computational convenience, the governing equations are written in matrix form as,

$$\frac{\partial}{\partial t}\begin{pmatrix} A \\ q \end{pmatrix} + \frac{\partial}{\partial x}\begin{pmatrix} q \\ \frac{q^2}{A} + f\sqrt{A_0 A} \end{pmatrix} = \begin{pmatrix} 0 \\ -\frac{2\pi qr}{\delta ARe} + \left(2\sqrt{A}\left(\sqrt{\pi}f + \sqrt{A_0}\frac{df}{dr_0}\right) - A\frac{df}{dr_0}\right)\frac{dr_0}{dz} \end{pmatrix} \tag{2.17}$$

where f is $\frac{4}{3}\frac{Eh}{r_0}$.

2.4 Numerical Method

The second-order accuracy finite difference method in spatial and time, two-step Lax-Wendroff scheme, is used to solve the governing equations for all interior points [35]. For computational convenience, the governing equation (Eq. (2.17)) can be rewritten as follows,

$$\frac{\partial \mathbf{U}}{\partial t} + \frac{\partial \mathbf{F}}{\partial z} = \mathbf{S} \tag{2.18}$$

where the dependent variable $\boldsymbol{U} = \begin{pmatrix} A \\ q \end{pmatrix}$, net flux vector $\boldsymbol{F} = \begin{pmatrix} q \\ \frac{q^2}{A} + f\sqrt{A_0 A} \end{pmatrix}$ and the outflow vector $\boldsymbol{S} = \begin{pmatrix} 0 \\ \frac{-2\pi qr}{\delta ARe} + (2\sqrt{A}(\sqrt{\pi}f + \sqrt{A_0}\frac{df}{dr_0}) - A\frac{df}{dr_0})\frac{dr_0}{d_z} \end{pmatrix}$.

The dependent variable $\boldsymbol{U}$, net flux vector $\boldsymbol{F}$, and outflow vector $\boldsymbol{S}$ can be discretized as $\boldsymbol{U}_m^n = \boldsymbol{U}(m\Delta z, n\Delta t)$, $\boldsymbol{F}_m^n = \boldsymbol{F}(m\Delta z, n\Delta t)$, and $\boldsymbol{S}_m^n = \boldsymbol{S}(m\Delta z, n\Delta t)$ in time and space.

The first step of the Lax-Wendroff scheme computes the value of $\boldsymbol{U}_m^n$ at half grid $m \pm 1/2$ and half-time step $n \pm 1/2$.

$$\mathbf{U}_{m+\frac{1}{2}}^{n+\frac{1}{2}} = \frac{1}{2}\left(\mathbf{U}_{m+1}^n + \mathbf{U}_m^n\right) + \frac{\Delta t}{2\Delta z}\left(-\mathbf{F}_{m+1}^n + \mathbf{F}_m^n\right) + \frac{\Delta t}{4}\left(\mathbf{S}_{m+1}^n + \mathbf{S}_m^n\right) \tag{2.19}$$

$$\mathbf{U}_{m-\frac{1}{2}}^{n+\frac{1}{2}} = \frac{1}{2}\left(\mathbf{U}_m^n + \mathbf{U}_{m-1}^n\right) + \frac{\Delta t}{2\Delta z}\left(-\mathbf{F}_m^n + \mathbf{F}_{m-1}^n\right) + \frac{\Delta t}{4}\left(\mathbf{S}_m^n + \mathbf{S}_{m-1}^n\right) \tag{2.20}$$

The intermediate value $\boldsymbol{U}_{m\pm1/2}^{n+1/2}$ acquired from the first step is used to compute the value of $\boldsymbol{U}_m^{n+1}$ at the next time step.

$$\mathbf{U}_m^{n+1} = \mathbf{U}_m^n - \frac{\Delta t}{\Delta z}\left(\mathbf{F}_{m+\frac{1}{2}}^{n+\frac{1}{2}} - \mathbf{F}_{m-\frac{1}{2}}^{n+\frac{1}{2}}\right) + \frac{\Delta t}{4}\left(\mathbf{S}_{m+\frac{1}{2}}^{n+\frac{1}{2}} + \mathbf{S}_{m-\frac{1}{2}}^{n+\frac{1}{2}}\right) \tag{2.21}$$

The CFL condition ensures the stability of the scheme,

$$\frac{\Delta t}{\Delta z} \leq \left|\frac{q}{A} \pm \sqrt{\frac{A}{\rho}\frac{\partial p}{\partial A}}\right|^{-1} \tag{2.22}$$

where $\frac{q}{A}$ is the mean velocity of the blood flow across the cross-sectional area. The wave speed can be solved along the characteristic line and represented as $\sqrt{\frac{A}{\rho}\frac{\partial p}{\partial A}}$.

Chapter Three

Outlet Boundary Conditions

3.1 The Review of Outlet Boundary Conditions

The boundary conditions play a crucial role in our model, as they can provide artificial wave reflections originating from downstream vessel junctions. By including realistic boundary conditions, the pressure wave resulting from simulations can closely resemble the physiological pressure wave.

Depending on the specific problem being addressed and the desired level of accuracy, researchers choose either the 0-D or 1-D outlet boundary model to simulate blood flow. The 0-D outlet boundary model utilizes a set of ordinary differential equations (ODEs) to represent the vasculature. Each compartment within the 0-D model is associated with two ODEs, which capture mass and momentum conservation. This simplified representation of the systemic arteries in the 0-D model allows for the inclusion of major components, such as the heart and heart valves [20]. This feature makes the 0-D systemic arteries model useful when constructing the global distribution of pressure and blood flow along the systemic arteries.

In contrast, the 1-D outlet boundary model employs Navier-Stokes equations to describe blood pressure and flow [20]. The 1-D outlet boundary model allows people to acquire wave reflection from downstream vessel junctions, which has been discussed in Chapter 1.

In this chapter, we will discuss both 0-D and 1-D outlet boundary conditions. Addition-

ally, we will provide an illustrative example featuring the connection of 0-D and 1-D outlet boundary conditions to the upstream large artery.

3.1.1 0-D Outlet Boundary Model

The foundation of the 0-D model lies in the observation that blood flow exhibits similarities to electrical conduction within a circuit [3]. Consequently, conventional methods used in electrical circuit analysis can be employed to investigate cardiovascular dynamics. In this analogy, resistance (R), inductance (L), and capacitance (C) within the circuit correspond to the effects of friction, inertia, and vessel elasticity on blood flow, respectively. Poiseuille's law governs the steady blood flow, while the linearized Navier-Stokes equations govern the unsteady blood flow [20]. Over the course of a century, numerous 0-D models have been developed.

The simplest and the first mono-compartment description is the famous two-element Windkessel model (RC), which was first proposed by Stephen Hales in 1733, and later formulated mathematically by Otto Frank in 1899 [36]. The RC model consists of two elements: one is the capacitor C which represents the storage properties of large arteries and the other is a resistor R which describes the dissipative properties of arterioles and capillaries. The RC model effectively captures the fundamental characteristics of the systemic artery network, making it widely utilized in clinical practice as a simple terminal boundary condition in more complex distributed parameter representations [24]. Numerous networks have been developed based on the two-element (RC) and three-element (RCR) Windkessel models [37, 38, 39, 40, 41], incorporating additional components such as the ventricle and heart to accommodate specific requirements. Nowadays, as the efficiency of the computer is surging, the RC/RCR model is used to construct the whole circulatory system and works as a terminal for important local branch models [42, 43, 44, 45, 46, 47, 48, 49].

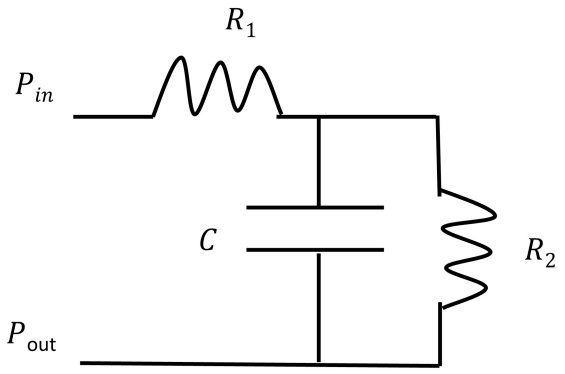

Figure 3.1 Three-element Windkessel model (RCR Model)

3.1.2 1-D Outlet Boundary Model

Pressure/velocity wave propagation of systemic arteries is one of the most important problems in the study of cardiovascular/cerebrovascular physiology [20]. It is believed that the blood pressure/velocity waveform encloses valuable information, such as cardiac function, the elasticity of vessel walls and pathological conditions of the heart/brain [32]. Thus, wave propagation studies have received extensive attention in cardiovascular research in recent years [22]. Compared with the higher-dimensional models (2-D/3-D models), the 1-D model not only captures the wave propagation characteristics of blood flow but also demands fewer computational resources [20]. Thus, the 1-D model has greater advantages when describing the pressure and flow variations throughout the entire systemic arteries.

In the late 20th century, researchers employed simple combinations of sine/cosine functions to define pressure/flow waveforms for outlet boundary conditions, aiming to mimic the physiological conditions of downstream vessels [36, 50, 51]. More recently, efforts have been made to develop more realistic outlet boundary conditions, including variable resistance [52], or connecting RCR models to the 1-D boundary model as terminal descriptions to better represent reflected waves. Some researchers focused on non-reflecting boundary conditions and

compatibility conditions [53], while others explored non-reflection boundary conditions with reflecting coefficients [54, 55]. Olufsen [24] proposed a binary tree outlet boundary condition accurately describing the vessel branching of the downstream vessels .

3.2 The 0-D Three–Element Windkessel Outlet Boundary Conditions

The three-element Windkessel (RCR) outlet boundary condition is one of the 0-D boundary models we have introduced in Chapter 3.1. The computational efficiency and ease of use make it particularly valuable when connecting the outlet boundary condition to the upstream large cerebral artery. In this chapter, we will discuss the three-element Windkessel outlet boundary condition and provide a detailed procedure on how to connect the outlet boundary condition to the upstream large artery.

The three-element Windkessel outlet boundary condition is based on wave transmission theory [56]. The model comprises two resistances R_1, R_2 along with compliance C_T (Figure 3.1). The two resistances R_1, R_2 represent the blood flow resistance encountered as blood flows through the systemic arterial system. The compliance C_T simulates the storage and release of blood flow by major arteries during the cardiac cycle [17]. The impedance can be represented in the frequency domain [20],

$$\bar{Z}\left(0,\omega\right) = \frac{R_1 + R_2 + i\omega C_T R_1 R_2}{1 + i\omega C_T R_2} \tag{3.1}$$

The governing equation of the upstream large artery is solved in the time domain. In order to connect with the upstream large artery, the governing equations of three-element Windkessel boundary conditions are transformed from the frequency domain to the time domain. To connect the exterior points with the three-element Windkessel outlet boundary conditions, the impedance is convolved with the pressure and flow at the end of the vessel into the time domain [56].

$$\frac{\partial p}{\partial t} = R_1 \frac{\partial q}{\partial t} - \frac{p}{R_2 C_T} + \frac{q\,(R_1 + R_2)}{R_2 C_T} \tag{3.2}$$

The pressure and blood flow p_m^n and q_m^n can be further discretized as follows,

$$\frac{p_m^{n+1} - p_m^n}{\Delta t} = R_1 \frac{(q_m^{n+1} - q_m^n)}{\Delta t} - \frac{p_m^n}{R_2 C_T} + \frac{q_m^n\,(R_1 + R_2)}{R_2 C_T} \tag{3.3}$$

$$A_m^{n+1} = A_m^n - \frac{\Delta t}{\Delta x}\left(q_m^{n+1} - q_m^n\right) \tag{3.4}$$

The cross-sectional area and the blood flow $A_m^{n+1}$and q_m^{n+1},at the boundary can be achieved by using an iterative method. The iteration starts from an initial guess for pressure at the boundary (p_{guess}), and the converged result is obtained by using the first-order finite difference method. The convergence criterion is given by

$$\left|p_{guess} - p_m^{n+1}\right| \leq 1e-7 \tag{3.5}$$

3.3 The 1-D Binary Tree Outlet Boundary Conditions

As discussed in Chapter 1, wave reflection originating from downstream vessel junctions adds an enhancement to the pressure waveform in the upstream large artery. To accurately capture the wave reflection and transmission from downstream arterioles, a realistic binary tree outlet boundary condition is constructed based on the 1-D outlet boundary model by Olufsen [24].

The outlet boundary condition is developed on the basis of the long-wave propagation assumption and incorporates the viscoelastic and distensibility of the vessel walls. The simplified momentum and continuity equations govern the downstream small vessels, while the impedance is solved in the frequency domain. The binary tree outlet boundary condition, depicted in Figure 3.2, is connected to the upstream large artery to acquire the pressure or blood flow waveform.

Several assumptions are made in modeling the downstream systemic arterial network [33].

It is assumed that the binary-tree structure exhibits symmetric on both the left and right sides, and the changes in the radius of the parent vessel and daughter vessels follow a linear relationship [57].

$$r_{d_1} = \alpha_1 \, r_p \tag{3.6a}$$

$$r_{d_2} = \beta_1 \, r_p \tag{3.6b}$$

where r_p is the radius of the parent vessel and r_d is the radius of the daughter vessels; α_1 and β_1 are scaling factors. The scaling factor is determined based on the principle of minimum work for a range of flow, from turbulence to laminar and area-ratio relationship between daughter and parent vessels [58, 59, 59]. The mean value from experimental data of cerebral vascular provides us with the scaling factors α_1 and β_1, which are 0.91 and 0.58, respectively.

The goal is to develop a tree-like structure that represents the downstream systemic arterial network and can be applied at the terminal of large arteries. However, it is not practical to include all the small arteries and the arterioles into the model. The decision to terminate the structure is determined by the minimum radii at the end of the outlet boundary conditions.

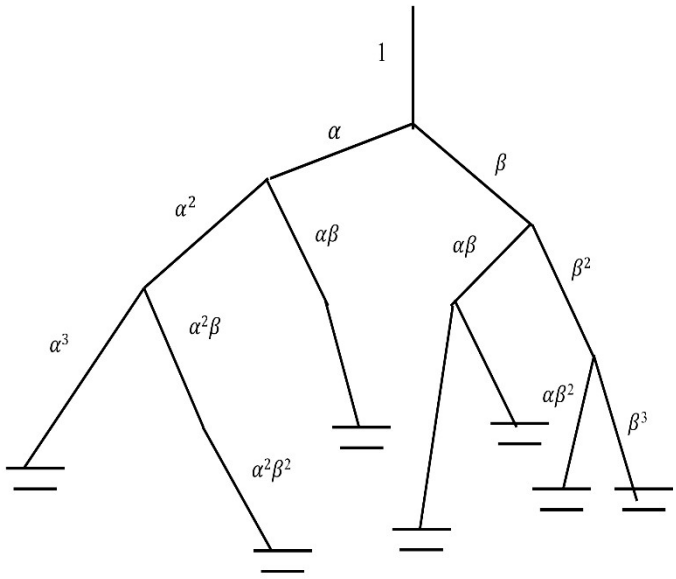

Figure 3.2 Binary tree outlet boundary conditions illustration

3.3.1 Governing Equations and Solution Process

The 2-D Navier-Stokes equation in cylindrical coordinates governs the blood flow. We assume that the fluid is incompressible and Newtonian. The linear constitutive relationship is used to model the elasticity of the vessel wall. In order to account for the viscoelastic behavior of the vessel wall, the tethering force is included as part of the external forces. At the vessel wall, a balance is maintained between fluid motion and solid motion, with the fluid velocity assumed to be at rest. The governing equations are listed below [60, 61].

Fluid Motion:

$$\frac{\partial u_r}{\partial t} + u_r\frac{\partial u_r}{\partial r} + u_z\frac{\partial u_r}{\partial z} = -\frac{1}{\rho}\frac{\partial p}{\partial r} + \frac{\mu}{\rho}\left[\frac{\partial^2 u_r}{\partial\, r^2} + \frac{1}{r}\frac{\partial u_r}{\partial r} + \frac{\partial^2 u_r}{\partial z^2} - \frac{u_r}{r^2}\right] \tag{3.7a}$$

$$\frac{\partial u_z}{\partial t} + u_r\frac{\partial u_z}{\partial r} + u_z\frac{\partial u_z}{\partial z} = -\frac{1}{\rho}\frac{\partial p}{\partial z} + \frac{\mu}{\rho}\left[\frac{1}{r}\frac{\partial}{\partial r}\left(r\frac{\partial u_z}{\partial r}\right) + \frac{\partial^2 u_z}{\partial z^2}\right] \tag{3.7b}$$

$$\frac{1}{r}\frac{\partial}{\partial r}(ru) + \frac{\partial u_z}{\partial z} = 0 \tag{3.7c}$$

Vessel Wall Motion:

$$M_0\frac{\partial^2 \xi}{\partial t^2} + C_l\frac{\partial \xi}{\partial t} + k_l\xi = -\mu\left[\frac{\partial u_z}{\partial r} + \frac{\partial u_r}{\partial z}\right]_{r=r_0} + \frac{\partial \eta}{\partial z}\frac{T_{t0} - T_{\theta 0}}{r_0} + \frac{\partial T_t}{\partial z} \tag{3.8a}$$

$$M_0\frac{\partial^2 \eta}{\partial t^2} + C_l\frac{\partial \eta}{\partial t} + k_l\eta = -\mu\left[p - 2\mu\frac{\partial u_r}{\partial r}\right]_{r=r_0} + \frac{\eta}{r_0^2}T_{\theta 0} - \frac{T_\theta - T_{\theta -}}{T_0} + T_{t0}\frac{\partial^2 \eta}{\partial z^2} \tag{3.8b}$$

where M, C, and K represent the spring coefficient, frictional coefficient of dashpot and additional mass of tethering force of the viscoelastic behavior of the vessel wall, respectively.

Interaction Conditions:

$$u_r\left(r, z, t\right)_{r=r_0} = \frac{\partial \eta}{\partial t} \tag{3.9a}$$

$$u_z\left(r, z, t\right)_{r=r_0} = \frac{\partial \xi}{\partial t} \tag{3.9b}$$

The classical solution was proposed by Womersley [62], and later extended by Atabek [60, 61]. The solutions of velocity u_z, pressure p can be assumed to be harmonic functions, considering that the blood flow exhibits periodic behavior over time with a period T,

$$u_z\left(r, z, t\right) = u_z\left(r\right)e^{i\omega\left(t - \frac{z}{c}\right)} \tag{3.10}$$

$$p\left(r, z, t\right) = p_r\left(r\right)e^{i\omega\left(t - \frac{z}{c}\right)} \tag{3.11}$$

where $\omega = \frac{2\pi k}{T}$ is the angular frequency and c is the wave speed.

The set of governing equations is linearized, yielding an inhomogeneous Bessel function. By solving this inhomogeneous Bessel function, the velocity profile u_z can be acquired. Additionally, the long-wave approximation is applied to further simplify the velocity and pressure profile [24, 60, 61], shown as follows,

$$u_z = p_c \left(-\frac{r_0 \beta_0^2}{\mu w_0^2} + A \frac{J_0\left(\frac{w_0 r}{r_0}\right)}{J_0\left(w_0\right)} \right) \tag{3.12a}$$

$$p_r = p_c J_0 \left(\frac{\beta_0 r}{r_0} \right) \tag{3.12b}$$

where J_0 and J_1 denote the 0^{th} and 1^{st} order Bessel functions; A is determined by boundary conditions; r_0 is the inner radius of undeformed vessel; w_0 and β_0 are dimensionless parameters and are given by the following relations,

$$w_0 = \frac{i^3 r_0^2 \omega}{\nu} \tag{3.13a}$$

$$\beta_0 = \frac{i r_0 \omega}{\nu} \tag{3.13b}$$

The 1-D volumetric flow can be determined by integrating the longitudinal velocity, which will be utilized to simplify the continuity and momentum equations,

$$Q(z,t) = 2\pi \int_0^{r_0} u_z(z,r,t) r dr \tag{3.14}$$

As the inlet flow for upstream large artery is periodic blood flow, both the blood pressure and flow for upstream large artery can be expressed by complex periodic Fourier series,

$$p\left(z,t\right) = \sum_{k=-\infty}^{\infty} P\left(z,\omega\right) e^{-i\omega t} \tag{3.15}$$

$$q\left(z,t\right) = \sum_{k=-\infty}^{\infty} Q\left(z,\omega\right) e^{-i\omega t} \tag{3.16}$$

$$P\left(z,\omega\right) = \frac{1}{T} \int_{\frac{-T}{2}}^{\frac{T}{2}} p\left(z,t\right) e^{-i\omega t}\ dt \tag{3.17}$$

$$Q\left(z,\omega\right) = \frac{1}{T} \int_{\frac{-T}{2}}^{\frac{T}{2}} q\left(z,t\right) e^{-i\omega t}\ dt \tag{3.18}$$

The contunity and momentum equation can be re-written by using the longtitudinal velocity solved from governing equations (Eqs. 3.7-3.9)[24, 60, 61].

$$i\omega C P + \frac{\partial Q}{\partial z} = 0 \tag{3.19a}$$

$$i\omega Q + \frac{A_0}{\rho} \frac{\partial P}{\partial z} (1 - F_k) = 0 \tag{3.19b}$$

where compliance $C = \frac{dA}{dP}|_{P=P_0} = \frac{3A_0 r_0}{2Eh}$, which is obtained from constitutive relationship of vessel wall in Eq. (2.10); and $F_k = \frac{2J_1(w_0)}{w_0 J_0(w_0)}$.

The aforementioned equations can be reformulated into the following set of equations, expressed in terms of P and Q.

Assuming the solution of pressure P and blood flow Q has the following form,

$$Q(z,\omega) = a\cos\frac{\omega z}{c} + b\sin\frac{\omega z}{c} \tag{3.20}$$

$$P(z,\omega) = i\sqrt{\frac{\rho}{CA_0(1-F_k)}}\left(-a\cos\frac{\omega z}{c} + b\sin\frac{\omega z}{c}\right) \tag{3.21}$$

where a and b are arbitrary constants and determined by boundary conditions.

For any Fourier mode, the frequency-dependent impedance $\bar{Z}(x,\omega)$ can be related to pressure and blood flow by

$$P(z,\omega) = \bar{Z}(z,\omega)\, Q(z,\omega) \tag{3.22}$$

Through the inverse Fourier transform, the impedance in frequency domain $\bar{Z}(z,\omega)$ can be transformed into time-domain $\tilde{z}(z,t)$ which can be used to compute the transient response of the pressure

$$p(z,t) = \int_{t-T}^{t} q(z,\tau)\,\tilde{z}(z,t-\tau)\;\, d\tau \tag{3.23}$$

The periodic pressure waveform obtained through Eq. (3.23) will be applied at the terminal of large arteries. The root impedance $\bar{Z}(0,\omega)$ in frequency domain can be computed by and assuming the impedance $\bar{Z}(L,\omega)$ is known.

$$\bar{Z}(0,\omega) = \frac{\frac{i}{\sqrt{CAK/\rho}}\sin\frac{\omega L}{c} + \bar{Z}(L,\omega)\cos\frac{\omega L}{c}}{\cos\frac{\omega L}{c} + i\sqrt{\frac{CAK}{\rho}}\bar{Z}(L,\omega)\sin\frac{\omega L}{c}} \tag{3.24}$$

where the impedance $\bar{Z}(L,\omega)$ can be found by

$$\bar{Z}(0,0) = \bar{Z}(L,0) + \frac{8\mu l_{rr}}{\pi r^3} \tag{3.25}$$

at zero frequency, where μ is the viscosity, l_{rr} is the length-to-radius ratio.

The junction condition for impedance in the frequency domain is defined as,

$$\frac{1}{\bar{Z}_p} = \frac{1}{\bar{Z}_{d_1}} + \frac{1}{\bar{Z}_{d_2}} \tag{3.26}$$

where $\bar{Z}_p$, $\bar{Z}_{d_{1,2}}$ are the impedances of the parent vessel and the daughter vessel, respectively.

3.3.2 Connecting to Upstream Large Arteries

The impedance in frequency domain $\bar{Z}(z,\omega)$ is first transformed into the time domain by using the inverse Fourier Transformation. The transfer function $\tilde{z}(z,t)$ in the time domain is related to pressure $p(x,t)$ and flow $q(z,t)$, as follows,

$$q\left(x_M,t\right) = \int_0^T p\left(x_M,\tau\right)\tilde{z}\left(x_M,t-\tau\right)\ d\tau \tag{3.27}$$

We discussed the cerebral blood flow modeling for the upstream large arteries in Chapter 2. The axial component of 2-D Navier-Stokes equation in cylindrical coordinates governs the blood flow of an upstream large artery, and the interior points were solved by a two-step Lax-Wendroff finite difference numerical scheme. In order to connect with the upstream large artery, the convolution form of the structured tree outlet boundary conditions can be utilized to solve the exterior boundary points by discretizing Eq. (3.28), which can be written as

$$q_M^n = q\left(M\Delta z, n\Delta t\right) = \sum_{k=0}^{N-1} p_M^{n-k}\tilde{z}^k\Delta t \tag{3.28}$$

where q_M^n represents the discretized points at grid M and time step n for structured tree outlet boundary conditions.

For computing convenience, Eq. (3.29) can be further rewritten by separating the first term of impedance,

$$q\left(M\Delta z, n\Delta t\right) = p_M^n\tilde{z}^0\Delta t + \sum_{k=1}^{N-1} p_M^{n-k}\tilde{z}^k\Delta t \quad (n-k\geq 0) \tag{3.29}$$

The structured tree outlet boundary conditions introduce two exterior points, which are A_M^{n+1} and q_M^{n+1}. Two new ghost points $A_{M+1/2}^{n+1/2}$ and $q_{M+1/2}^{n+1/2}$ are introduced and Eq. (3.30)

can be solved numerically,when the binary tree outlet boundary condition is connected to the upstream large arteries. An iterative method is applied to solve for four unknowns A_M^{n+1}, q_M^{n+1}, $A_{M+1/2}^{n+1/2}$ and $q_{M+1/2}^{n+1/2}$.

3.4 A Comparative Study of 0-D and 1-D Outlet Boundary Conditions

To investigate the impact of two types of outlet boundary conditions on an upstream large artery, we connect two types of outlet boundary conditions to tapered straight vessels as illustrated in Figure 3.3. The top and bottom radii of the tapered straight vessels are 0.4 and 0.25 cm respectively and the length of the vessel is 100 cm. At the inlet, a physiological flow waveform with a flat velocity profile is imposed and scaled to provide a cardiac output (CO) of 3.228 L/min. In each study case, the three-element Windkessel outlet boundary condition or the binary tree outlet boundary condition is specified at the end of the vessels. The root impedance is set to be zero and the length-to-radius parameter is 50 for the binary tree outlet boundary condition, while the impedance parameters of three-element Windkessel boundary condition are $R_1 = 4860$ gs^{-1}cm^{-4},$R_2 = 540$ gs^{-1}cm^{-4} and $C_t = 5.3384e-6$ cm^{4}s^{2}g^{-1}.

The simulation starts at rest and the mean pressure reaches an oscillating steady state condition after carrying out two cycles. The academic package MATLAB R2019b is used to run all simulations. The second-order accuracy finite difference method is used for time integration with a time step of $5e^{-5}$ s and a spatial step size of 0.5 cm.

It can be clearly observed from Figure 3.4 that the impedance of the 1-D outlet boundary condition exhibits more oscillations (wave reflections) originating from the downstream vascular networks. Additionally, it is demonstrated that the impedance curve of the 1-D outlet boundary condition aligns more closely with physiological measured data [23]. In contrast, the fitted impedance curve of the 0-D outlet boundary condition appears much smoother.

We are also interested in exploring to what extent these two types of boundary conditions contribute to the pressure waveform of the upstream large artery.

Figures 3.5 and 3.6 present the pressure and blood flow waveform from upstream large artery when connected to two types of outlet boundary conditions. In Figure 3.5, the pressure and blood flow waveform is measured at $z = 40$ cm, while in Figure 3.6, the pressure and blood flow waveform is measured at $z = 60$ cm. It can be observed that the pressure profile gains noticeable oscillation from downstream vascular arterioles modeled by both types of outlet boundary conditions. However, Figures 3.5 and 3.6 reveal that the 0-D boundary condition and the 1-D boundary condition contribute little differences in terms of both amplitude and phase changes in the pressure and blood flow profile of the upstream large artery.

As discussed in Chapter 3.3.1, we employed the long-wave approximation to simplify the governing equations and obtain solutions. It is important to note that, for the long-wave approximation to be valid, the length of the tube should be sufficiently long compared to its radius. However, the length of the cerebral large artery is short, below 10 cm, which does not meet the requirements for the long-wave approximation when using the 1-D outlet boundary condition. Considering the flexibility and the ability to provide similar wave reflection effects from the downstream vascular network, we decide to employ the 0-D outlet boundary conditions for our patient-specific case. Nonetheless, it is worth mentioning that the 1-D outlet boundary condition is widely used for cardiovascular disease [24] and pulmonary disease [63].

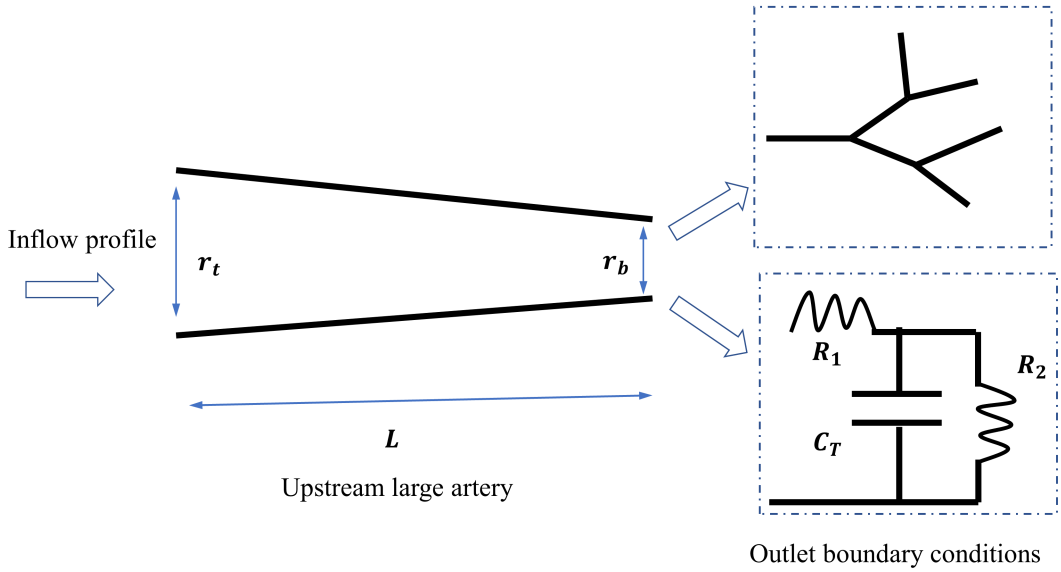

Figure 3.3 Illustration of two types of outlet boundary conditions connected to an upstream large artery

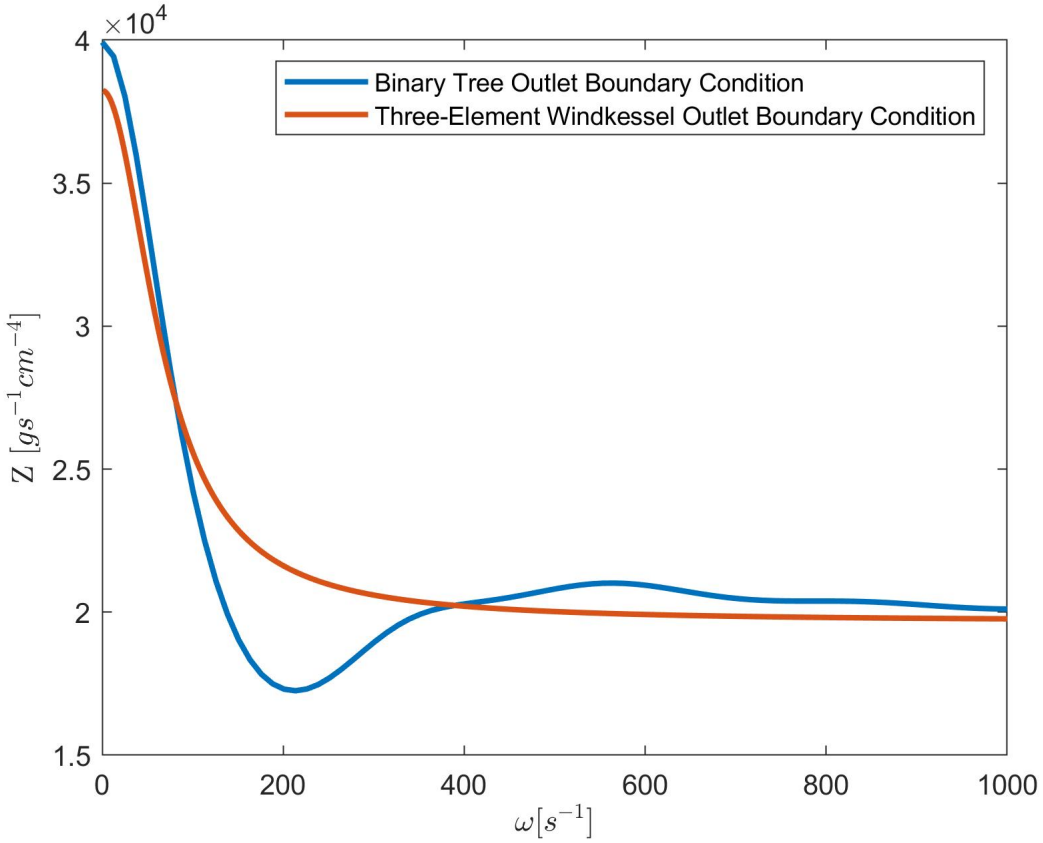

Figure 3.4 Blue line: Impedance solved from 1-D outlet boundary conditions; Red line: Fitted impedance for comparison purposes

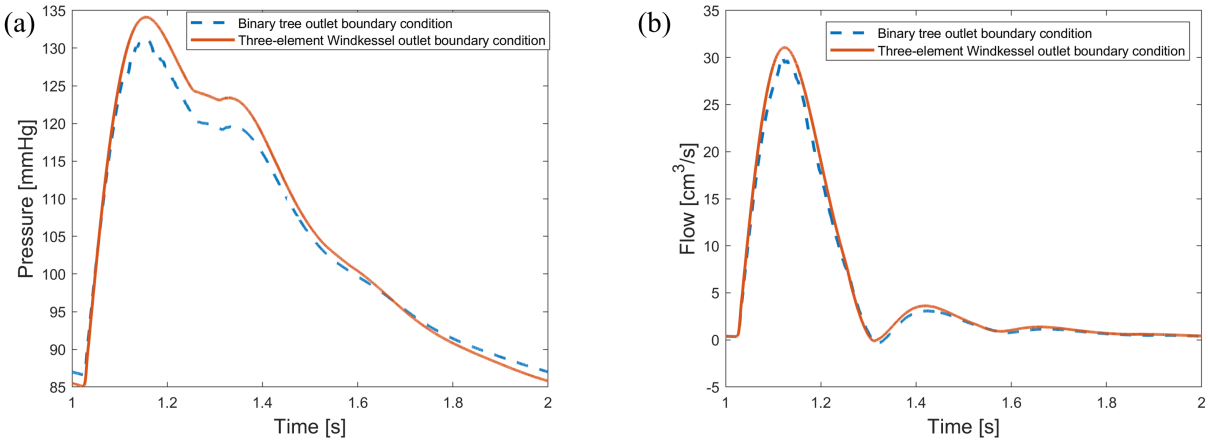

Figure 3.5 Comparison of two types of boundary conditions at $x = 40$ cm: (a) pressure profile; (b) blood flow profile

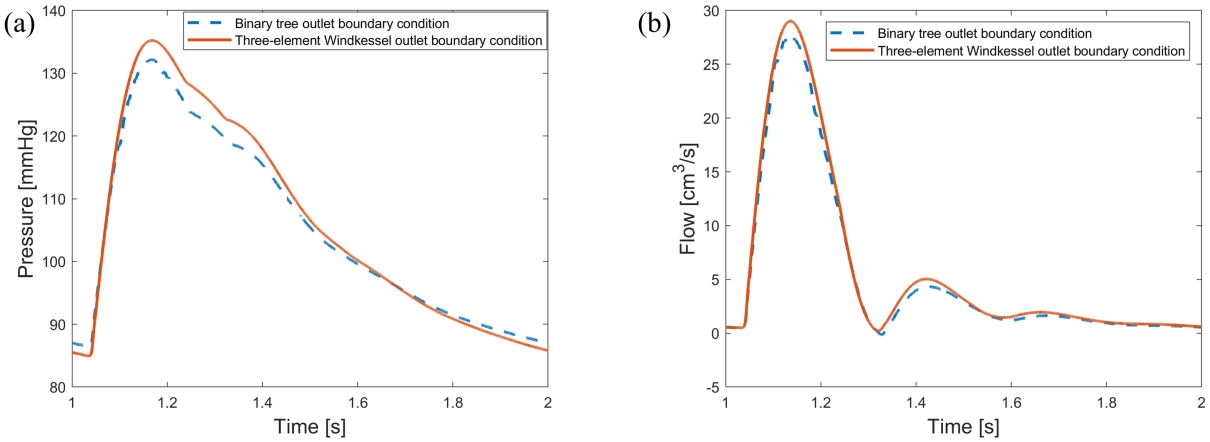

Figure 3.6 Comparison of two types of boundary conditions at $x = 60$ cm: (a) pressure profile; (b) blood flow profile

3.5 Sensitivity Analysis of 0-D Outlet Boundary Parameters

In this work, we aim to investigate the impact of resistance and compliance parameters on the pressure and blood flow waveforms of upstream large artery. We consider two resistances, R_1 and R_2, along with one compliance parameter, C_t. The original compliance is set to at the scale of $1e^{-6}$. Figure 3.7 illustrates the pressure and blood flow profiles of upstream large artery when we increase the scale of compliance to $1e^{-5}$ and decrease it to $1e^{-7}$. These variations in compliance scale allow us to assess its influence on the upstream large artery pressure and blood flow profile. Regarding to resistances, R_1 take places a significant portion of the total resistance in the configuration. Figure 3.8 demonstrates the impact of the resistance on the upstream large artery pressure and blood waveforms, when we increase and decrease R_1 by 20%. These variations allow us to gain insights into the influence of resistance on the pressure and blood flow profiles of upstream large artery.

Figure 3.7 shows that the amplitude of the three cases does not vary significantly, but noticeable phase change can be observed especially from blood flow profile. In Figure 3.8 , it can be seen that both the pressure and blood flow profile undergo significant changes in amplitude. Additionally, increasing the resistance of R_1 introduces more oscillations in diastole, as observed in the pressure waveform profile. The sensitivity analysis aligns with the role of resistance and compliance in our 0-D outlet boundary condition. The compliance has an impact on the phase change of impedance, as it serves as a crucial factor in modeling the elasticity of the vessel wall. The diverse elasticity of the vessel wall give rise to the phase variations in the blood flow profile of upstream large artery. On the other hand, the total resistance affects the amplitude of the waveform as it reflects the resistance encountered by the blood flow. Thus, changes in resistance can lead to the decrease or increase in the amplitude of pressure waveform of the upstream large artery.

(a) (b)

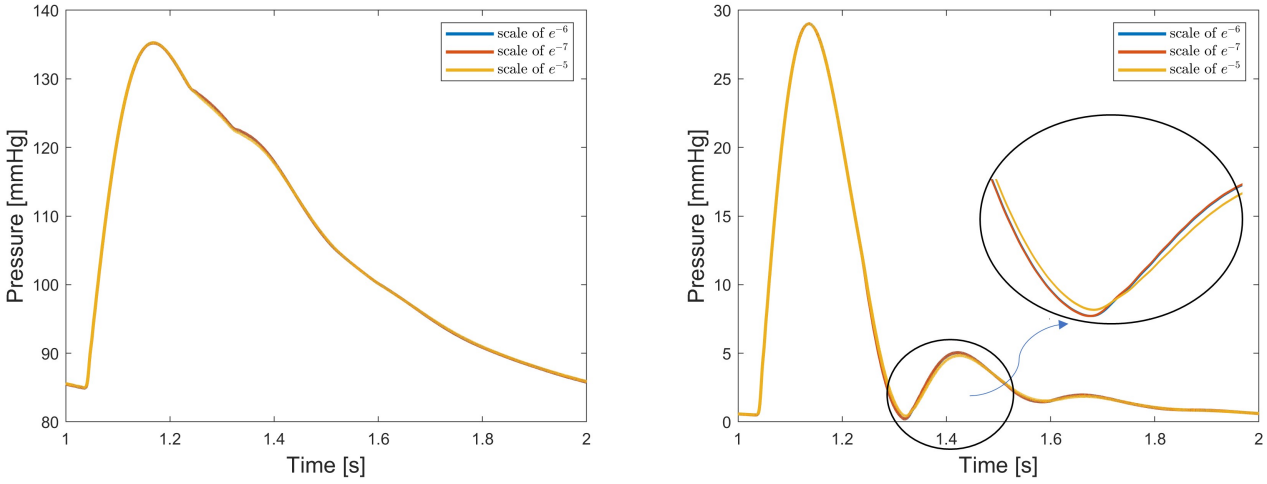

Figure 3.7 Sensitivity analysis on compliance: (a) pressure profile at $z = 60$ cm; (b) blood flow profile at $z = 60$ cm

(a) (b)

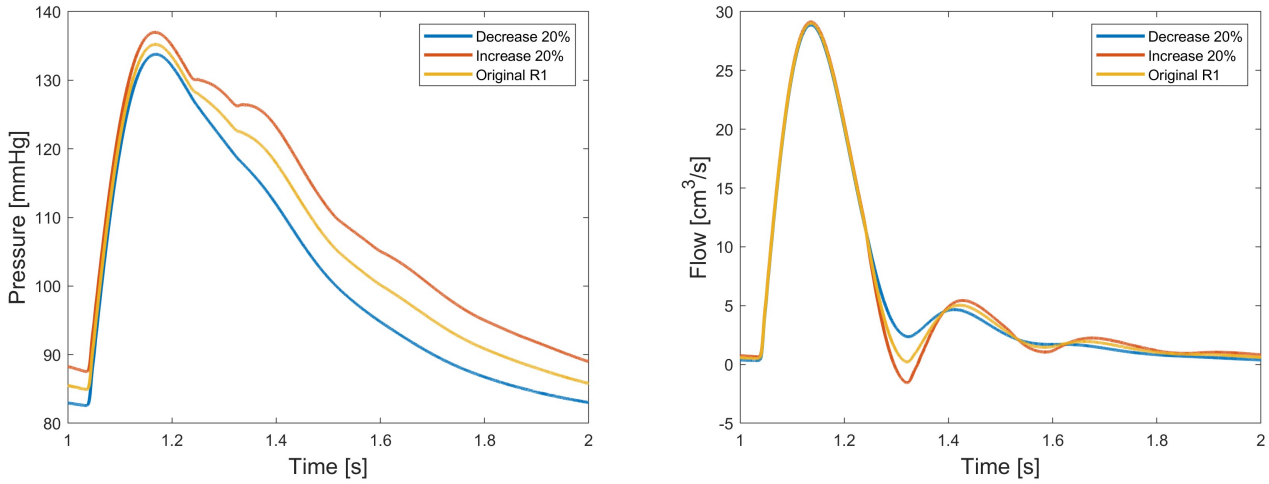

Figure 3.8 Sensitivity analysis on resistance R_1: (a) pressure profile at $z = 60$ cm; (b) blood flow profile at $z = 60$ cm

3.6 A Comparative Study of Numerical Results and Analytical Solutions

In this section, our aim is to validate the numerical outcomes presented in Chapter 3.4 through comparison with established analytical solutions. For simplicity purposes, we utilize the numerical results obtained from the single straight vessel attached to the 0-D outlet boundary condition, as discussed in Chapter 3.4. Given the complexity of deriving an exact solution for pulsatile flow within an elastic pipe, we choose to validate our numerical results by contrasting our findings with the exact solution proposed by Womersley in 1954 for pulsatile flow within a rigid pipe [64].

We start with the axial component of the 2-D Navier-Stokes equations. To further simplify the governing equations, the nonlinear term in Eq. (2.1) is neglected. The simplification results in the governing equations for describing pulsatile flow within a rigid pipe,

$$\frac{\partial u_z}{\partial t} = \frac{-1}{\rho}\frac{\partial p}{\partial z} + \frac{\mu}{\rho}\left(\frac{1}{r}\frac{\partial u_z}{\partial r} + \frac{\partial^2 u_z}{\partial r^2}\right) \tag{3.30}$$

Given the periodic nature of both pressure and blood flow, it becomes feasible to express the pressure gradient as follows,

$$\frac{\partial p}{\partial z} = Ae^{i\omega t} \tag{3.31}$$

We assume the solution of velocity is periodic in time and it has the similar form with the pressure gradient,

$$u_z\left(r,t\right) = ue^{i\omega t} \tag{3.32}$$

The governing equation becomes Eq. (3.26) when we plug Eq. (3.25) into the governing equation, Eq. (3.23),

$$\frac{d^2u}{dr^2} + \frac{1}{r}\frac{du}{dr} - \frac{i^3\omega}{\nu}u = \frac{-A}{\mu} \tag{3.33}$$

Womersley first proposed the solution of axial velocity u_z of Eq. (3.26) in 1954 and it has the form,

$$u_z = \frac{A}{\rho\omega}\left(1 - \frac{J_0\left(\alpha y i^{3/2}\right)}{J_0\left(\alpha i^{3/2}\right)}\right)e^{i\omega t} \tag{3.34}$$

whereα is an dimensionless parameter, which is called Womersley number [64],

$$\alpha = R\sqrt{\frac{\omega}{\nu}} \tag{3.35}$$

J_0 is a Bessel function of order zero; $y = \frac{r}{R}$ is a dimensionless parameter and R is the radius of the pipe.

We adopt an identical initial configuration to the straight vessel connected to a 0-D outlet boundary condition, as elaborated in Chapter 3.4. The radius of the pipe is 0.4 cm and the length of the pipe is 4 cm. The outlet is free with weakly imposed pressure equal to zero. To facilitate a more precise comparison between numerical and analytical results, the length of the pipe for Wormersley flow is relatively short. This adjustment aims to mitigate the impact of outlet boundary conditions on the upstream straight vessel flow waveform.

The flow comparison result is presented in Figure 3.9. It can be seen that the amplitude difference between the two outcomes is relatively minor, accompanied by observable phase variation. The minor amplitude difference may result from the outlet boundary reflection effects. The phase shift arises due to the different assumptions about the pipe wall: the analytical solution presumes a rigid pipe, whereas the numerical solution correspond to an elastic tube. As emphasized earlier, it is very hard to find an analytical solution for pulsatile flow within an elastic tube. Thus, we employ the classical Womersley analytical solution to compare with our numerical results. The comparison shows that phase shift is observed between the numerical result and the analytical solution, which is reasonable.

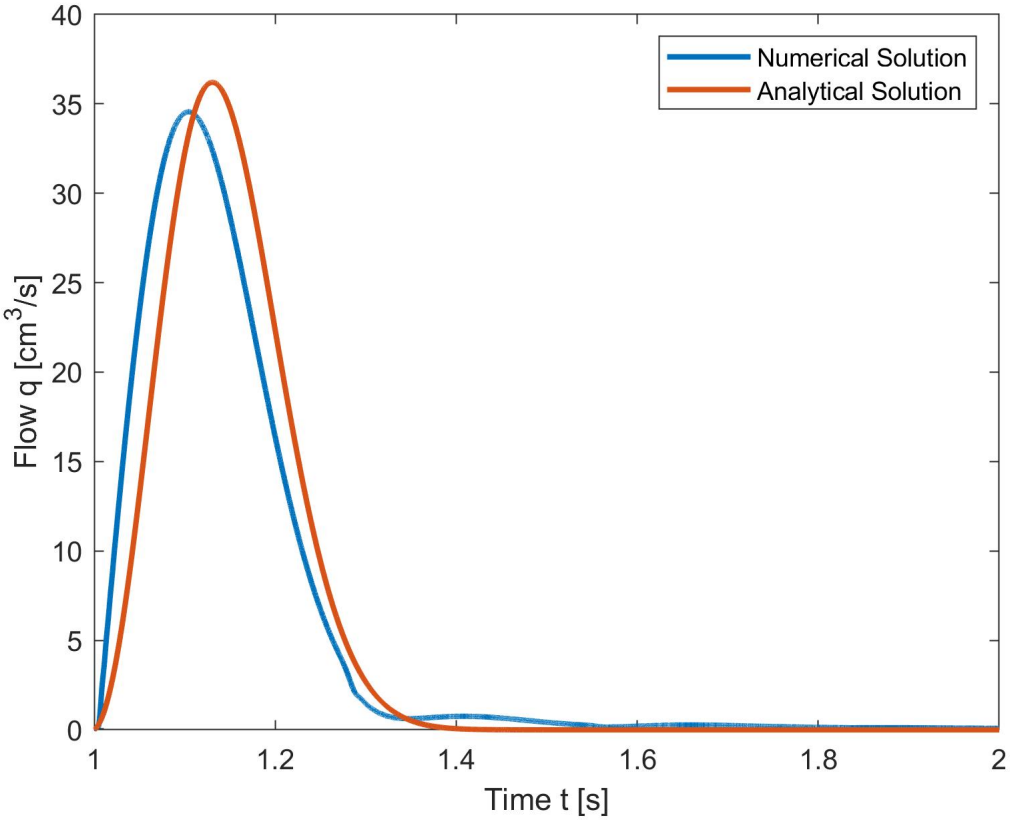

Figure 3.9 A comparative study between the numerical result and the analytical solution of flow waveform

Chapter Four

Patient-Specific Modeling of Circle of Wills

4.1 The Review of Patient-Specific Modeling

Patient-specific modeling is the development of computational models of human pathophysiology that are individualized by using patient-specific data [65]. The method has the potential to improve diagnosis (noninvasive measurement of blood pressure and velocity at the same site) and optimize clinical treatment by predicting surgical outcomes. The process typically contains image processing and segmentation from the medical image data and performs CFD simulation based on the extracted parameters from a series of medical image data.

The patient-specific modeling was first applied in the 1960s to compute blood pressure for an idealized and generic model. As imaging techniques are being developed, especially the emergence of MRI (magnetic resonance image) and CTA (computed tomography angiography), it is now possible to reconstruct patient-specific anatomic and physiological models. In the 1990s, many groups started to use image-based modeling technologies to simulate the blood flow [66, 67, 68]. Since then, the patient-specific model has been used to investigate the occlusion in the coronary arteries [69], the aorta [70], and the rupture of aneurysms [71]. The workflow is illustrated in Figure 4.1.

In this work, we utilize patient-specific data extracted from CT scans to construct our numerical model. The individualized data provide us with reliable results and help us investigate

human pathophysiology and optimize clinical treatment.

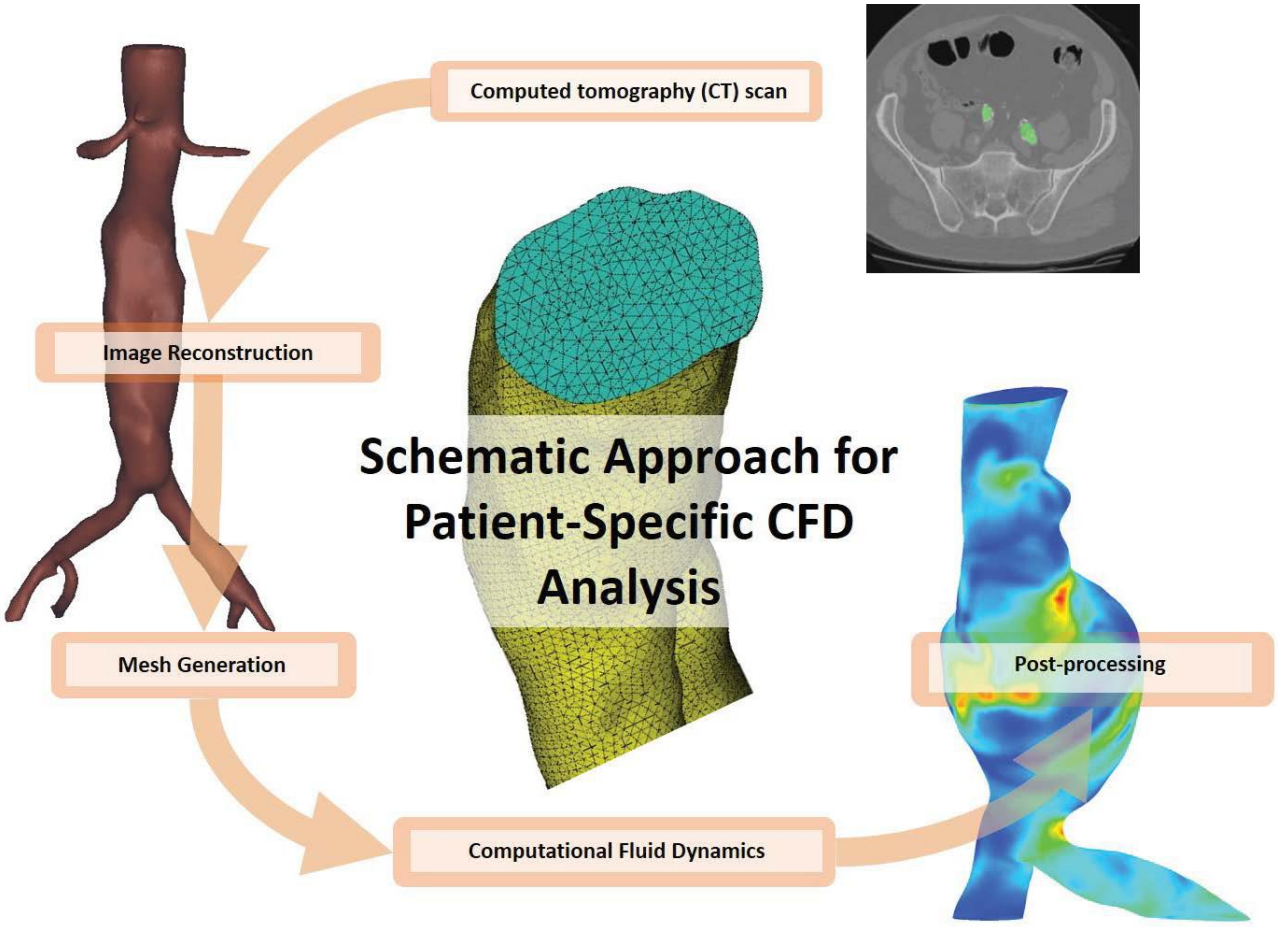

Figure 4.1 Schematics approach for patient-specific CFD analysis](Graph from [72])

4.2 Extract Parameters of Circle of Wills

We generate a network of the Circle of Wills (CoWs) from a series of contract CT scan and CT scan, which is available online (see https://github.com/lassoan/SlicerSegmentationRecipes) [73]. The series of CT scans are imported to the open-source segmentation software 3D Slicer (see http://www.slicer.org) for reconstruction, segmentation and extracting centerlines [73].

The series of contrast CT scans and baseline CT scans are imported into 3D Slicer and reconstructed with bone and tissues. The Vesselness Filtering Toolbox is used to indicate and enhance the vessels from the bones and tissues. The Segmentaion Toolbox allows us to segment the cerebral vascular network from the bones and tissues. As this work only focuses on part of the CoWs, we identified the large arteries: internal carotid artery (ICA), middle cerebral artery (MCA), anterior cerebral artery (ACA) and posterior communicating artery (Pcomm). Next, we manually segmented all other segmental vessels and small arterioles.

The 1-D network model is reduced from the reconstructed 3-D network by extracting centerlines using Vascular Modeling ToolKit (VMTK) [74]. In this 1-D network, ICA is a nonterminal vessel, which is connected to the inlet of terminal vessels MCA, ACA and PComm. The nonterminal vessel is defined as the parent vessel while the terminal vessel is defined as the daughter vessel. The mean radius and length of each vessel are computed from extracted centerlines automatically, which is shown in Table 4.1. Figure 4.2 presents the original series contrast CT scan, the reconstructed 3D segmented network and the extracted centerlines.

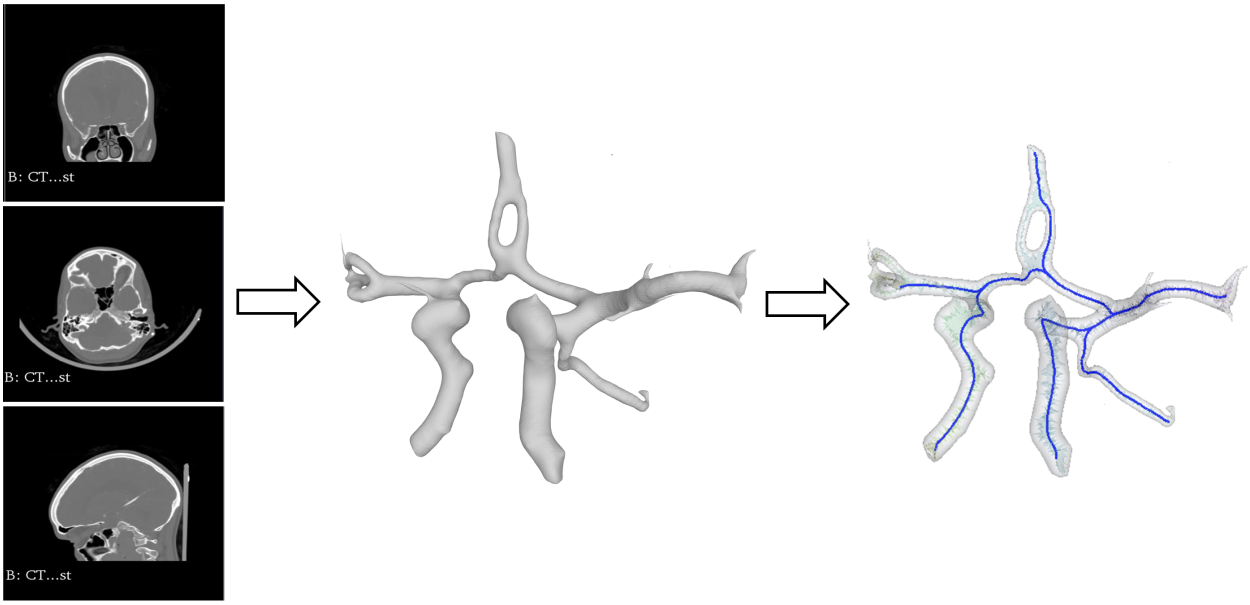

Figure 4.2 Schematic of model development, from series of contrast CT images to segmentation and centerlines

Table 4.1 Arterial length and radius

Arterial segment name	Arterial length L (mm)	Arterial radius r_0 (mm)
Internal Carotid Artery	48.85	2.21
Middle Cerebral Artery	41.93	1.58
Anterior Cerebral Artery (A1)	19.65	1.33
Anterior Cerebral Artery (A2)	12.35	1.31
Posterior Communication Artery	21.77	1.11

Chapter Five

Wave Reflection and Variations

5.1 The Review of Bifurcations

As discussed in Chapter 1.2.4, wave reflection can arise at any point of changes along the arterial system. The cerebral artery is not always a straight vessel; instead, there are many slight bends and unevenness along the cerebral vascular system that can cause wave reflection. However, the most significant wave reflection occurs at the junctions of the vessels. The incident wave traveling from the parent vessel is partially reflected at the junction, and the other part travels down to the daughter vessels and becomes transmitted waves. In order to better simulate the wave reflection phenomenon of the downstream vascular network and acquire more realistic pulsatile pressure and blood flow waveform profiles of the upstream large artery, we will incorporate the effect of bifurcation in our study.

Bifurcation occurs at the point where the outflow of the parent vessel is balanced with the inflow of two or three daughter vessels. It is assumed that there is no leakage at the point of bifurcation [56]. What's more, it is also assumed that the pressure differential across a location where a branch diverts from the main stem is small and can be neglected [75]. Although there might be a mismatch in the radii of the parent vessel and the daughter vessel, it will not cause significant energy loss when the wave is transmitted.

In order to investigate the effect of the communicating artery PComm on the collateral circulation of CoWs, we have constructed two bifurcation models. One model does not

include the communicating artery PComm, which will be discussed in Chapter 5.2. The other model includes the communicating artery PComm, which will be introduced in Chapter 5.3. Therefore, in Chapter 5.2, a model containing one upstream parent vessel ICA and two daughter vessels (MCA and ACA) is constructred, and in Chapter 5.3, a model consisting of one upstream parent vessel ICA and three daughter vessels (MCA, ACA and PComm) is constructed.

5.2 Bifurcation with Two-Daughter-Vessel Model

In the two-daughter bifurcation model, the upstream parent vessel ICA is connected to two downstream daughter vessels MCA and ACA. To model the downstream vascular wave reflection behavior stably and accurately, we applied the three-element Windkessel outlet boundary conditions at the end of each daughter vessel. The inlet blood flow profile is calibrated at the ICA using color-coded duplex ultrasound in young healthy volunteers, as shown in Figure 5.1 [76]. Figure 5.1 illustrates the network including bifurcation. Two additional governing equations are applied to ensure conservation law at the bifurcation [56].

$$\left(q^P\right)_M = \left(q^{d_1}\right)_0 + \left(q^{d_2}\right)_0 \tag{5.1}$$

$$\left(p^P\right)_M = \left(p^{d_1}\right)_0 = \left(p^{d_2}\right)_0 \tag{5.2}$$

where q_M^P is the outflow from the parent vessel ICA; $q_0^{d_1}$ is the inflow from the daughter vessel MCA; $q_0^{d_2}$ is the inflow from the daughter vessel ACA.

To connect two daughter vessels and solve for the flow q and pressure p at the junction, we introduce ghost points at the end of the upstream parent vessel $(A_M^p)^{n+1/2}$, $(q_M^p)^{n+1/2}$, and at the start of downstream daughter vessels $(A_M^{d1})^{n+1/2}$, $(q_M^{d1})^{n+1/2}$, $(A_M^{d2})^{n+1/2}$, $(q_M^{d2})^{n+1/2}$. The governing equations, Eq. 2.17 and Eq.5.1 – 5.2, are solved by the two-step Lax-Wendroff method with 18 equations and 18 unknowns. The modeling and solution method of a single vessel has been introduced in the previous section. At each time step, (i) the interior points

of both the parent vessel and daughter vessels are solved separately; (ii) the results from all vessels are constrained by the conservation law, and the bifurcation point is solved iteratively; (iii) the inlet and outlet boundary conditions are attached at the start of the parent vessel and the end of the daughter vessel, respectively.

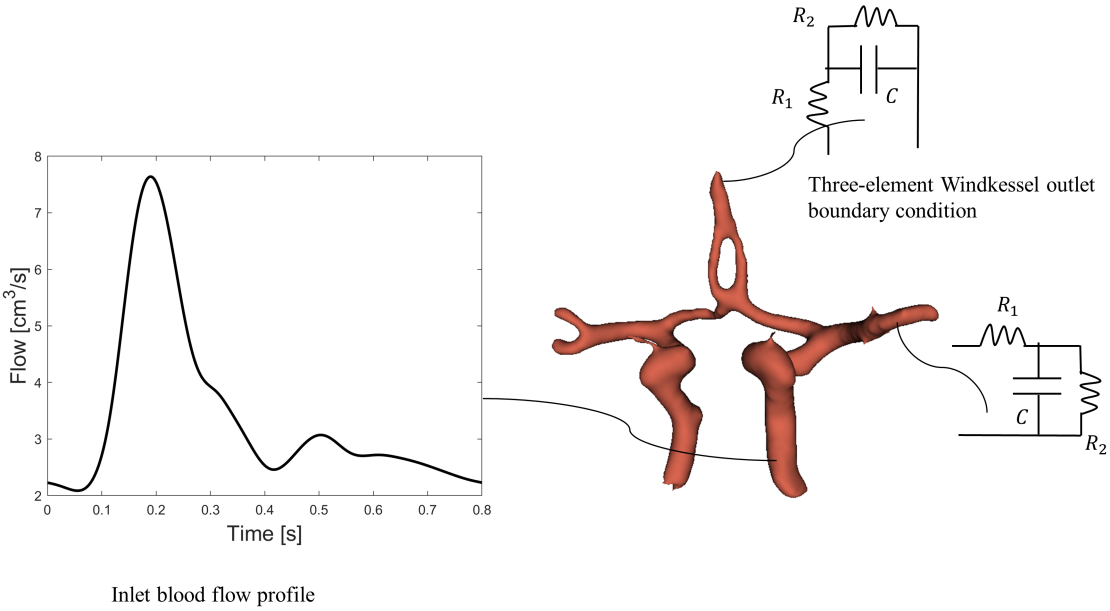

Figure 5.1 Illustration of two-daughter-vessel bifurcation model

5.3 Bifurcation with Three-Daughter-Vessel Model

In the three-daughter bifurcation model, the upstream parent vessel ICA is connected to three downstream daughter vessels MCA, ACA and PComm. The three-element Windkessel outlet boundary condition is attached to the end of each daughter vessel, while the inlet blood flow profile is prescribed at the start of the parent vessel. Figure 5.2 visually represents the network with the bifurcation included. In order to ensure conservation laws at the bifurcation, two additional governing equations are applied [56].

$$\left(q^{P}\right)_{M} = \left(q^{d_1}\right)_{0} + \left(q^{d_2}\right)_{0} + \left(q^{d_3}\right)_{0} \tag{5.3}$$

$$\left(p^{P}\right)_{M} = \left(p^{d_1}\right)_{0} = \left(p^{d_2}\right)_{0} = \left(p^{d_3}\right)_{0} \tag{5.4}$$

where q_M^P is the outflow from parent vessel ICA; $q_0^{d_1}$ is the inflow from the daughter vessel MCA; $q_0^{d_2}$ and $q_0^{d_3}$ are the inflow from daughter vessels ACA and PComm.

To connect three daughter vessels and solve for the flow q and pressure p at the junction, we introduce ghost points at the end of the upstream parent vessel $(A_M^p)^{n+1/2}$ and $(q_M^p)^{n+1/2}$, and at the start of downstream daughter vessels $(A_M^{d1})^{n+1/2}$, $(q_M^{d1})^{n+1/2}$, $(A_M^{d2})^{n+1/2}$, $(q_M^{d2})^{n+1/2}$, $(A_M^{d3})^{n+1/2}$, $(q_M^{d3})^{n+1/2}$. The governing equations, Eq. (2.17),Eq. (5.3) and (5.4), are solved by the two-step Lax-Wendroff method with 24 equations and 24 unknowns. The modeling and solution method process is similar to the previous case discussed in Chapter 5.2. A detailed derivation process is provided in Appendix A.1.

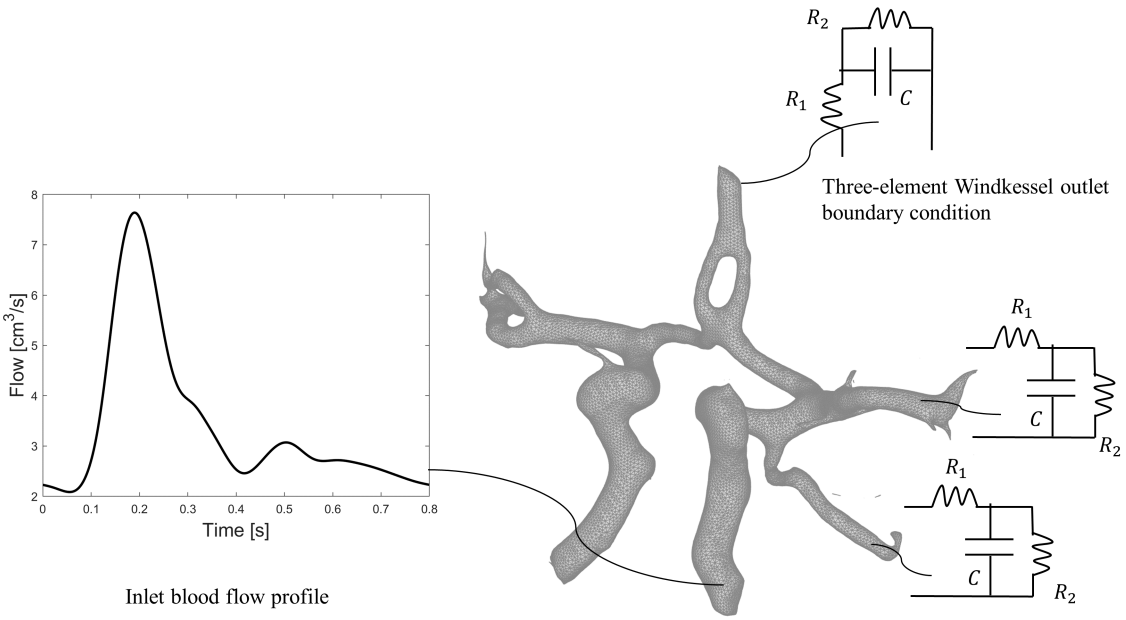

Figure 5.2 Illustration of three-daughter-vessel bifurcation model

5.4 Wave Intensity Analysis

Wave intensity analysis (WIA) is one method used for the analysis of 1-D pulse transmission. WIA was introduced for the decomposition of forward and backward traveling waves [77].It is an alternative time domain method based on the method of characteristics. WIA allows people to capture the temporal events at any site along the circulatory system, without assuming the linearity or periodicity. Wave Intensity (WI) is computed as the product of the blood pressure change and the velocity change during short time intervals [78]. A positive value of WI indicates that forward-traveling waves predominate while a negative value indicates that backward-traveling waves predominate. Since WI is in units of power per area (an index of energy per unit area carried by waves), the WIA method can determine the wave directionality as well as the magnitude of the energy transferred by the waves [78]. WIA has been used in hemodynamic studies throughout the circulatory network including the ascending aorta [79], common carotid artery [80], coronary arteries [81] and systemic arterial system [82, 83]. It has demonstrated promising abilities in providing clinical insights useful for early diagnosis in cardiovascular and cerebrovascular diseases.

WIA is based on the method of characteristic. The forward dI_+ and the backward wave intensity dI_- can be represented by [84],

$$dI_+ = \frac{1}{4\rho c}\left(dP + \rho c\, dU\right)^2 \tag{5.5}$$

$$dI_- = \frac{1}{4\rho c}\left(dP - \rho c\, dU\right)^2 \tag{5.6}$$

where dI is defined as the WI in units of power per unit area (W/m^2); c is the wave speed and $c = \sqrt{\frac{A}{\rho}\frac{\partial P}{\partial A}}$; dP and dU are incremental changes in pressure and velocity acquired through the 1-D network; and ρ is the density of the blood flow.

The forward and the backward wave intensities can be further decomposed based on the compression and expansion waves. In normal circulation, forward compression waves (FCW) originate from the right cardiac ventricle, increasing pressure and accelerating flow as blood

travels toward the periphery. Forward expansion waves (FEW) originate from the proximal arteries, decreasing the pressure and flow velocity. In contrast, backward compression waves (BCW) travel from the periphery to the heart, increasing pressure and decelerating flow. Backward expansion waves (BEW) travel from the periphery to the heart, decreasing pressure and increasing flow [85]. Understanding the physics of these forward and backward waves is necessary for extracting physiological information relevant to clinical practice.

In this work, WIA is performed using the numerical results of blood pressure, wave speed and blood flow profiles. The forward and backward wave intensities are further separated into FCW, FEW, BEW and BCW, which are used to investigate the downstream vascular network behavior and elucidate the relationship between MCA stenosis and the formation of collateral circulation.

5.5 Results

This chapter presents the results of both the two-daughter-vessel model and the three-daughter-vessel model. The two-daughter-vessel model consists of a parent vessel (ICA) connected to two daughter vessels (MCA and ACA). And the three-daughter-vessel model includes a parent vessel (ICA) connected to three daughter vessels (MCA, ACA and PComm). The inlet blood flow profile is specified at the start of the parent vessel ICA, and a three-element Windkessel outlet boundary condition is connected to the end of each daughter vessel. Parameters for ICA, MCA, ACA and PComm of three-daughter-vessel model are extracted from CT contrast images using 3D Slicer are listed in Table 4.1. For the two-daughter-vessel model, we use radius of 0.134 cm for MCA and 0.17 cm for ACA. The resistance and compliance for the three-element Windkessel outlet boundary conditions are provided in Table 5.1 [76].

In each simulation, the network starts at rest and the mean pressure reaches an oscillat-

ing steady- state condition after two cycles. The academic package MATLAB R2019b is used to run all simulations. The second-order accuracy finite difference method is used for time integration with a time step of 0.000016 s and a spatial step size of 0.1 cm for the three-daughter-vessel model. Doubling the number of spatial elements with a time step of of 0.000008 s reveals a maximum relative error less than 7% in the pressure waveform at the middle of MCA for the three-daughter vessel model.

Figures 5.3, 5.4 and 5.5 display the pressure and blood flow waveforms for ICA, MCA and ACA in the two-daughter-vessel bifurcation model. Figures 5.6 to 5.9 present the pressure and blood flow waveform for ICA, MCA, ACA and PComm in the three-daughter-vessel bifurcation model.

Table 5.1 Parameter values for outlet boundary conditions

Arterial segment name	Resistance R_1 ($g/cm\,s^4$)	Resistance R_2 ($g/cm\,s^4$)	Compliance C_T (cm^4s^2/g)
Middle Cerebral Artery	11,600	12,300	7.87e-5
Anterior Cerebral Artery	17,000	15,750	2.92e-4
Posterior Communicating Artery	34,000	31,500	5.84e-4

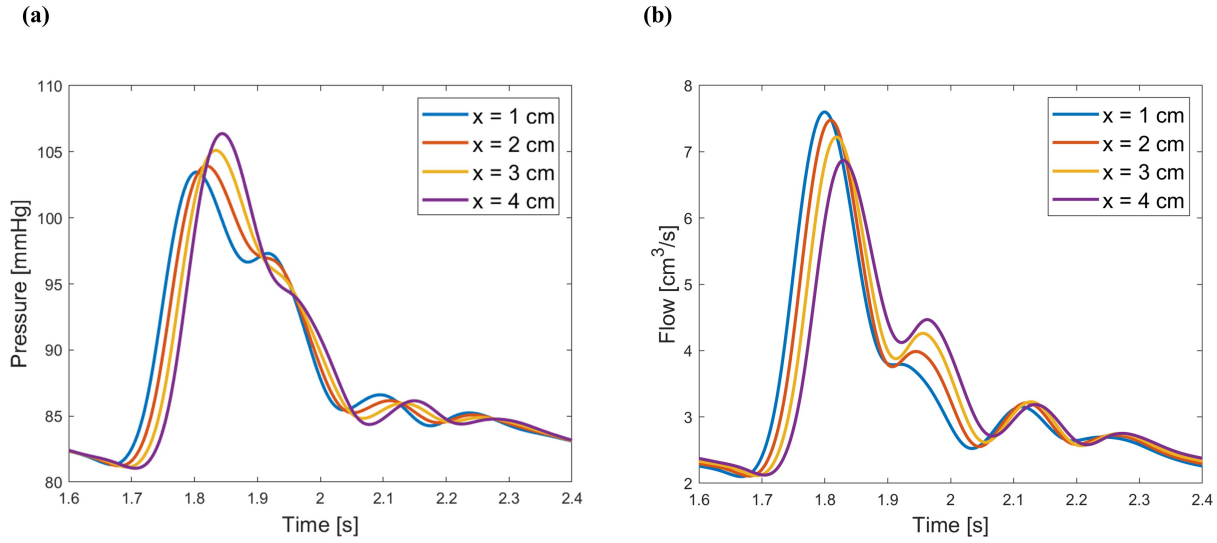

Figure 5.3 Two-daughter-vessel bifurcation model: (a) ICA pressure profile at $x = 1$ cm, 2 cm, 3 cm and 4 cm; (b) ICA blood flow profile at $x = 1$ cm, 2 cm, 3 cm and 4 cm

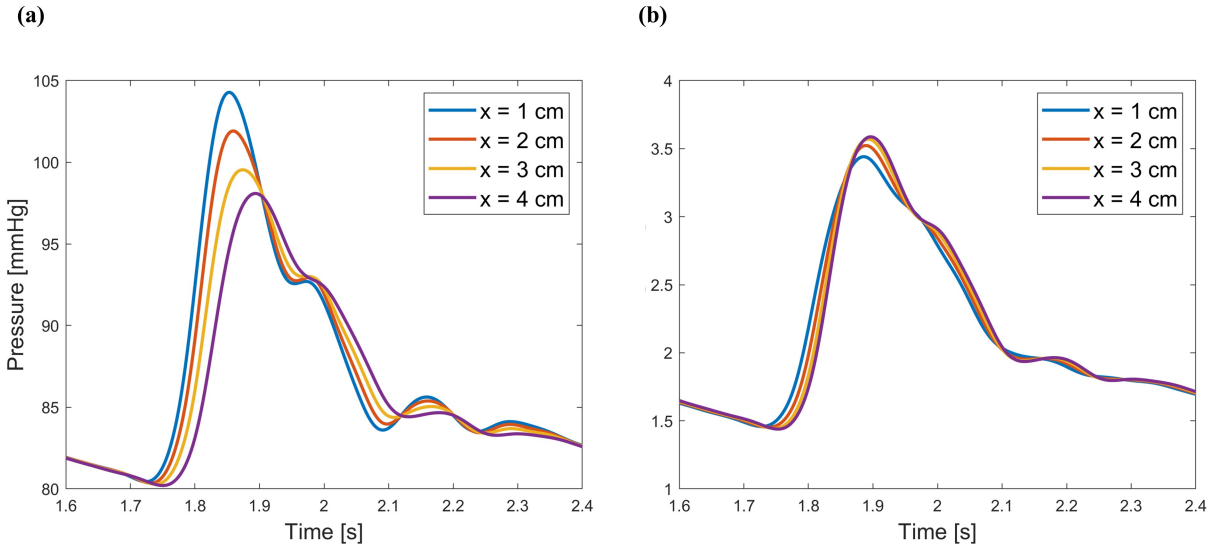

Figure 5.4 Two-daughter-vessel bifurcation model: (a) MCA pressure profile at $x = 1$ cm, 2 cm, 3 cm and 4 cm; (b) MCA blood flow profile at $x = 1$ cm, 2 cm, 3 cm and 4 cm

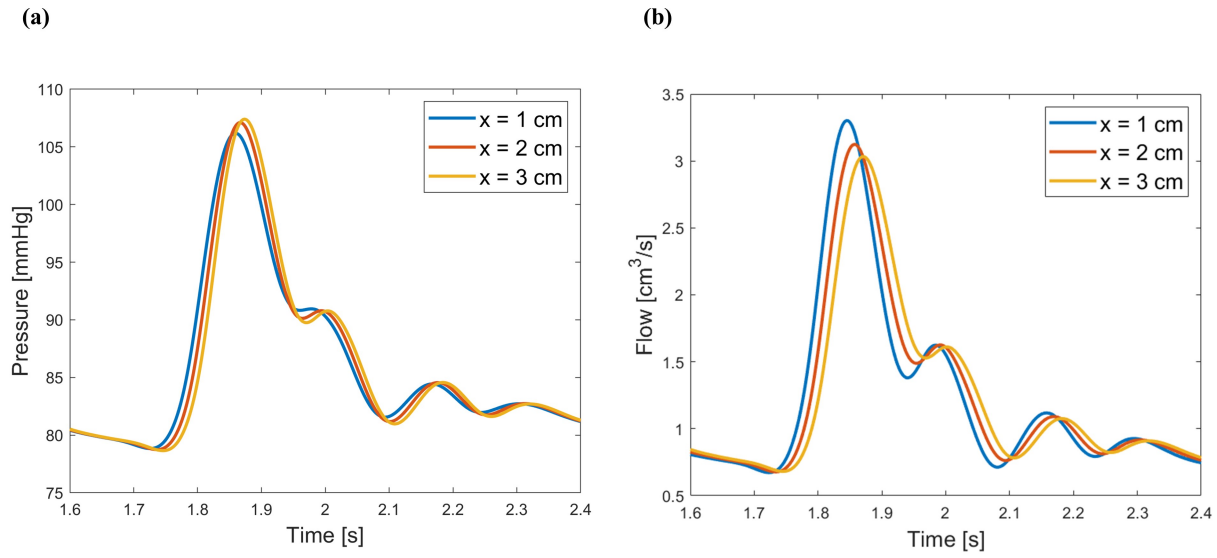

Figure 5.5 Two-daughter-vessel bifurcation model: (a) ACA pressure profile at $x = 1$ cm, 2 cm and 3 cm; (b) ACA blood flow profile at $x = 1$ cm, 2 cm and 3 cm

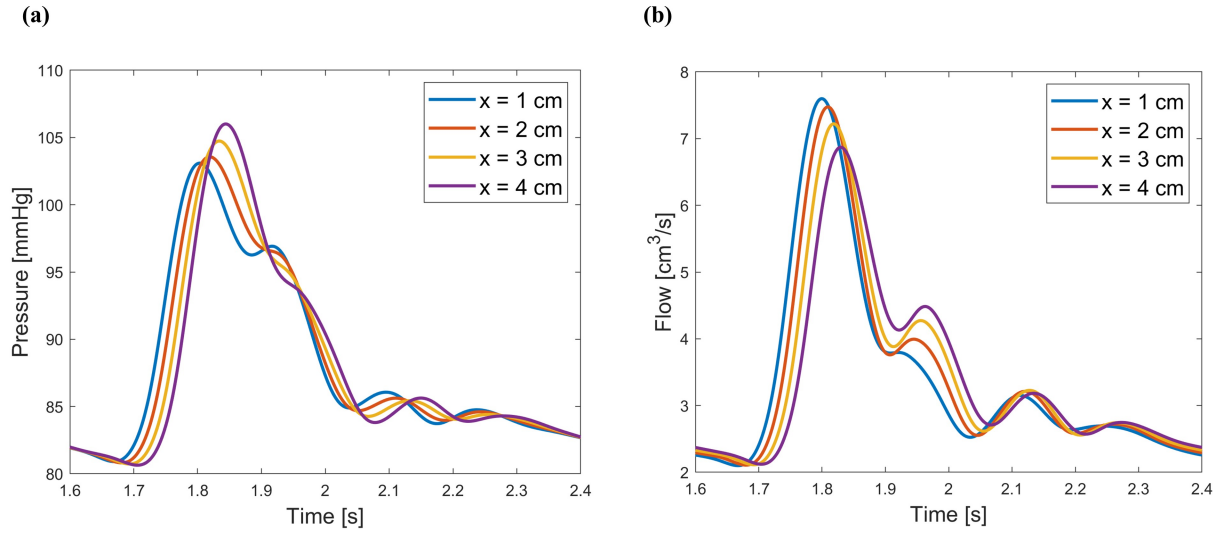

Figure 5.6 Three-daughter-vessel bifurcation model: (a) ICA pressure profile at $x = 1$ cm, 2 cm, 3 cm and 4 cm; (b) ICA blood flow profile at $x = 1$ cm, 2 cm, 3 cm and 4 cm

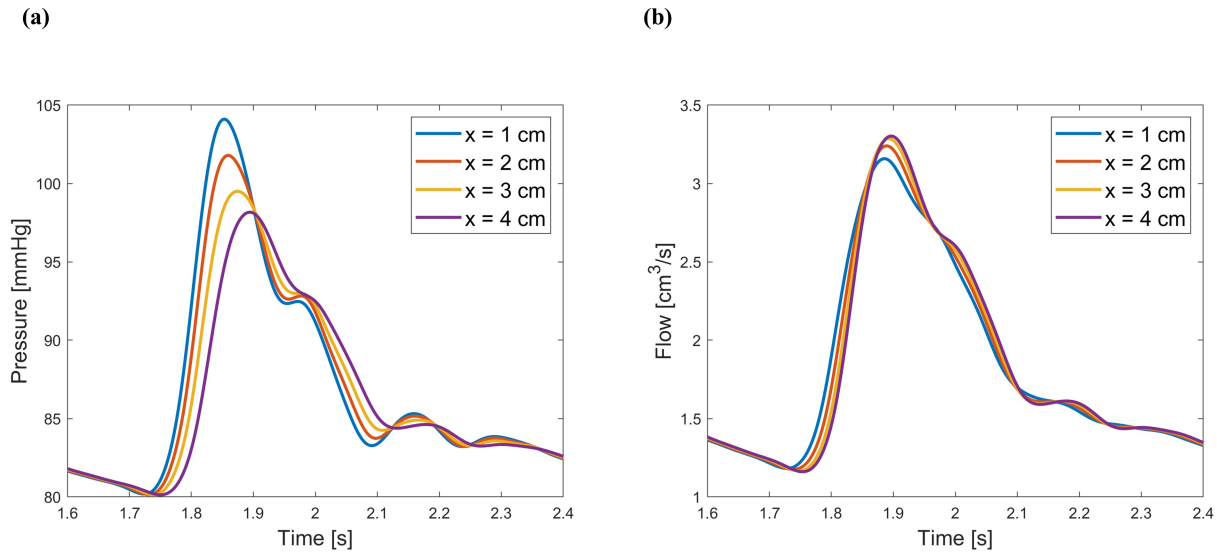

Figure 5.7 Three-daughter-vessel bifurcation model: (a) MCA pressure profile at $x = 1$ cm, 2 cm, 3 cm and 4 cm; (b) MCA blood flow profile at $x = 1$ cm, 2 cm, 3 cm and 4 cm

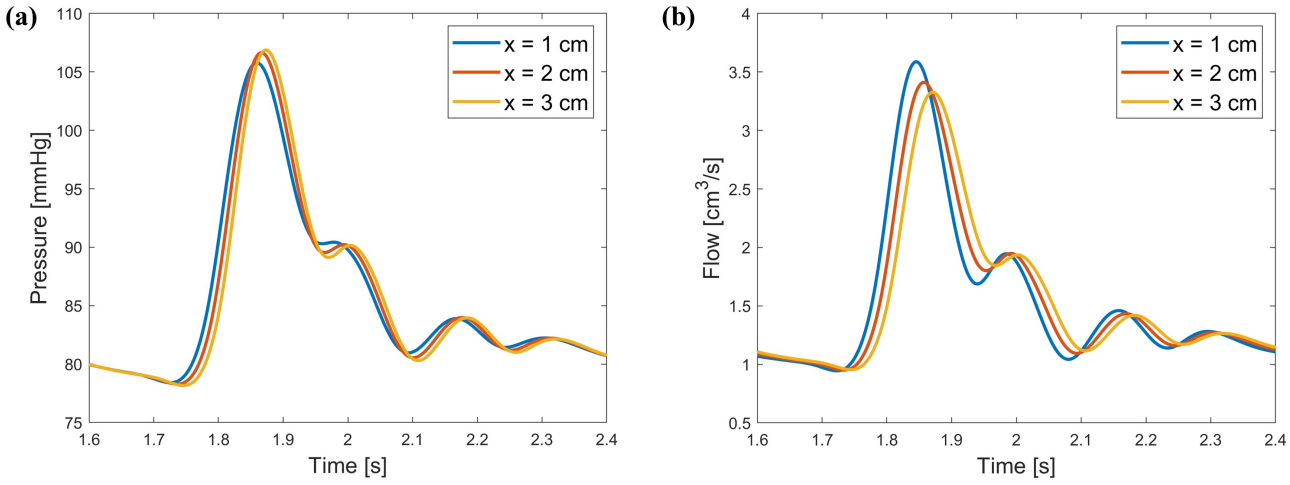

Figure 5.8 Three-daughter-vessel bifurcation model: (a) ACA pressure profile at $x = 1$ cm, 2 cm and 3 cm ; (b) ACA blood flow profile at $x = 1$ cm, 2 cm and 3 cm

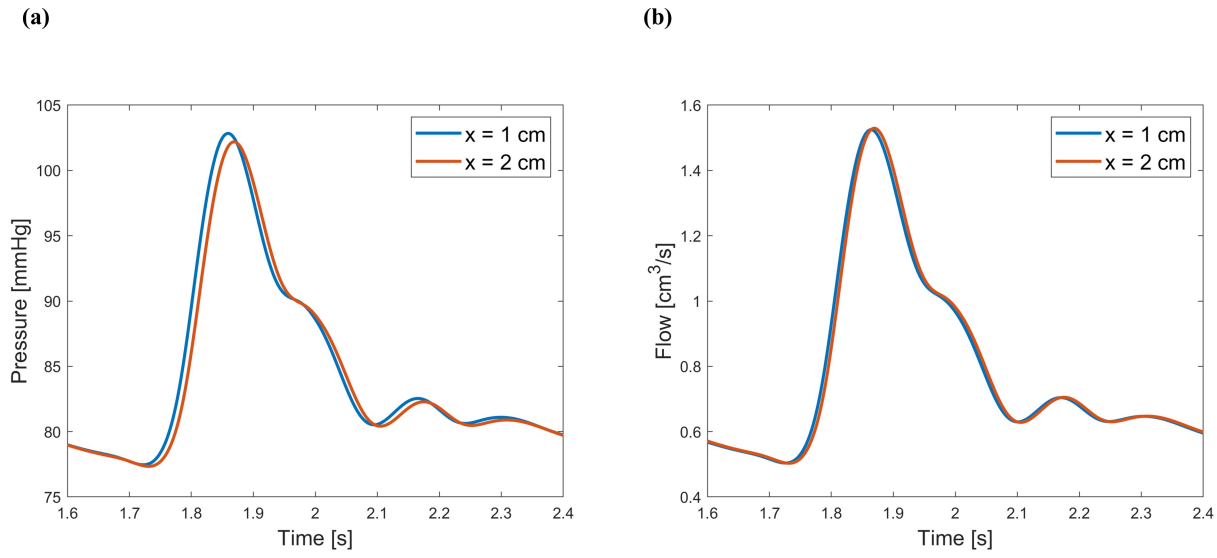

Figure 5.9 Three-daughter-vessel bifurcation model: (a) PComm pressure profile at $x = 1$ cm and 2 cm; (b) PComm blood flow profile at $x = 1$ cm and 2 cm

Chapter Six

Stenosis Model and Reverse Flow Investigation

6.1 The Review of Stenosis

Intracranial Stenosis refers to the severe narrowing of an intracranial artery, mainly occuring at ICA and the trunk of MCA. Patients with intracranial stenosis have a higher risk of stroke, with MCA stenosis having a yearly risk of at least 8% per year [86, 87, 88, 89]. Compared to extracranial carotid stenosis, MCA stenosis poses a higher risk of stroke [89, 90]. In this chapter, we will incorporate the effect of MCA stenosis in our network.

Collateral circulation plays a crucial role in stroke and ischemia , and CoWs constitute the primary cerebral collateral network. The formation of collateral circulation and the phenomeno of reverse direction of blood flow in collateral circulation have confused scientists for centuries [5]. As discussed in Chapter 1.2.2, the current hypothesis suggests that the blood flow can flow from PComm to MCA when MCA is largely occluded via downstream vascular network. Normal blood flow is piped from proximal large arteries to the distal small arteries by the high-pressure difference between the ventricle and the peripheral resistance. However, when MCA is largely occluded, blood flow is allowed to flow from distal small arteries to large cerebral arteries through the downstream vascular network. The pressure gradient between neighboring arteries and distal small arteries can cause changes in blood flow direction and rate, leading to the formation of collateral channels[91]. This process can take 1$\sim$4 seconds and it can be observed on the TCD monitor as an increase in artery flow

velocity. It is of great importance to model the effect of MCA stenosis and further investigate the collateral circulation phenomenon.

Several groups have used patient-specific computational models to study MCA stenosis. Park used ADINA commercial software to investigate severe M1 stenosis before and after stenting [92],while Lan investigated MCA stenosis and its relationship with collateral flow in ACA and PCA using ANSYS commercial software [93]. The energy loss stenosis model was first proposed by Tsai and Young [94]. Several studies have been performed, demonstrating that the 1-D stenosis simulation results exhibit little difference compared to 3-D stenosis model predictions [21]. The 1-D energy loss stenosis model has been applied to the whole circulatory system: including aortic [95], coronary [96], pulmonary [63] and carotid [97].

6.2 Stenosis for Two-Daughter-Vessel Bifurcation Model

Our mathematical model considers an intracranial stenosis of the proximal MCA, consistent with the post-bifurcation lesion type Mori proposed [98]. This is the most common types of lesions for M1 segment [99]. In this work, the post-bifurcation lesion for the MCA is considered and the lesion is modeled using the pressure loss term [94],

$$\Delta p = \frac{\mu K_\nu}{2\pi r_p^3} q + \frac{\rho K_t}{2A_p^2}\left(\frac{A_p}{A_s} - 1\right)^2 q\,|q| + L_s \frac{\rho K_u}{A_p}\frac{\partial q}{\partial t} \tag{6.1}$$

where A_p and r_p are the unobstructed cross-sectional area and unobstructed radius, respectively. The A_s is the obstructed cross-sectional area. The viscous loss, inertial force loss and turbulent loss are represented by K_v, K_u and K_t, respectively. And L_s is the stenosis length.

In Chapter 5, we constructed two models: a two-daughter-vessel bifurcation model and a three-daughter-vessel bifurcation model. In this chapter, we will include the stenosis into these two models. In the two-daughter-vessel bifurcation model, the parent vessel ICA is connected to two daughter vessels, MCA and ACA, with MCA being occluded. The stenosis

is modeled as a pressure drop for the downstream daughter vessel MCA. The pressure loss term introduced in Eq. (6.1) is combined with the bifurcation condition described in Eqs. (5.1) and (5.2). Therefore, the pressure loss term accounts for the energy loss, and governing equations become,

$$\left(q^P\right)_M = \left(q^{d_1}\right)_0 + \left(q^{d_2}\right)_0 \tag{6.2}$$

$$\left(p^P\right)_M - \Delta p^{d_1} = \left(p^{d_1}\right)_0 = \left(p^{d_2}\right)_0 - \Delta p^{d_1} \tag{6.3}$$

The governing equations provide 18 unknowns and 18 equations at the bifurcation between the parent vessel and daughter vessels. The detailed solution process is presented in Appendix A.2.

6.3 Stenosis for Three-Daughter-Vessel Bifurcation Model

The primary collateral circulation, which serves as a backup system of CoWs, consists of communicating arteries: PComm and AComm. PComm and AComm can preserve cerebral perfusion to avoid ischemic when a large artery supporting the CoWs is blocked or narrowed [6]. In healthy brains, there is no net flow of blood across the PComm and AComm [10]. However, when the large artery is occluded, a pressure gradient develops, making it necessary to study PComm and AComm. In this study, our goal is to investigate the collateral circulation through PComm when MCA is occluded through downstream vascular network. As the main focus is to investigate the relationship between MCA stenosis and formation of collateral circulation, we include the stenosis model in the three-daughter-vessel bifurcation model.

In this chapter, we will discuss the stenosis model included in the three-daughter-vessel bifurcation model. In this model, the parent vessel ICA is connected to three daughter vessels: MCA, ACA and PComm. Additionally, MCA is occluded while the other daughter vessels are not occluded. The stenosis is represented as a pressure drop for the downstream daughter

vessel, MCA. The pressure loss term in Eq. (6.1) is combined with the bifurcation condition, Eqs. (5.3) and (5.4), to account for the energy loss. The governing equations are modified as follows,

$$\left(q^{P}\right)_{M} = \left(q^{d_1}\right)_{0} + \left(q^{d_2}\right)_{0} + \left(q^{d_3}\right)_{0} \tag{6.4}$$

$$\left(p^{P}\right)_{M} - \Delta p^{d_1} = \left(p^{d_1}\right)_{0} = \left(p^{d_2}\right)_{0} - \Delta p^{d_1} = \left(p^{d_3}\right)_{0} - \Delta p^{d_1} \tag{6.5}$$

The governing equations provide 24 unknowns and 24 equations at the bifurcation between parent vessel and daughter vessels. The detailed solution process is presented in the appendix A.3.

6.4 Stenosis Model Results

In this chapter, we will present the results for two stenosis models: the two-daughter-vessel bifurcation with stenosis model and the three-daughter-vessel bifurcation with stenosis model. The first model contains one parent vessel ICA, which is connected to two daughter vessels MCA and ACA. One of the daughter vessels, MCA, is occluded, while the other daughter vessel ACA remains unoccluded. The second model inlcudes one parent vessel ICA, which is connected to three daughter vessels MCA, ACA and PComm. One of the daughter vessels, MCA, is occluded, while the daughter vessels ACA and PComm are not occluded. The inlet blood flow profile is specified at the start of the parent vessel ICA, and the three-element Windkessel outlet boundary condition is connected to the end of each daughter vessel. The parameters of ICA, MCA, ACA and PComm are extracted from CT contrast images using 3D Slicer, as shown in Table 4.1. The resistance and compliance of three-element Windkessel outlet boundary conditions for daughter vessels are listed in Table 5.1.

We will introduce stenosis proximal to the vessel junction. The turbulent loss and the inertial force loss are set to be $K_t = 1.52$ and $K_v = 1.2$, according to the experiment result [75,

94]. The viscous loss is represented as,

$$K_\nu = 16\frac{L_s}{r_p}\left(\frac{A_p}{A_s}\right)^2 \tag{6.6}$$

The occluded area is 25%, 50%, 75% and 90% of MCA cross-sectional areas. The length of the stenosis is set as 25% of the original vessel length. To compare the effect of stenosis on both upstream and downstream vessels, we also compare the results of the stenosis cases with the non-stenosis (control case) results. Therefore, this work studies how the severity of stenosis influences the blood flow and pressure waveform in both parent and daughter vessels.

In each simulation, the network starts at rest and the mean pressure reaches an oscillating steady- state condition after two cycles. The academic package MATLAB R2019b is used to run all simulations. The second-order accuracy finite difference method is used for time integration with a time step of 0.000016 s and a spatial step size of 0.1 cm for the three-daughter-vessel bifurcation with stenosis model. Doubling the number of spatial elements with a time step of of 0.000008 s reveals a maximum relative error less than 11% in the pressure waveform at the middle of MCA for the 75% MCA occlusion case.

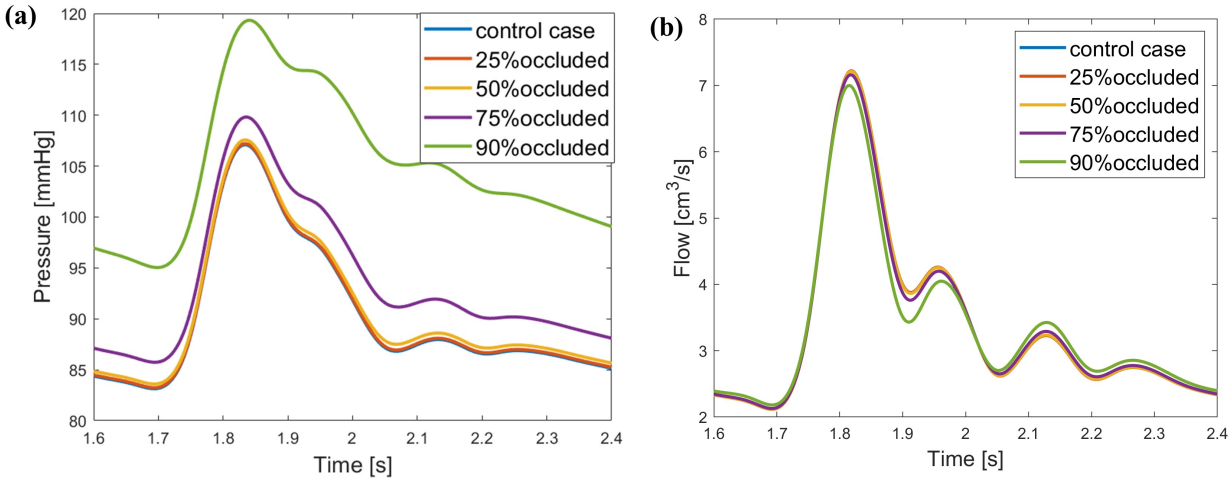

Figure 6.1 In two-daughter-vessel bifurcation with stenosis model, MCA is occluded by 0%, 25%, 50%, 75% and 90%: (a) ICA pressure profile at $x = 3$ cm; (b) ICA blood flow profile at $x = 3$ cm

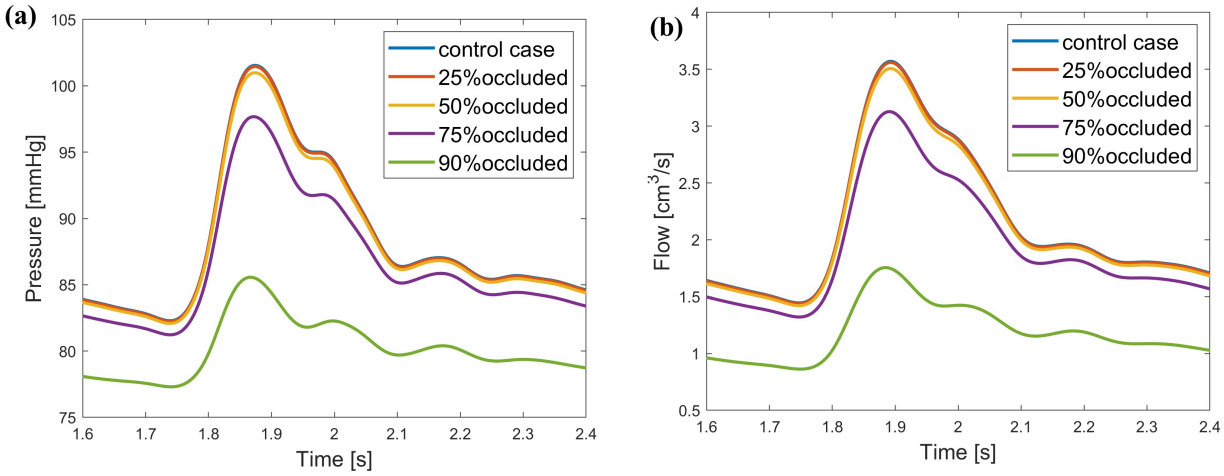

Figure 6.2 In two-daughter-vessel bifurcation with stenosis model, MCA is occluded by 0%, 25%, 50%, 75% and 90%: (a) MCA pressure profile at $x = 3$ cm; (b) MCA blood flow profile at $x = 3$ cm

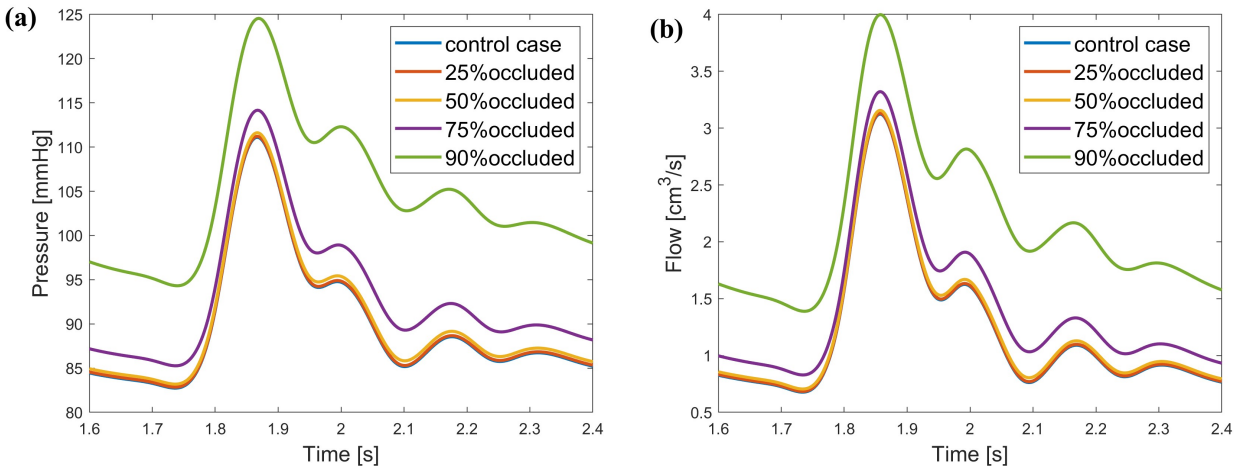

Figure 6.3 In two-daughter-vessel bifurcation with stenosis model, MCA is occluded by 0%, 25%, 50%, 75% and 90%: (a) ACA pressure profile at $x = 2$ cm; (b) ACA blood flow profile at $x = 2$ cm

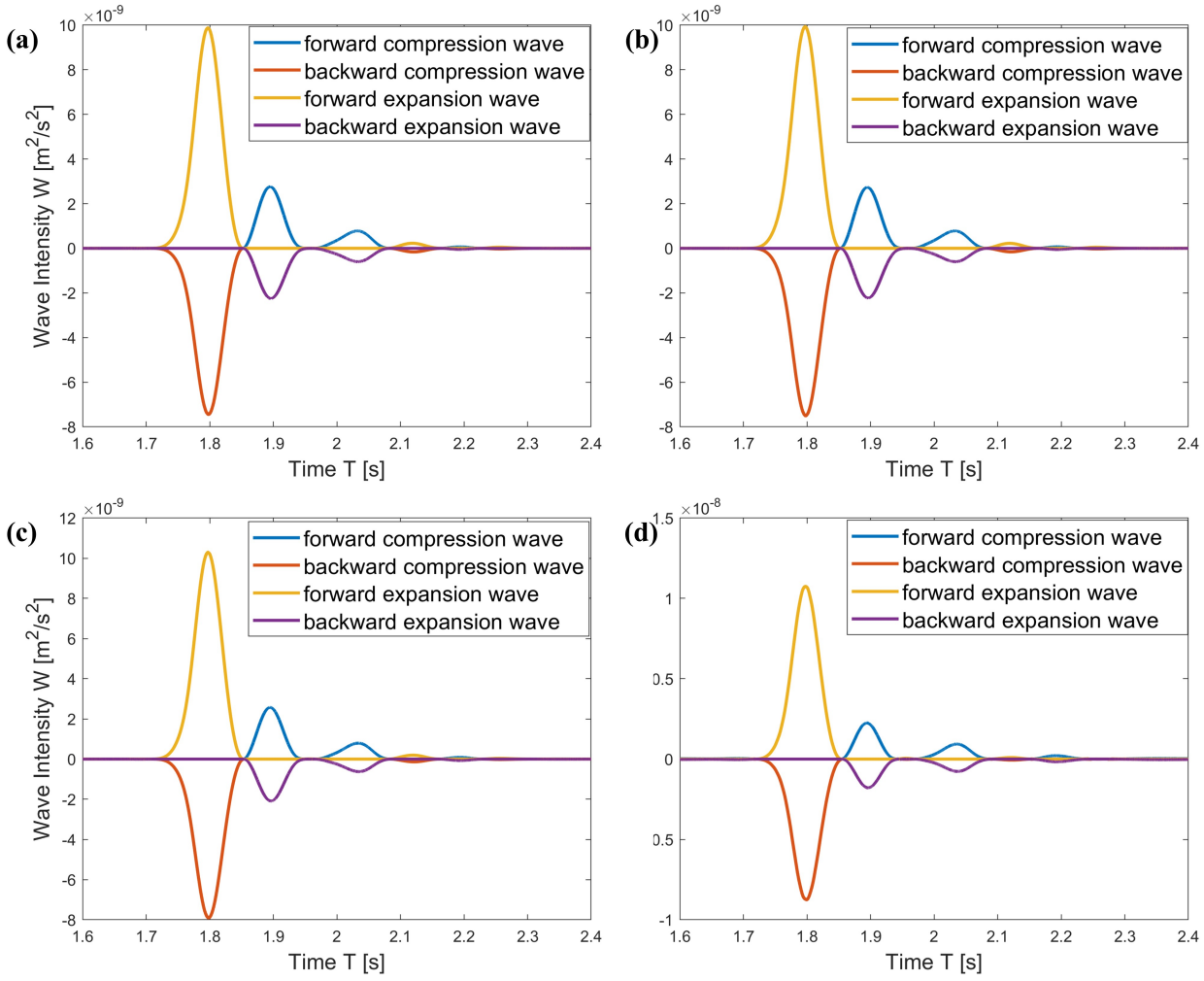

Figure 6.4 ICA WI in two-daughter-vessel bifurcation with stenosis model: (a) MCA is not occluded; (b) MCA is occluded by 50%; (c) MCA is occluded by 75%; (d) MCA is occluded by 90%

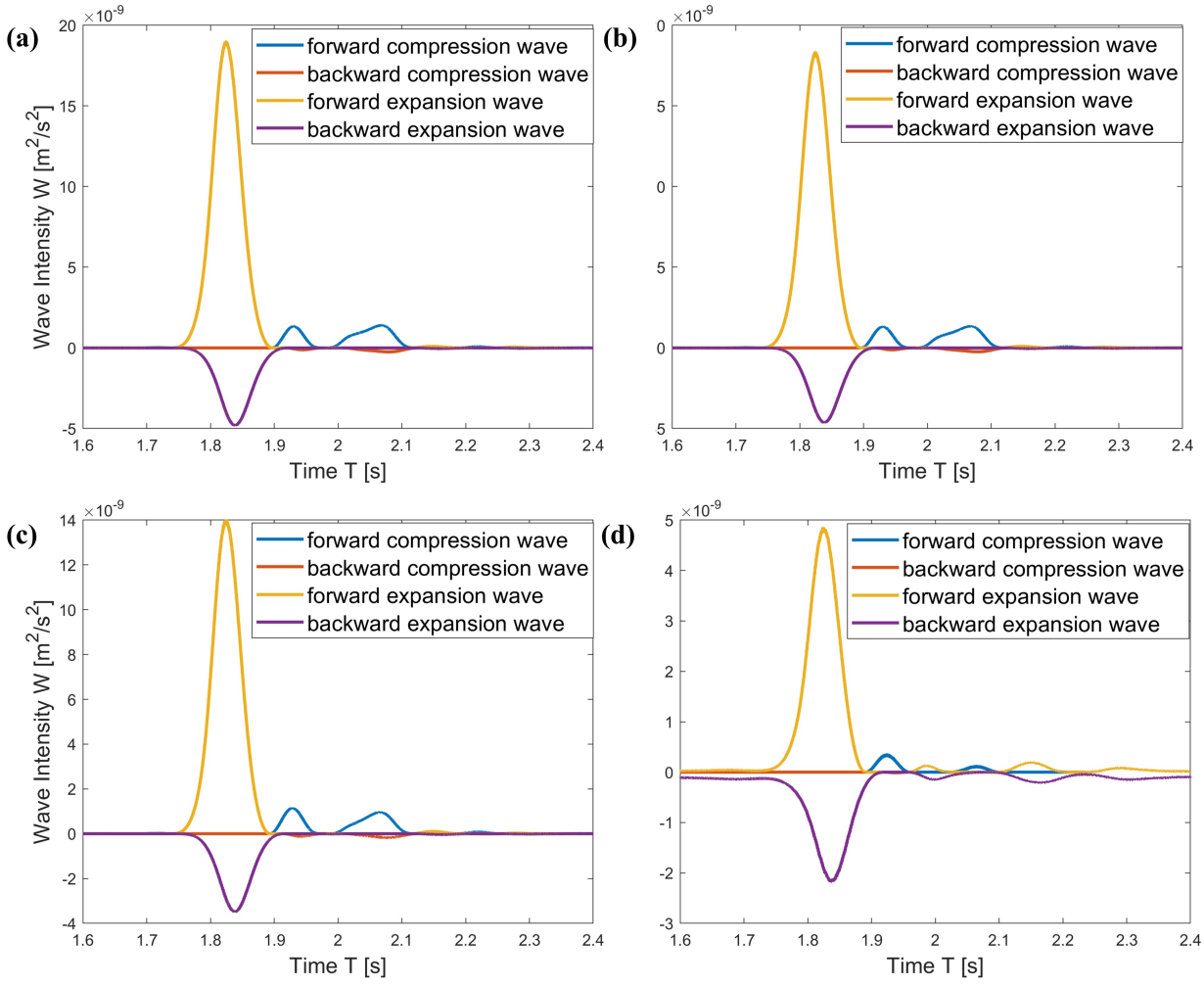

Figure 6.5 MCA WI in two-daughter-vessel bifurcation with stenosis model: (a) MCA is not occluded; (b) MCA is occluded by 50%; (c) MCA is occluded by 75%; (d) MCA is occluded by 90%

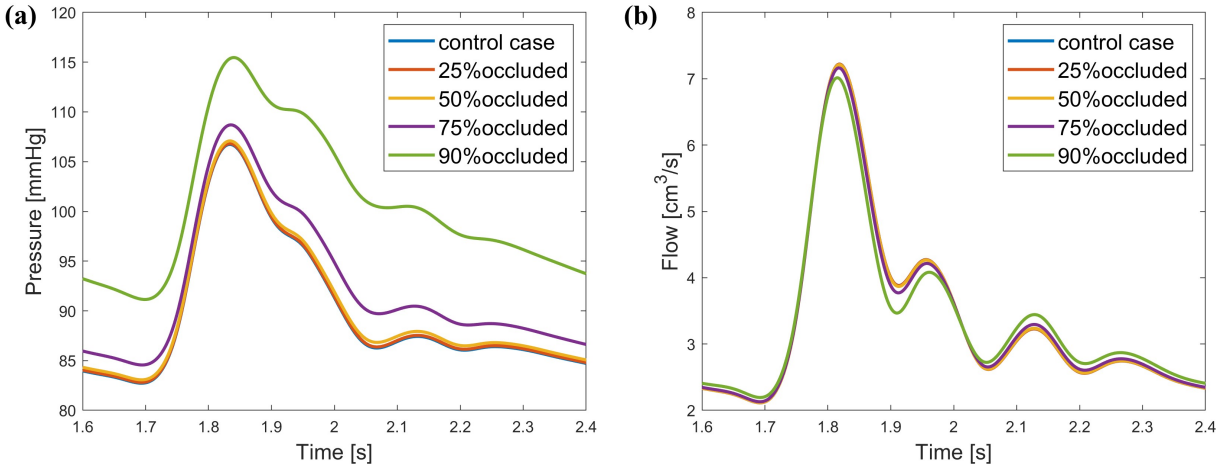

Figure 6.6 In three-daughter-vessel bifurcation with stenosis model, MCA is occluded by 0%, 25%, 50%, 75% and 90%: (a) ICA pressure profile at $x = 3$ cm; (b) ICA blood flow profile at $x = 3$ cm

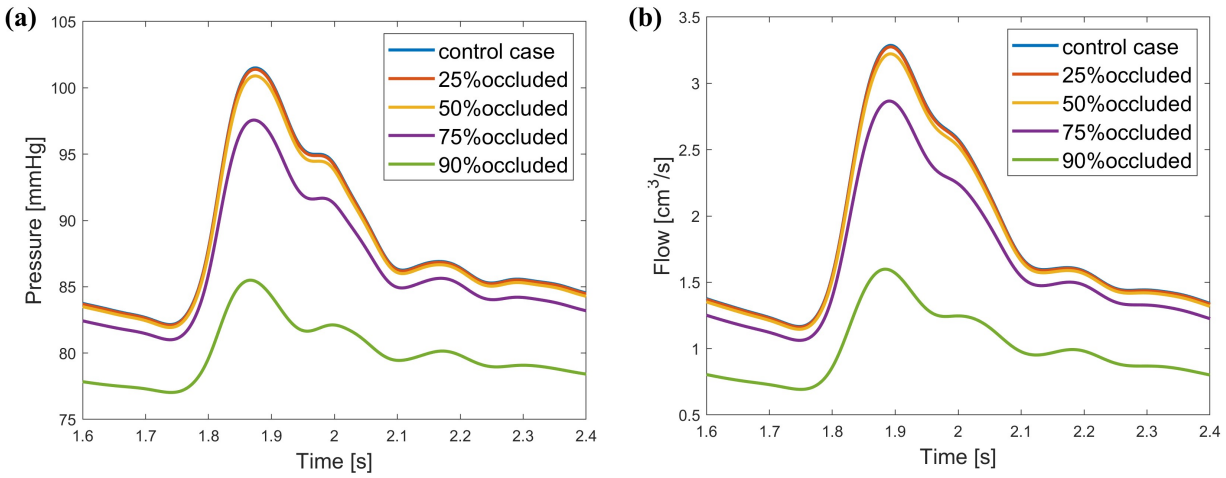

Figure 6.7 In three-daughter-vessel bifurcation with stenosis model, MCA is occluded by 0%, 25%, 50%, 75% and 90%: (a) MCA pressure profile at $x = 3$ cm; (b) MCA blood flow profile at $x = 3$ cm

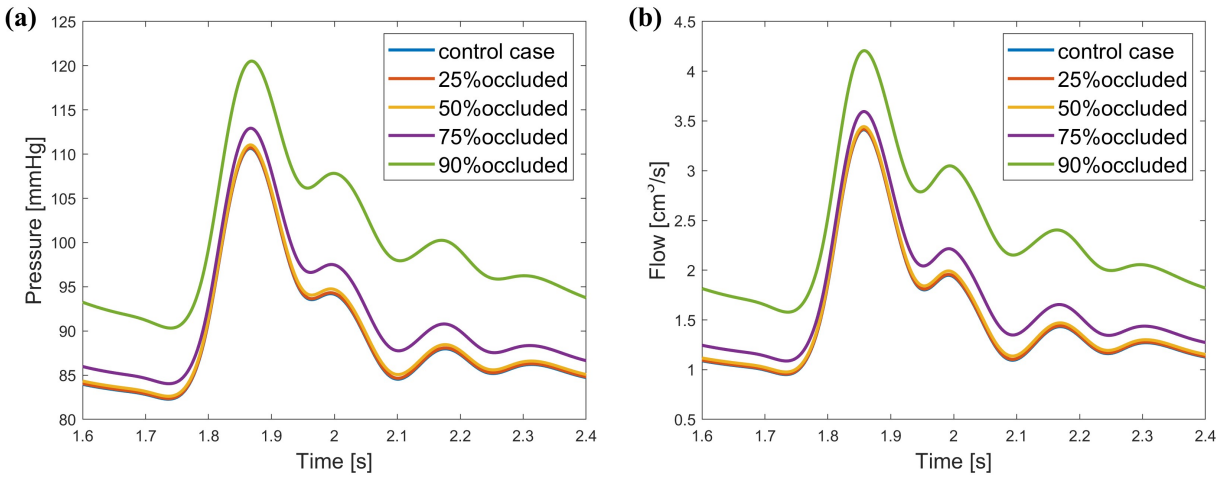

Figure 6.8 In three-daughter-vessel bifurcation with stenosis model, MCA is occluded by 0%, 25%, 50%, 75% and 90%: (a) ACA pressure profile at $x = 2$ cm; (b) ACA blood flow profile at $x = 2$ cm

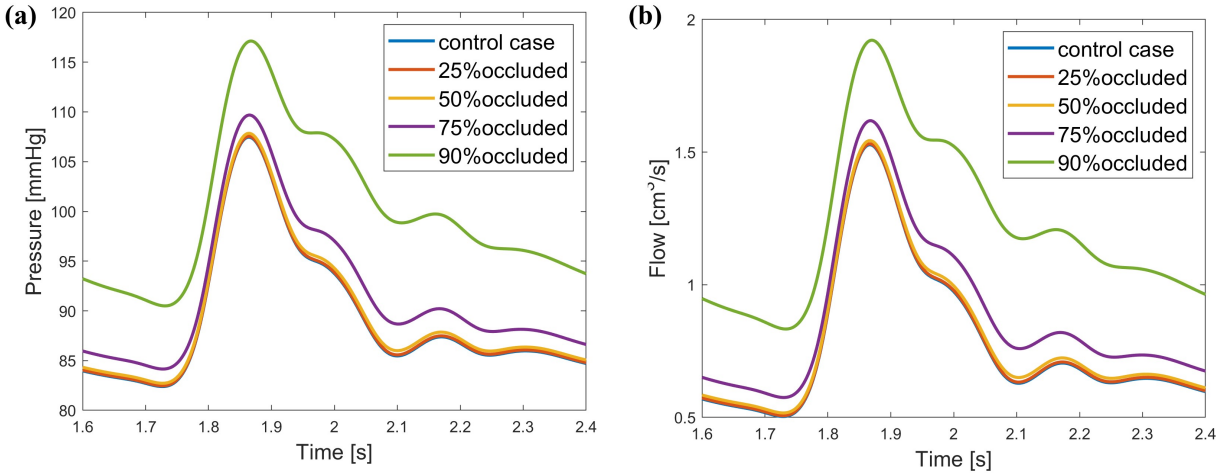

Figure 6.9 In three-daughter-vessel bifurcation with stenosis model, MCA is occluded by 0%, 25%, 50%, 75% and 90%: (a) PComm pressure profile at $x = 2$ cm; (b) PComm blood flow profile at $x = 2$ cm

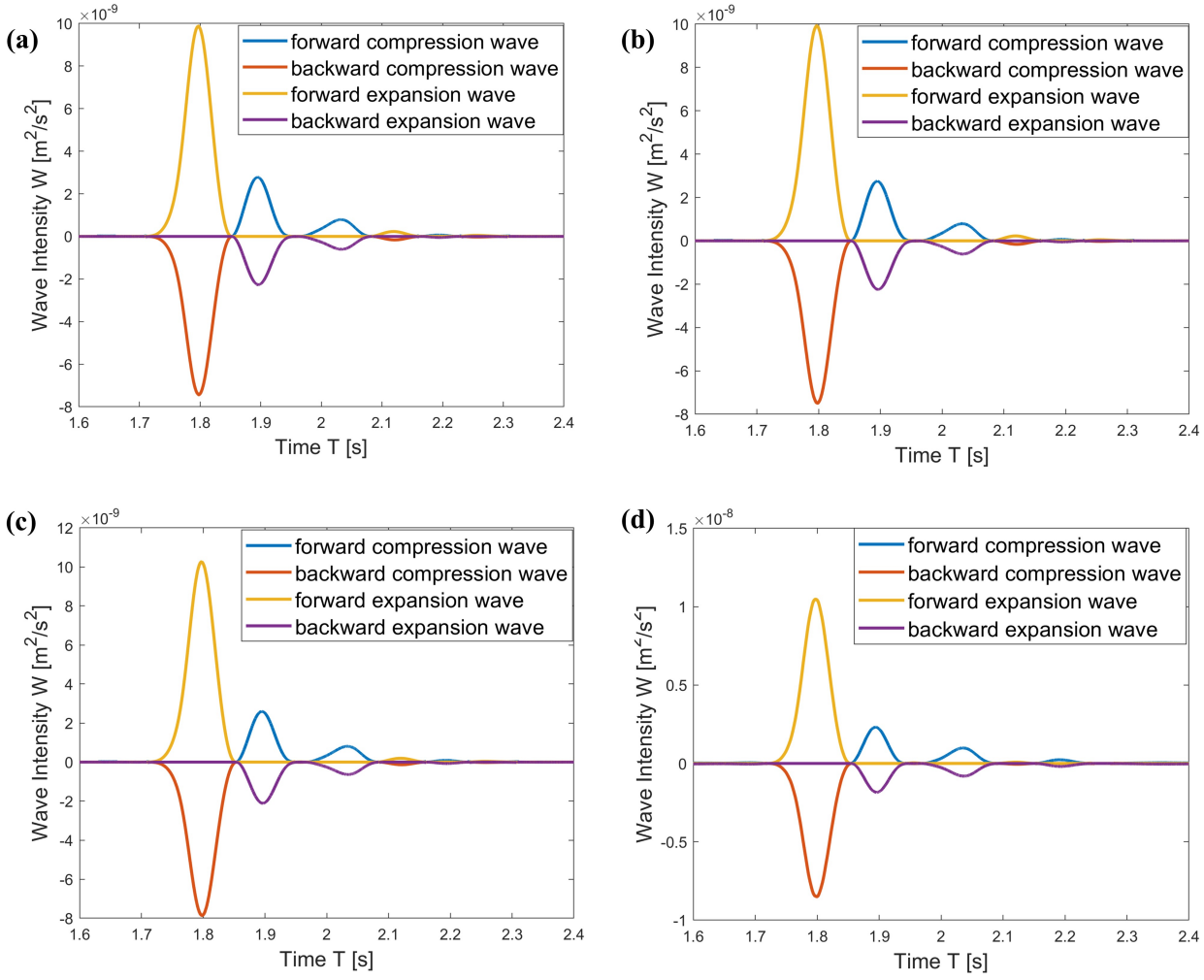

Figure 6.10 ICA WI in three-daughter-vessel bifurcation with stenosis model: (a) MCA is not occluded; (b) MCA is occluded by 50%; (c) MCA is occluded by 75%; (d) MCA is occluded by 90%

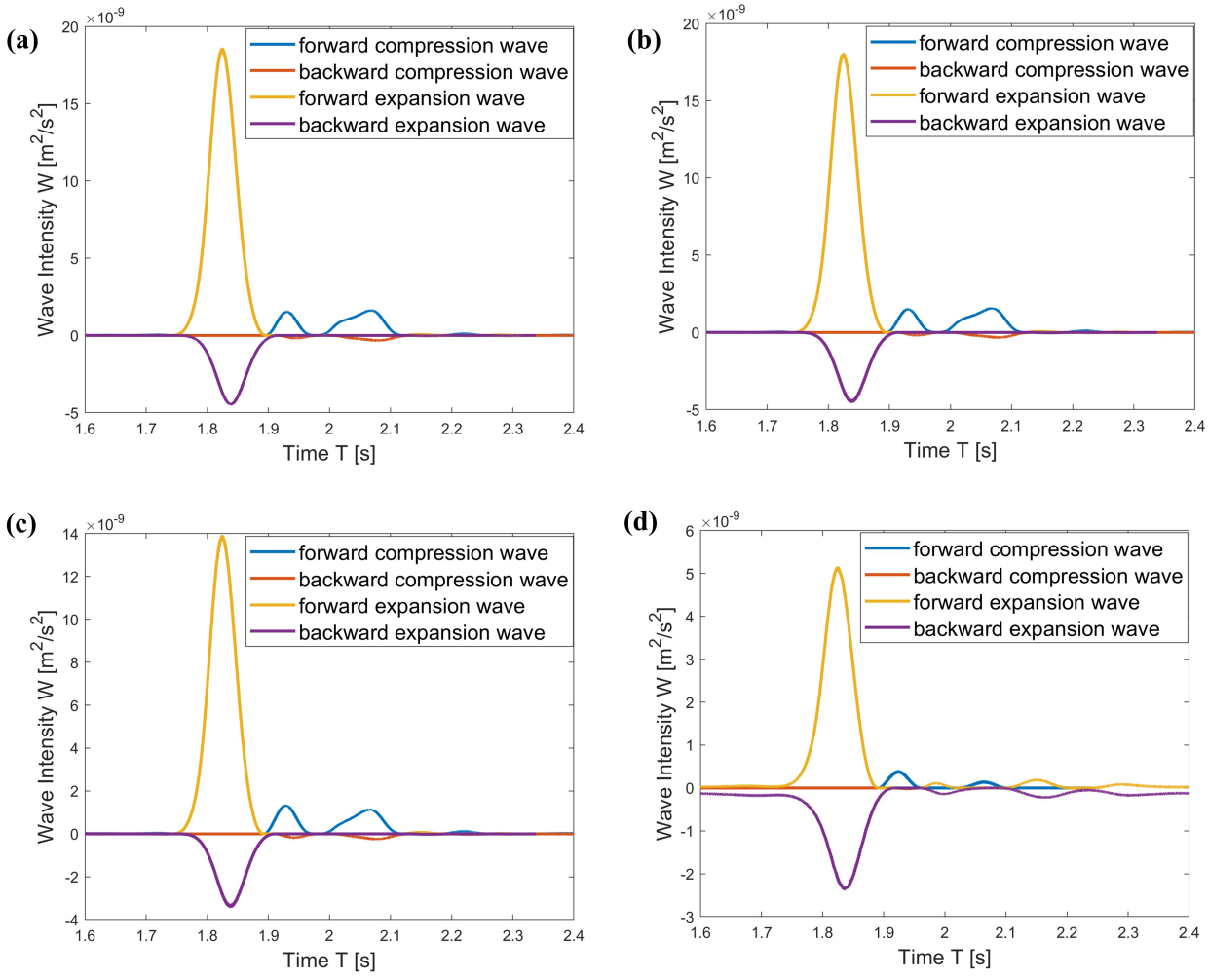

Figure 6.11 MCA WI in three-daughter-vessel bifurcation with stenosis model: (a) MCA is not occluded; (b) MCA is occluded by 50%; (c) MCA is occluded by 75%; (d) MCA is occluded by 90%

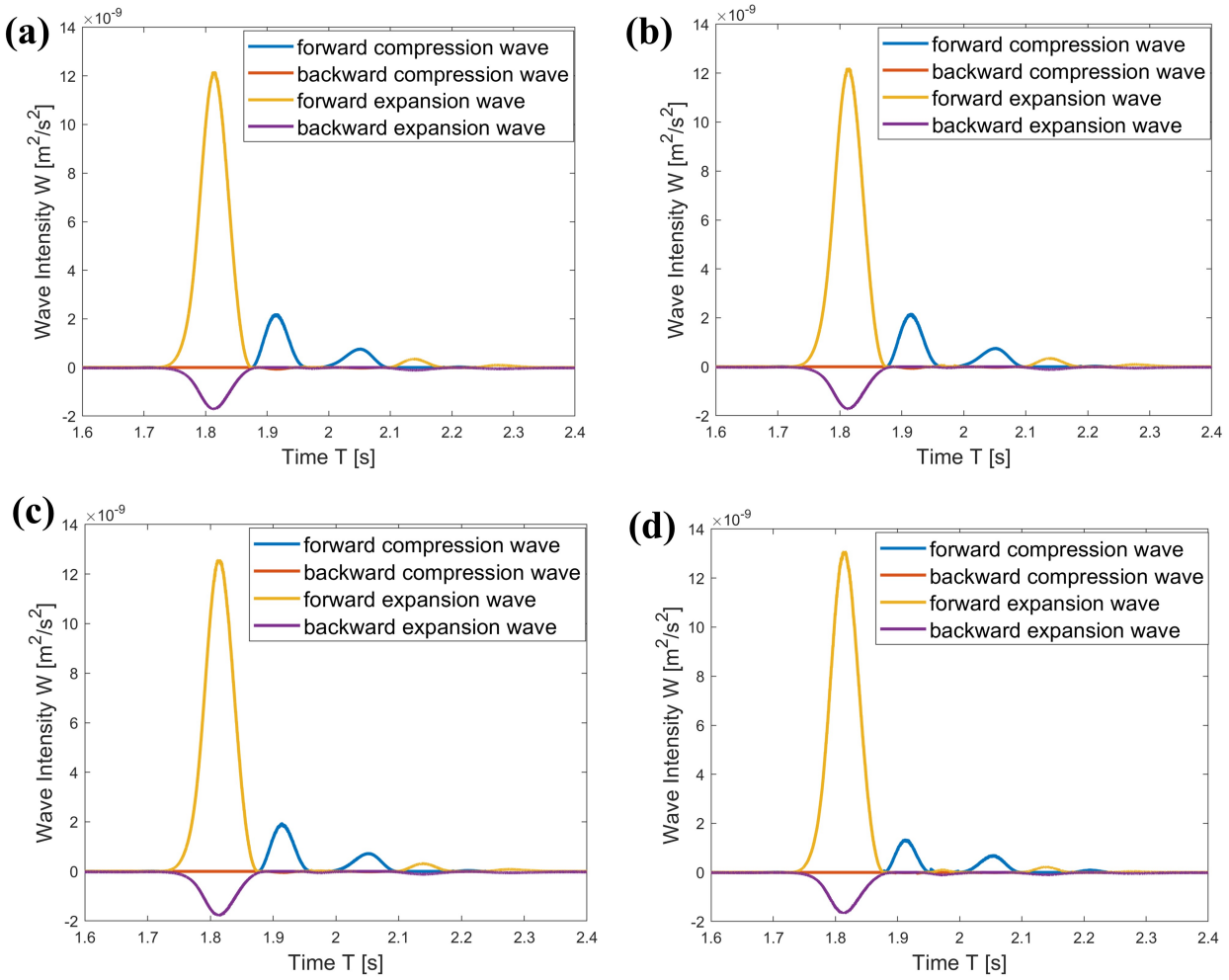

Figure 6.12 PComm WI in three-daughter-vessel bifurcation with stenosis model: (a) MCA is not occluded; (b) MCA is occluded by 50%; (c) MCA is occluded by 75%; (d) MCA is occluded by 90%

Figures 6.1 to 6.3 present the pressure and blood flow for ICA, MCA and ACA of the stenosis case with two-daughter-vessel bifurcation model. Figures 6.4 and 6.5 shows the separated forward and backward expansion and compression wave intensity of ICA and MCA of the same stenosis case, with varying degrees of MCA occlusion (0%,50%, 75% and 90%). Figures 6.6 to 6.9 show the pressure and blood flow for ICA, MCA, ACA and PComm of the stenosis case with three- daughter-vessel bifurcation model. Figures 6.10 to 6.12 present the separated forward and backward expansion and compression wave intensities of ICA, MCA and PComm of of the stenosis case when MCA is not occluded, is occluded by 50%, 75% and 90%. Figure 6.13 clearly shows the relationship between mean pressure of MCA and PComm with area reduction.

Figures 6.1(b) and 6.6(b) illustrate that the blood flow profile of the ICA exhibits a sharp systolic peak followed by a less pronounced secondary peak at the start of diastole, which matches the clinical measurement result [76]. Figures 6.2(a) and 6.7(a) demonstrate that the pressure profile of the MCA has a characteristic plateau midway in the descending part of the systolic peak, which is in accordance with the clinical measurement result [76].

It has been noticed from Figures 6.1 to 6.3 and Figures 6.6 to 6.9 that the pressure profile increases as the severity of stenosis increases. Furthermore, it can be observed that the effect of mild stenosis (less than 50% cross-sectional area is obstructed) on pressure waveform can be negligible. The effect of stenosis becomes more significant on the pressure profile only after about 75% cross-sectional area is obstructed. Additionally, the presence of stenosis not only affects the peak value of the flow profile in the daughter vessel but also causes a phase shift in the pressure and blood flow waveform.

Figures 6.1 and 6.6 present the ICA pressure and blood flow profiles when $0 \sim 90\%$ cross-sectional area of MCA is obstructed. The pressure profile significantly increases when 75% and 90% cross-sectional area is obstructed compared to the control case. It is shown in Figures 6.1(b) and 6.6(b) that the severity of stenosis of MCA has little effect on the blood

flow waveform of the ICA. Figures 6.2 and 6.7 present the MCA pressure and blood flow profiles when $0 \sim 90\%$ cross-sectional area of MCA is obstructed. It is evident that both the pressure and blood flow significantly decrease when 75% and 90% cross-sectional area is obstructed compared to the control case. This outcome is expected, as the narrowed MCA restricts blood flow passage through the vessel. Notably, a phase change is observed in Figures 6.2 and 6.7, and the magnitude of this phase change increases as the severity of stenosis increases.

Figure 6.3 and 6.8 present the ACA pressure and blood flow profiles when $0 \sim 90\%$ cross-sectional area of MCA is obstructed. Both the pressure and blood flow exhibit a significant increase when 75% and 90% of the MCA cross-sectional area is obstructed, in contrast to the control case. The pronounced phase change appears between the control case and 90% cross-sectional area obstructed case in ACA pressure profile shown in Figures 6.3(a) and 6.8(a). Figure 6.9 presents the PComm pressure and blood flow profile when $0 \sim 90\%$ cross-sectional area of MCA is obstructed. Both the pressure and the blood flow profile significantly increase when 75% and 90% of the MCA cross-sectional area is obstructed, compared to the control case. The redistribution of blood flow to the unobstructed vessels ACA and PComm through downstream vascular netwrok, leads to the increased pressure and blood in the PComm.

Wave Intensity analysis results are presented in Figures 6.4, 6.5 and 6.10 to 6.12. In this study, the forward and backward wave intensities are further separated into four components: forward compression wave (FCW), forward extension wave (FEW), backward compression wave (BCW) and backward extension wave (BEW). This separation allows for a better understanding of the impact of ventricular or peripheral resistance on the wave intensity.

Figures 6.4(a) and 6.10(a) demonstrate the parent vessel (ICA) wave intensity waveform in the control case. The dominant separated wave component is the FEW, followed by a minor BCW that corresponds to the reflection of the initial contraction. Figures 6.4(b) and 6.10(b) show the ICA wave intensity waveform when the cross-sectional area of MCA is occluded

by 50%, while Figures 6.4(c,d) and6.10(c,d) show the ICA wave intensity waveform for 75% and 90% occlusion, respectively. The stenosis has little effect on the shape of wave intensity waveform, but it slightly increases the amplitude of FEW and decreases the amplitude of BCW. In the 90% occluded case, the third peak of the FCW becomes more pronounced, while the second peak of FEW nearly disappears.

Figures 6.5(a) and 6.11(a) demonstrate the wave intensity waveform of the daughter vessel (MCA) in the control case. The predominant FEW arises first followed by the minor BEW. The pronounced phase lag is noticed between forward expansion and backward expansion waves. Overall, the compression wave is negligible in this case. Figures 6.5(b), (c), (d) and 6.11(b), (c), (d) demonstrate the MCA wave intensity waveform for 50%,75% and 90% occlusion, respectively. The stenosis has more striking effect on the wave intensity compared to the parent vessel (ICA). In the occluded cases, MCA FEW and BCW significantly decrease compared to the control case. Some interesting phenomenon is observed in the 90% occluded case, where the first and second peaks of FCW decrease while the BEW increase.

Figure 6.12(a) shows the wave intensity waveform of the PComm in the control case. The FEW is raised first, followed by the BEW. A noticeable phase lag between the FEW and BEW can be observed, which is more pronounced compared to the parent vessel ICA. In the 90% obstructed case, there is a slight increase in the amplitude of the first peak of the FEW compared to the control case.

6.5 Reverse Flow Investigation

As discussed in Chapter 1.2.2, normal blood flow is piped from proximal large arteries to distal small arteries due to the high blood pressure difference between the ventricle and the peripheral resistance to flow. In collateral circulation, blood flow is allowed to move from distal small arteries to large cerebral arteries when occlusions occur. Our results indicate that the obstructed and unobstructed pathways are highly affected by stenosis, as discussed in Chapter 6.4. In this chapter, we will further investigate the occurrence of reverse flow that existed in MCA when it is extensively occluded. What's more, we will explore the compensatory function of PComm in collateral circulation.

In Figures 6.2 and 6.7, the results clearly show significant pressure drops downstream from the lesion (MCA pressure drops), while the resistance to flow increases. On the other hand, in the unobstructed pathways (Figures 6.3, 6.8 and 6.9), both blood flow and pressure increase. The increase in pressure and flow may facilitate the redirection of blood flow from PComm to MCA through the small vascular network. Our findings support these hypotheses and demonstrate the existence of collateral blood flow in the obstructed pathway [5].

Several studies applied wave intensity analysis in investigate cerebrovascular artery function [100, 101]. Results in Figure 6.8 reveal a large FEW in MCA during systole followed by a smaller magnitude BEW and FCW, which rapidly decay during diastole. Additionally, we observe that FEW increases while FCW decreases during the systole. The FEW, originating from the microcirculatory end, accelerates the blood flow and increases the pressure, while the FCW, also originating from the microcirculatory end, decelerates the blood flow and decreases the pressure [100]. The FCW decreases during systole due to the presence of MCA stenosis. In contrast, the FEW increases during systole, accelerating the blood flow and pressure from the downstream vascular network. This scenario becomes more obvious in the case of 75% and 90% occluded MCA. However, the same scenario is not observed in ICA

and PComm. Our wave intensity results further support the hypothesis that the reverse flow does exist in MCA when MCA is occluded.

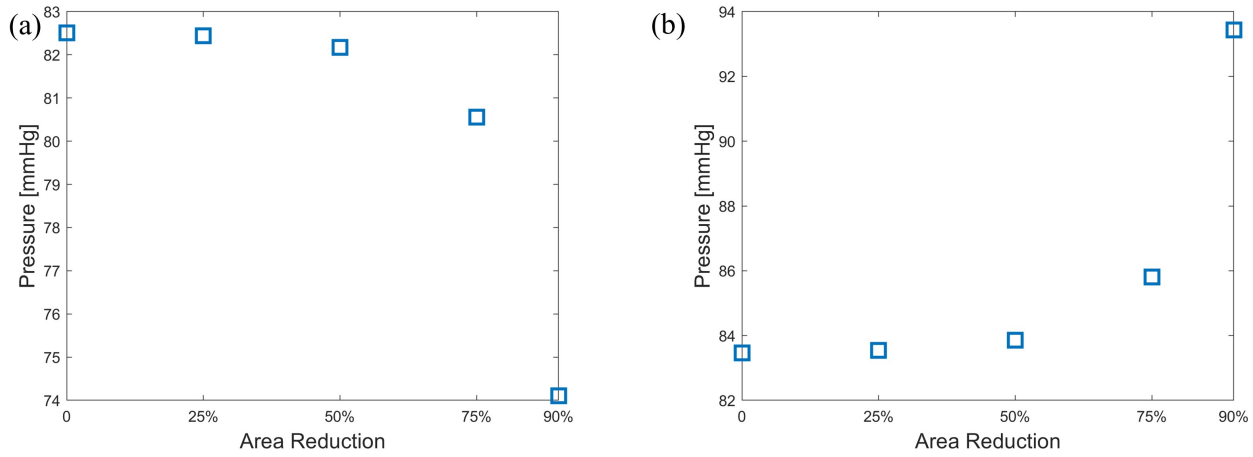

Figure 6.13 Area reduction vesus mean pressure: (a) MCA; (b) PComm

6.6 Sensitivity Analysis of Three-Daughter-Vessel Bifurcation with Stenosis Model

In Chapter 3.6, we conducted a parameter variation study on outlet boundary conditions, specifically focusing on resistance and compliance. The results of the sensitivity analysis revealed a strong correlation between the compliance and the phase shift observed in the upstream pressure waveform, while resistance exhibited a significant influence on the amplitude of the upstream pressure waveform. In this chapter, our aim is to investigate the effects of varing compliance parameters on the upstream pressure and flow waveforms within the three-daughter-vessel bifurcation with stenosis model. This sensitivity analysis serves as a valuable tool to further validate the key conclusions presented in Chapter 6.4.

The compliance in the three-daughter-vessel bifurcation with stenosis model is initially configured at the scale of $1e^{-5}$. To investigate the changes in the upstream pressure and flow waveforms resulting from compliance variations, we increases and decreases the compliance by 20% from its original value. The sensitivity analysis is perfomed in three cases: the control case, the 50% cross-sectional area occluded stenosis case and the 75% cross-sectional area occluded stenosis case. Figure 6.14 illustrates the changes in ICA pressure and flow waveforms for these cases when compliance is modified by 20% from its original value. In a similar manner, Figure 6.15 demonstrates the variations in MCA pressure and flow waveforms, while Figure 6.16 presents the variations in ACA pressure and flow waveforms. These three figures offer insights into how the compliance adjustment impacts the upstream pressure and flow waveforms across different scenarios.

Figure 6.14 reveals that, as the severity of stenosis increased, there is a slight elevation in ICA pressure, while the ICA flow waveform remains largely consistent. These findings align with the conclusions drawn in Chapter 6.4 regarding compliance variations. Although variations in compliance does introduce subtle changes in the ICA pressure waveform, these

differences are relatively minor. For ICA flow waveform, we observe that slight discrepancies in amplitude when we manipulate compliance. What's more, the feature of the ICA flow is characterized by a sharp peak followed by a less pronounced second peak, and it remains consistent across these compliance adjustments. In Figure 6.15, it becomes evident that MCA pressure significantly decreases with increasing stenosis severity. This conclusion is also applicable to the MCA flow waveform. Interestingly, the MCA pressure and flow waveforms exhibit only marginal variations when the compliance is increased or decreased by 20%. Furthermore, the characteristic plateau in the middle of MCA pressure waveform persists consistently, irrespective of compliance adjustments. In Figure 6.16, the ACA pressure and flow waveforms display a tendency to increase with greater stenosis severity. Notably, variations in compliance introduce only minor discrepancies across the control case, the 50% cross-sectional area occluded case and the 75% cross-sectional area occluded case.

In summary, we conducted compliance variations, adjusting this outlet boundary condition parameter by 20% from its original value. Throughout this investigation, we closely examined the resulting pressure and flow waveforms in the ICA, MCA, and ACA. Our observations revealed that while compliance variations did induce slight discrepancies in both pressure and flow waveforms, these differences remained notably small and did not exert a significant influence on our overall conclusions. Moreover, it's worth highlighting that the distinctive characteristics of the ICA flow and MCA pressure waveforms remained consistent throughout the compliance adjustments, reaffirming the robustness of our findings.

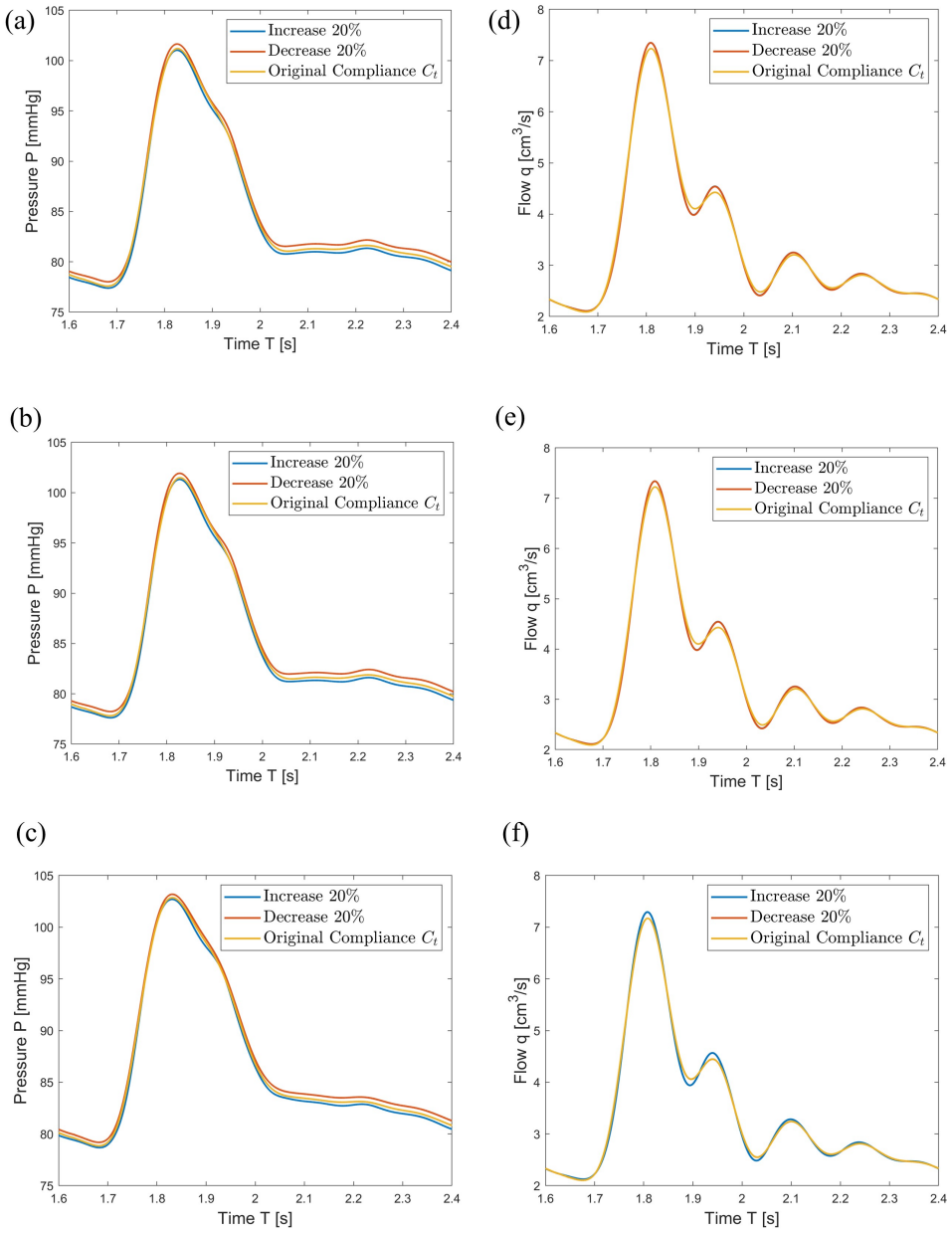

Figure 6.14 ICA pressure and flow waveform results under varied compliance condition: (a) pressure waveform for control case; (b) pressure waveform for 50% cross-sectional area occluded case; (c) pressure waveform for 75% cross-sectional area occluded case; (d) flow waveform for control case; (e) flow waveform for 50% cross-sectional area occluded case; (f) flow waveform for 75% cross-sectional area occluded case

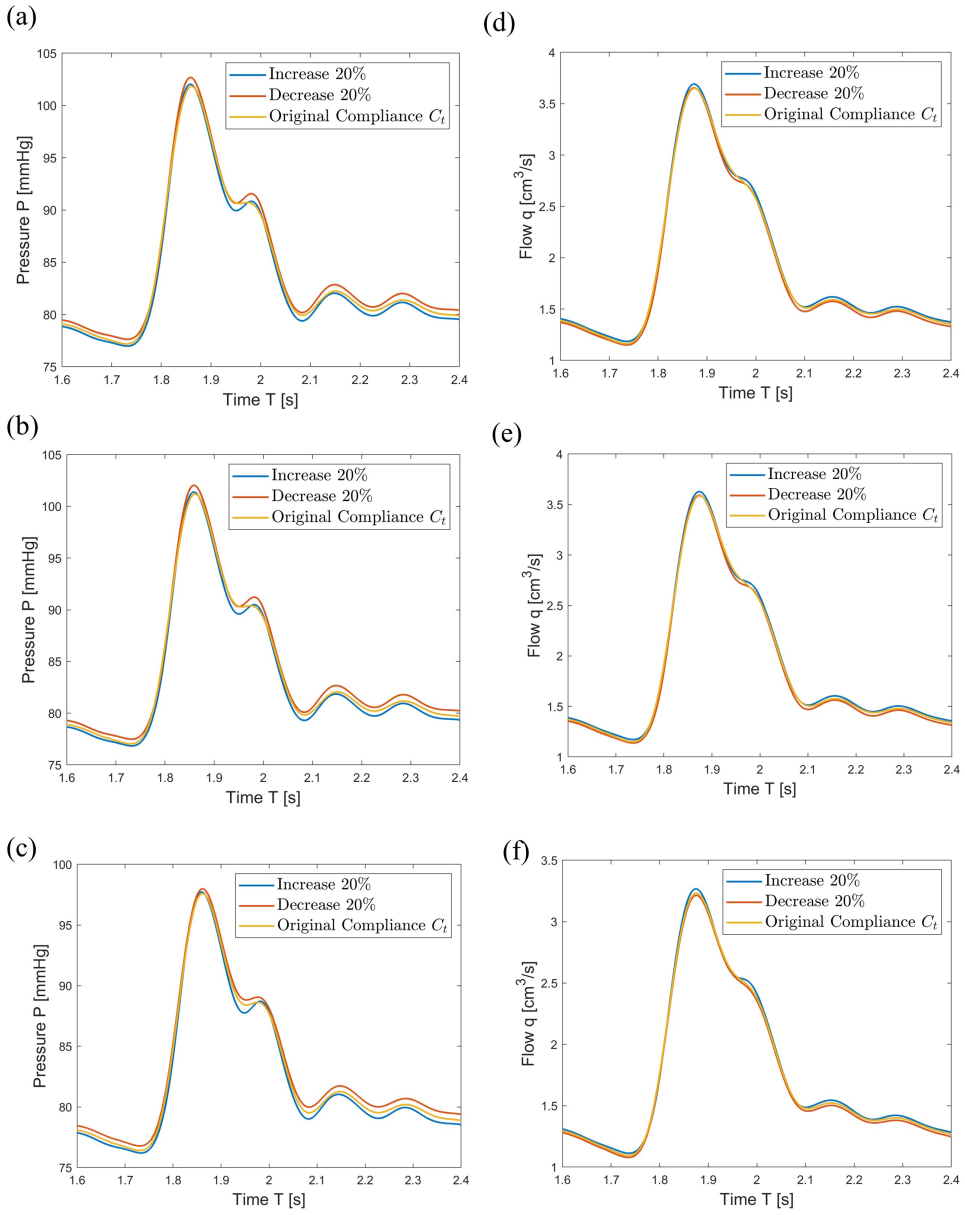

Figure 6.15 MCA pressure and flow waveform results under varied compliance condition: (a) pressure waveform for control case; (b) pressure waveform for 50% cross-sectional area occluded case; (c) pressure waveform for 75% cross-sectional area occluded case; (d) flow waveform for control case; (e) flow waveform for 50% cross-sectional area occluded case; (f) flow waveform for 75% cross-sectional area occluded case

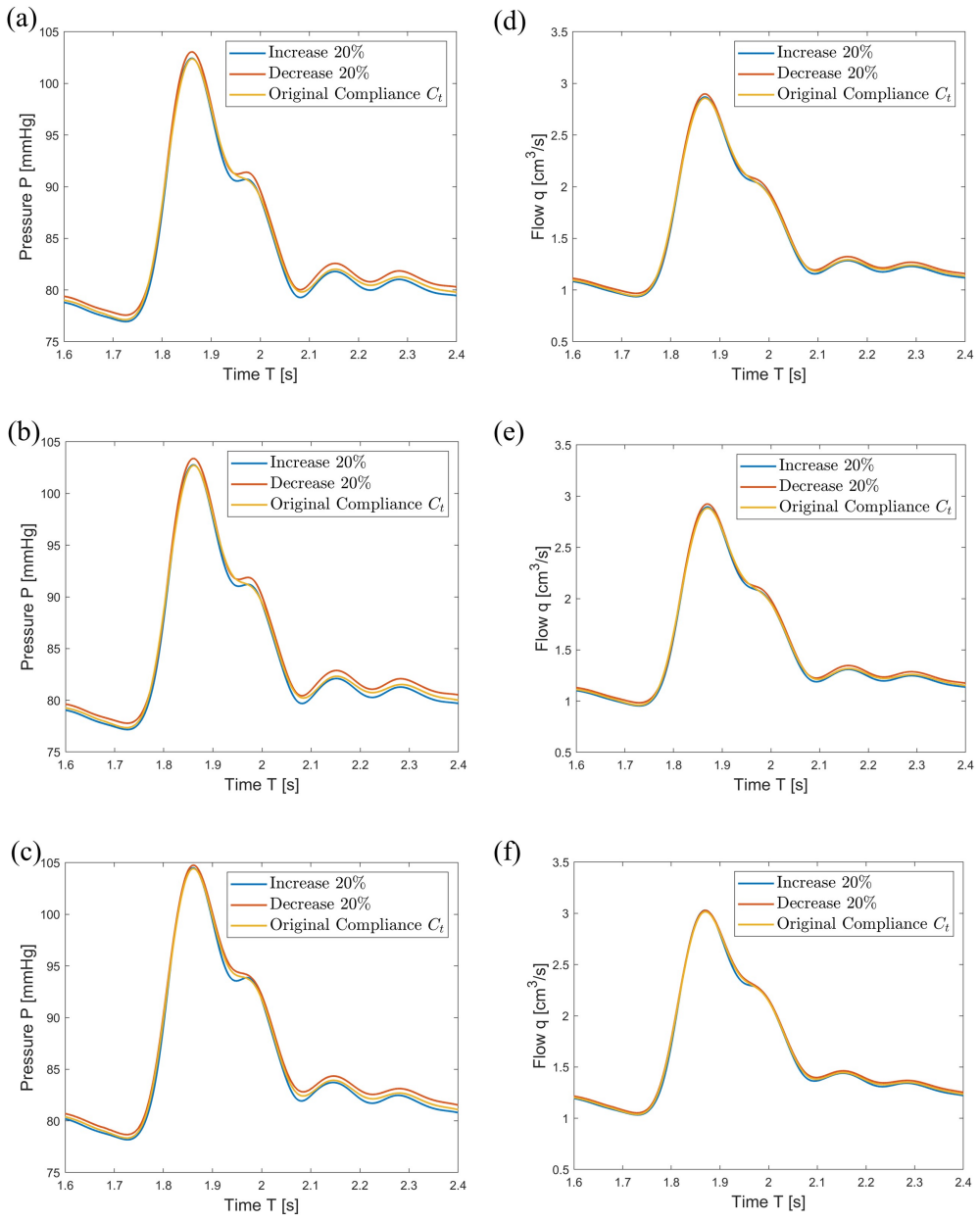

Figure 6.16 ACA pressure and flow waveform results under varied compliance condition: (a) pressure waveform for control case; (b) pressure waveform for 50% cross-sectional area occluded case; (c) pressure waveform for 75% cross-sectional area occluded case; (d) flow waveform for control case; (e) flow waveform for 50% cross-sectional area occluded case; (f) flow waveform for 75% cross-sectional area occluded case

Chapter Seven

Conclusions

Intracranial stenosis contributes to a significant portion, ranging from 30% to 50%, of ischemic strokes, which rank among the primary causes of mortality in the United States. Collateral circulation becomes crucial in cases of severe intracranial stenosis where more than 90% of the cross-sectional area is occluded, playing a pivotal role in determining whether a stroke patient can recover from an ischemic event. However, the factors underlying the development of collateral circulation remain unclear and are challenging to observe solely from image data. This work develops a computational model that integrates patient-specific CTA imaging with arterial segments fluid dynamics to investigate the intracranial stenosis and collateral circulations in CoWs.

The model includes parent arterial segment, ICA, and daughter arterial segments, MCA, ACA and PComm, that are all extracted from individual CTA scans. Inlet blood flow profile is calibrated using color-coded duplex ultrasound from young, healthy volunteers. A three-element Windkessel outlet boundary condition is attached to the end of each daughter arterial segment. Bifurcation conditions and stenosis are also included in the model, varying the area reduction of MCA from 0% $\sim$ 90% to predict the development of collateral circulations and their effect on the daughter vessel PComm.

The results show that increases in area reduction increase the pressure of the unobstructed pathway and decrease the pressure of the obstructed pathway, which becomes significant after 90% of the MCA area is occluded, aligning with clinical observations. Our WIA results

indicate that the FEW of the obstructed pathway increases when area reduction increases (90% MCA occluded scenario). WIA results also suggest that the downstream vascular network pressure and blood flow increase as the area reduction of obstructed pathway increases. The pressure/blood flow and WIA results demonstrate that when MCA is largely occluded, collateral circulation forms between PComm and MCA through the downstream vascular network.

Furthermore, we conduct a comparison of the three-element Windkessel outlet boundary condition and the 1-D binary tree outlet boundary condition. The pressure and blood flow waveform results of the upstream large artery show that the 1-D binary tree outlet boundary condition has little difference with the three-element Windkessel outlet boundary condition, when the resistance parameter of the 0-D outlet boundary condition is fitted to match the impedance of the 1-D outlet boundary condition. Additionally, while the 1-D binary tree outlet boundary conditions encompass blood flow and pressure information of the downstream vascular network, the long-wave propagation assumption imposes a restriction that the upstream large artery must be long enough, which is not suitable for our model.

The computational model developed in this work offers valuable insights into the development of stenosis and the formation of collateral circulation. Though we have access to abundant imaging data nowadays, it is challenging to observe the dynamic progression of stenosis solely from the medical imaging data. As the imaging data is just a snapshot of the stenosis, we have a poor understanding of how stenosis evolves over time. Gaining insight into how stenosis evolves over time is crucial. Our computational framework, which incorporates downstream vascular network reflection waveforms, helps shed light on this process.

Moreover, the versatility of our framework allows it to be applied to various arterial segments and different inflow and outflow boundary conditions, making it highly applicable in surgical planning and medical device design. It can be employed to investigate different types of M1

stenosis, intracranial and extracranial stenosis, and can adapt to different anatomies. The computational model serves as a standard protocol that can be utilized under different conditions, making it a valuable tool in the investigation of numerous cerebral vascular diseases and providing essential guidance for clinical surgical planning.

In this work, one patient anatomy is applied to the computational model. However, to ensure its robustness and applicability, future validation will be conducted using multiple patient anatomies. Additionally, the 1-D computational model relies on certain simplifications and assumptions, which may limit its realism. To overcome this, a more comprehensive 2-D computational model will be proposed in future studies, offering a more detailed representation of blood flow development and reverse flow changes. The calibration of the inlet blood flow boundary condition from healthy volunteers, while useful for initial exploration, may not fully reflect real-world scenarios. To address this limitation, we aim to develop a method to extract the inlet blood flow from CT perfusion images from our patient database, enabling us to provide more realistic and personalized guidance for surgical planning.

Overall, our work presents a novel and realistic computational model that integrates patient-specific data, enabling a deeper understanding of the evolution of hemodynamic changes in cerebral arterial segments. The framework is also used to obseve the dynamic progression of stenosis changes and their relationship with the formation of collateral circulation.

APPENDIX

Appendix A

Solution Process

A.1 Iteration Method Solving Three Daughter Vessel Bifurcation Model

The governing equation at bifurcation provides 24 equations and 24 unknowns.

$x_1 = (q^p)_M^{n+1}$ $x_2 = (q^p)_M^{n+1/2}$ $x_3 = (q^p)_{M+1/2}^{n+1/2}$

$x_4 = (q^{d_1})_0^{n+1}$ $x_5 = (q^{d_1})_0^{n+1/2}$ $x_6 = (q^{d_1})_{-1/2}^{n+1/2}$

$x_7 = (q^{d_2})_0^{n+1}$ $x_8 = (q^{d_2})_0^{n+1/2}$ $x_9 = (q^{d_2})_{-1/2}^{n+1/2}$

$x_{10} = (A^p)_M^{n+1}$ $x_{11} = (A^p)_M^{n+1/2}$ $x_{12} = (A^p)_{M+1/2}^{n+1/2}$

$x_{13} = (A^{d_1})_0^{n+1}$ $x_{14} = (A^{d_1})_0^{n+1/2}$ $x_{15} = (A^{d_1})_{-1/2}^{n+1/2}$

$x_{16} = (A^{d_2})_0^{n+1}$ $x_{17} = (A^{d_2})_0^{n+1/2}$ $x_{18} = (A^{d_2})_{-1/2}^{n+1/2}$

$x_{19} = (q^{d_3})_0^{n+1}$ $x_{20} = (q^{d_3})_0^{n+1/2}$ $x_{21} = (q^{d_3})_{-1/2}^{n+1/2}$

$x_{22} = (A^{d_3})_0^{n+1}$ $x_{23} = (A^{d_3})_0^{n+1/2}$ $x_{24} = (A^{d_3})_{-1/2}^{n+1/2}$

$$f_1 : -x_1 + (q_P)_M^n - \frac{\Delta t}{\Delta x}(\frac{x_3^2}{x_{12}} + B(M+1/2, x_{12}) - (R_2)_{M-1/2}^{n+1/2}) + \frac{\Delta t}{2}(F(M+1/2, x_3, x_{12}) + \frac{dB(M+1/2,x_{12})}{dx} + (S_2)_{M-1/2}^{n+1/2})$$

$$f_{2,3,19} : -x_{4,7,19} + (q_{d_1,d_2,d_3})_0^n - \frac{\Delta t}{\Delta x}((R_2^{d_1,d_2,d_3})_{M+1/2}^{n+1/2} - B(-1/2, x_{15,18,24}) - \frac{x_{6,9,21}^2}{x_{15,18,24}}) + \frac{\Delta t}{2}(S_2^{d_1,d_2,d_3})_{1/2}^{n+1/2} + F(-1/2, x_{6,9,21}, x_{15,18,24}) + \frac{dB(-1/2,x_{15,18,24}}{dx})$$

$$f_4 : -x_{10} + (A^P)_M^n - \frac{\Delta t}{\Delta x}(-x_3 - (q^P)_{M-1/2}^{n+1/2})$$

$$f_{5,6,20} : -x_{13,16,22} + (A_{d_1,d_2,d_3})_0^n - \frac{\Delta t}{\Delta x}(-x_{6,9,21} + (q_{d_1,d_2,d_3})_{M+1/2}^{n+1/2})$$

$f_7 : -x_2 + \frac{1}{2}(x_3 + (q_P)_{M-1/2}^{n+1/2})$

$f_{8,9,21} : -x_{5,8,20} + \frac{1}{2}(x_{6,9,21} + (q_{d_1,d_2,d_3})_{1/2}^{n+1/2})$

$f_{10} : -x_{11} + \frac{1}{2}(x_{12} + (A_P)_{M-1/2}^{n+1/2})$

$f_{11,12,22} : -x_{14,17,23} + \frac{1}{2}(x_{15,18,24} + (A_{d_1,d_2,d_3})_{M+1/2}^{n+1/2})$

$f_{13,14} : -x_{2,1} + x_{5,4} + x_{8,7} + x_{20,19}$

$f_{15,16,23} : -(f_P)_M^{n+1/2}(1 - \sqrt{\frac{(A_0^P)_M^{n+1/2}}{x_{11}}}) + (f_{d_1,d_2,d_3})_0^{n+1/2}(1 - \sqrt{\frac{(A_0^{d_1,d_2,d_3})_0^{n+1/2}}{x_{14,17,23}}})$

$f_{17,18,24} : -(f_P)_M^{n+1/2}(1 - \sqrt{\frac{(A_0^P)_M^{n+1}}{x_{10}}}) + (f_{d_1,d_2,d_3})_0^{n+1/2}(1 - \sqrt{\frac{(A_0^{d_1,d_2,d_3})_0^{n+1}}{x_{13,16,22}}})$

The first-order accuracy Newton-Raphson scheme is used to solve the 24 unknowns and 24 equations.

$$\boldsymbol{x}_{j+1} = \boldsymbol{x}_j - D^{-1}\boldsymbol{f} \tag{A.1}$$

where $\boldsymbol{x}$ represents $\begin{bmatrix} x_1, & x_2, & \cdots & x_{24} \end{bmatrix}^T$ and $\boldsymbol{f}$ represents $\begin{bmatrix} f_1, & f_2, & \cdots & f_{24} \end{bmatrix}^T$; D is the Jacobian matrix. The jacobian matrix is presented below.

$$
\left\{\begin{array}{cccccccccccccccccccccc}
-1 & 0 & k_1 & 0 & 0 & 0 & 0 & 0 & 0 & 0 & 0 & k_2 & 0 & 0 & 0 & 0 & 0 & 0 & 0 & 0 & 0 & 0 & 0 & 0 \\
0 & 0 & 0 & -1 & 0 & k_3 & 0 & 0 & 0 & 0 & 0 & 0 & 0 & 0 & k_4 & 0 & 0 & 0 & 0 & 0 & 0 & 0 & 0 & 0 \\
0 & 0 & 0 & 0 & 0 & 0 & -1 & 0 & k_5 & 0 & 0 & 0 & 0 & 0 & 0 & 0 & 0 & k_6 & 0 & 0 & 0 & 0 & 0 & 0 \\
0 & 0 & \delta_t/\delta_x & 0 & 0 & 0 & 0 & 0 & 0 & -1 & 0 & 0 & 0 & 0 & 0 & 0 & 0 & 0 & 0 & 0 & 0 & 0 & 0 & 0 \\
0 & 0 & 0 & 0 & 0 & \delta_t/\delta_x & 0 & 0 & 0 & 0 & 0 & 0 & -1 & 0 & 0 & 0 & 0 & 0 & 0 & 0 & 0 & 0 & 0 & 0 \\
0 & 0 & 0 & 0 & 0 & 0 & 0 & 0 & \delta_t/\delta_x & 0 & 0 & 0 & 0 & 0 & 0 & 0 & -1 & 0 & 0 & 0 & 0 & 0 & 0 & 0 \\
0 & -1 & 0.5 & 0 & 0 & 0 & 0 & 0 & 0 & 0 & 0 & 0 & 0 & 0 & 0 & 0 & 0 & 0 & 0 & 0 & 0 & 0 & 0 & 0 \\
0 & 0 & 0 & 0 & -1 & 0.5 & 0 & 0 & 0 & 0 & 0 & 0 & 0 & 0 & 0 & 0 & 0 & 0 & 0 & 0 & 0 & 0 & 0 & 0 \\
0 & 0 & 0 & 0 & 0 & 0 & 0 & -1 & 0.5 & 0 & 0 & 0 & 0 & 0 & 0 & 0 & 0 & 0 & 0 & 0 & 0 & 0 & 0 & 0 \\
0 & 0 & 0 & 0 & 0 & 0 & 0 & 0 & 0 & 0 & -1 & 0.5 & 0 & 0 & 0 & 0 & 0 & 0 & 0 & 0 & 0 & 0 & 0 & 0 \\
0 & 0 & 0 & 0 & 0 & 0 & 0 & 0 & 0 & 0 & 0 & 0 & 0 & -1 & 0.5 & 0 & 0 & 0 & 0 & 0 & 0 & 0 & 0 & 0 \\
0 & 0 & 0 & 0 & 0 & 0 & 0 & 0 & 0 & 0 & 0 & 0 & 0 & 0 & 0 & 0 & -1 & 0.5 & 0 & 0 & 0 & 0 & 0 & 0 \\
0 & -1 & 0 & 0 & 1 & 0 & 0 & 1 & 0 & 0 & 0 & 0 & 0 & 0 & 0 & 0 & 0 & 0 & 0 & 1 & 0 & 0 & 0 & 0 \\
-1 & 0 & 0 & 1 & 0 & 0 & 1 & 0 & 0 & 0 & 0 & 0 & 0 & 0 & 0 & 0 & 0 & 0 & 1 & 0 & 0 & 0 & 0 & 0 \\
0 & 0 & 0 & 0 & 0 & 0 & 0 & 0 & 0 & 0 & k_7 & 0 & 0 & k_8 & 0 & 0 & 0 & 0 & 0 & 0 & 0 & 0 & 0 & 0 \\
0 & 0 & 0 & 0 & 0 & 0 & 0 & 0 & 0 & 0 & k_7 & 0 & 0 & 0 & 0 & 0 & k_9 & 0 & 0 & 0 & 0 & 0 & 0 & 0 \\
0 & 0 & 0 & 0 & 0 & 0 & 0 & 0 & 0 & k_{10} & 0 & 0 & k_{11} & 0 & 0 & 0 & 0 & 0 & 0 & 0 & 0 & 0 & 0 & 0 \\
0 & 0 & 0 & 0 & 0 & 0 & 0 & 0 & 0 & k_{10} & 0 & 0 & 0 & 0 & k_{12} & 0 & 0 & 0 & 0 & 0 & 0 & 0 & 0 & 0 \\
0 & 0 & 0 & 0 & 0 & 0 & 0 & 0 & 0 & 0 & 0 & 0 & 0 & 0 & 0 & 0 & 0 & 0 & -1 & 0 & k_{23} & 0 & 0 & k_{24} \\
0 & 0 & 0 & 0 & 0 & 0 & 0 & 0 & 0 & 0 & 0 & 0 & 0 & 0 & 0 & 0 & 0 & 0 & 0 & \delta_t/\delta_x & -1 & 0 & 0 & 0 \\
0 & 0 & 0 & 0 & 0 & 0 & 0 & 0 & 0 & 0 & 0 & 0 & 0 & 0 & 0 & 0 & 0 & 0 & -1 & 0.5 & 0 & 0 & 0 & 0 \\
0 & 0 & 0 & 0 & 0 & 0 & 0 & 0 & 0 & 0 & 0 & 0 & 0 & 0 & 0 & 0 & 0 & 0 & 0 & 0 & 0 & -1 & 0.5 & 0 \\
0 & 0 & 0 & 0 & 0 & 0 & 0 & 0 & 0 & 0 & k_7 & 0 & 0 & 0 & 0 & 0 & 0 & 0 & 0 & 0 & 0 & k_{25} & 0 & 0 \\
0 & 0 & 0 & 0 & 0 & 0 & 0 & 0 & 0 & k_{10} & 0 & 0 & 0 & 0 & 0 & 0 & 0 & 0 & 0 & 0 & k_{26} & 0 & 0 & 0
\end{array}\right\}
$$

where

$k_1 = -\frac{\Delta t}{\Delta x}\frac{2x_3}{x_{12}} + \frac{\Delta t}{2}\frac{dF(M+1/2,x_3,x_{12})}{dx_3}$

$k_2 = \frac{\Delta t}{\Delta x}(\frac{(x_3)^2}{(x_{12})^2} - \frac{dB(M+1/2,x_{12})}{dx_{12}}) + \frac{\Delta t}{2}(\frac{dF(M+1/2,x_3,x_{12}}{dx_{12}}) + \frac{d^2B(M+1/2,x_{12})}{dxdx_{12}})$

$$k_3 = \frac{\Delta t}{\Delta x}\frac{2x_6}{x_{15}} + \frac{\Delta t}{2}\frac{dF(-1/2,x_6,x_{15})}{dx_6}$$

$$k_4 = \frac{\Delta t}{\Delta x}(-\frac{(x_6)^2}{(x_{15})^2} + \frac{dB(-1/2,x_{15})}{dx_{15}}) + \frac{\Delta t}{2}(\frac{dF(-1/2,x_6,x_{15})}{dx_{15}} + \frac{d^2B(-1/2,x_{15})}{dxdx_{15}})$$

$$k_5 = \frac{\Delta t}{\Delta x}\frac{2x_9}{x_{18}} + \frac{\Delta t}{2}\frac{dF(-1/2,x_9,x_{18})}{dx_9}$$

$$k_6 = (\frac{-(x_9)^2}{(x_{18})^2} + \frac{dB(-1/2,x_{18})}{dx_{18}}) + \frac{\Delta t}{2}(\frac{dF(-1/2,x_9,x_{18})}{dx_{18}} + \frac{d^2B(-1/2,x_{18})}{dxdx_{18}})$$

$$k_7 = -\frac{dP(M,x_{11})}{dA}$$

$$k_8 = -\frac{dP(0,x_{14})}{dA}$$

$$k_9 = -\frac{dP(0,x_{17})}{dA}$$

$$k_{10} = -\frac{dP(M,x_{10})}{dA}$$

$$k_{11} = -\frac{dP(0,x_{13})}{dA}$$

$$k_{12} = -\frac{dP(0,x_{16})}{dA}$$

$$k_{23} = \frac{\Delta t}{\Delta x}\frac{2x_{19}}{x_{24}} + \frac{\Delta t}{2}\frac{dF(-1/2,x_{21},x_{24})}{dx_{21}}$$

$$k_{24} = \frac{\Delta t}{\Delta x}(-\frac{(x_{19})^2}{(x_{24})^2} + \frac{dB(-1/2,x_{19})}{dx_{24}}) + \frac{\Delta t}{2}(\frac{dF(-1/2,x_{19},x_{24})}{dx_{24}} + \frac{d^2B(-1/2,x_{24})}{dxdx_{24}})$$

$$k_{25} = -\frac{dP(0,x_{23})}{dA}$$

$$k_{26} = -\frac{dP(0,x_{22})}{dA}$$

And

$$\frac{dB(L,x_i)}{dx_i} = \frac{f_L}{2}\sqrt{(\frac{(A_0)_L}{x_i})}$$

$$\frac{d^2B(L,x_i)}{dxdx_i} = (\frac{dr_0}{dx}(\frac{1}{\sqrt{x_i}}(f\sqrt{\pi} + \frac{df}{(dr_0)_L}\sqrt{(A_0)_L} - \frac{df}{(dr_0)_L}))$$

$$\frac{dF(L,x_{i1},x_{i2})}{dx_{i2}} = \frac{2\pi(r_0)_L}{\delta Re}\frac{x_{i1}}{(x_{i2})^2}$$

$$\frac{dF(L,x_{i1},x_{i2})}{dx_{i1}} = \frac{2\pi(r_0)_L}{\delta Re}\frac{1}{(x_{i2})^2}$$

$$\frac{dP(L,x_i)}{dx_i} = -\frac{f_L}{2}\sqrt{(\frac{(A_0)_L}{(x_i)^3})}$$

And the convergence criterion for the Newton method is,

$$| \boldsymbol{x}_{j+1} - \boldsymbol{x}_j | \leq 1e-8 \tag{A.2}$$

A.2 Iteration Method Solving Two Daughter Vessels Bifurcation with Stenosis Model

The governing equation at bifurcation provides 18 equations and 18 unknowns.

$x_1 = (q^p)_M^{n+1}$ $x_2 = (q^p)_M^{n+1/2}$ $x_3 = (q^p)_{M+1/2}^{n+1/2}$

$x_4 = (q^{d_1})_0^{n+1}$ $x_5 = (q^{d_1})_0^{n+1/2}$ $x_6 = (q^{d_1})_{-1/2}^{n+1/2}$

$x_7 = (q^{d_2})_0^{n+1}$ $x_8 = (q^{d_2})_0^{n+1/2}$ $x_9 = (q^{d_2})_{-1/2}^{n+1/2}$

$x_{10} = (A^p)_M^{n+1}$ $x_{11} = (A^p)_M^{n+1/2}$ $x_{12} = (A^p)_{M+1/2}^{n+1/2}$

$x_{13} = (A^{d_1})_0^{n+1}$ $x_{14} = (A^{d_1})_0^{n+1/2}$ $x_{15} = (A^{d_1})_{-1/2}^{n+1/2}$

$x_{16} = (A^{d_2})_0^{n+1}$ $x_{17} = (A^{d_2})_0^{n+1/2}$ $x_{18} = (A^{d_2})_{-1/2}^{n+1/2}$

$f_{stenosis1} : -x_1 + (q_P)_M^n - \frac{\Delta t}{\Delta x}(\frac{x_3^2}{x_{12}} + B(M+1/2, x_{12}) - (R_2)_{M-1/2}^{n+1/2}) + \frac{\Delta t}{2}(F(M+1/2, x_3, x_{12})$
$+ \frac{dB(M+1/2, x_{12})}{dx} + (S_2)_{M-1/2}^{n+1/2})$

$f_{stenosis2,3} : -x_{4,7} + (q_{d_1,d_2})_0^n - \frac{\Delta t}{\Delta x}((R_2^{d_1,d_2})_{M+1/2}^{n+1/2} - B(-1/2, x_{15,18}) - \frac{x_{6,9}^2}{x_{15,18}})$
$+ \frac{\Delta t}{2}(S_2^{d_1,d_2})_{1/2}^{n+1/2} + F(-1/2, x_{6,9}, x_{15,18}) + \frac{dB(-1/2, x_{15,18}}{dx})$

$f_{stenosis4} : -x_{10} + (A^P)_M^n - \frac{\Delta t}{\Delta x}(-x_3 - (q^P)_{M-1/2}^{n+1/2})$

$f_{stenosis5,6} : -x_{13,16} + (A_{d_1,d_2})_0^n - \frac{\Delta t}{\Delta x}(-x_{6,9} + (q_{d_1,d_2})_{M+1/2}^{n+1/2})$

$f_{stenosis7} : -x_2 + \frac{1}{2}(x_3 + (q_P)_{M-1/2}^{n+1/2})$

$f_{stenosis8,9} : -x_{5,8} + \frac{1}{2}(x_{6,9} + (q_{d_1,d_2})_{1/2}^{n+1/2})$

$f_{stenosis10} : -x_{11} + \frac{1}{2}(x_{12} + (A_P)_{M-1/2}^{n+1/2})$

$f_{stenosis11,12} : -x_{14,17} + \frac{1}{2}(x_{15,18} + (A_{d_1,d_2})_{M+1/2}^{n+1/2})$

$f_{stenosis13,14} : -x_{2,1} + x_{5,4} + x_{8,7}$

$$f_{stenosis15,16} : -(f_P)_M^{n+1/2}(1 - \sqrt{\frac{(A_0^P)_M^{n+1/2}}{x_{11}}}) + \Delta P_M^{n+1/2} + (f_{d_1,d_2})_0^{n+1/2}(1 - \sqrt{\frac{(A_0^{d_1,d_2})_0^{n+1/2}}{x_{14,17}}})$$

where

$$\Delta P_M^{n+1/2} = \frac{\mu K_v}{2\pi r_p^3} x_2 + \frac{\rho K_t}{2A_p^2}(\frac{A_p}{A_s} - 1)^2 x_2 \mid x_2 \mid + L_s \frac{\rho K_u}{A_p}(x_2 - q_M^{n-1/2})$$

$$f_{stenosis17,18} : -(f_P)_M^{n+1}(1 - \sqrt{\frac{(A_0^P)_M^{n+1}}{x_{10}}}) + \Delta P_M^{n+1} + (f_{d_1,d_2})_0^{n+1}(1 - \sqrt{\frac{(A_0^{d_1,d_2})_0^{n+1}}{x_{13,16}}})$$

where

$$\Delta P_M^{n+1} = \frac{\mu K_v}{2\pi r_p^3} x_1 + \frac{\rho K_t}{2A_p^2}(\frac{A_p}{A_s} - 1)^2 x_1 \mid x_1 \mid + L_s \frac{\rho K_u}{A_p}(x_1 - q_M^n)$$

The first-order accuracy Newton-Raphson scheme is used to solve the 18 unknowns and 18 equations.

$$\boldsymbol{x}_{j+1} = \boldsymbol{x}_j - D_{stenosis}^{-1} \boldsymbol{f}_{stenosis} \tag{A.3}$$

where $\boldsymbol{x}$ represents $\Big[x_1, x_2, \cdots x_{18}\Big]^T$ and $\boldsymbol{f}_{stenosis}$ represents $\Big[f_1, f_2, \cdots f_{18}\Big]^T$; $D_{stenosis}$ is the Jacobian matrix. The jacobian matrix is presented below.

$$D_{stenosis} = \begin{Bmatrix}
-1 & 0 & k_1 & 0 & 0 & 0 & 0 & 0 & 0 & 0 & 0 & k_2 & 0 & 0 & 0 & 0 & 0 & 0 \\
0 & 0 & 0 & -1 & 0 & k_3 & 0 & 0 & 0 & 0 & 0 & 0 & 0 & 0 & k_4 & 0 & 0 & 0 \\
0 & 0 & 0 & 0 & 0 & 0 & -1 & 0 & k_5 & 0 & 0 & 0 & 0 & 0 & 0 & 0 & 0 & k_6 \\
0 & 0 & -\delta_t/\delta_x & 0 & 0 & 0 & 0 & 0 & 0 & -1 & 0 & 0 & 0 & 0 & 0 & 0 & 0 & 0 \\
0 & 0 & 0 & 0 & 0 & \delta_t/\delta_x & 0 & 0 & 0 & 0 & 0 & 0 & -1 & 0 & 0 & 0 & 0 & 0 \\
0 & 0 & 0 & 0 & 0 & 0 & 0 & 0 & \delta_t/\delta_x & 0 & 0 & 0 & 0 & 0 & 0 & 0 & -1 & 0 \\
0 & -1 & 0.5 & 0 & 0 & 0 & 0 & 0 & 0 & 0 & 0 & 0 & 0 & 0 & 0 & 0 & 0 & 0 \\
0 & 0 & 0 & 0 & -1 & 0.5 & 0 & 0 & 0 & 0 & 0 & 0 & 0 & 0 & 0 & 0 & 0 & 0 \\
0 & 0 & 0 & 0 & 0 & 0 & 0 & -1 & 0.5 & 0 & 0 & 0 & 0 & 0 & 0 & 0 & 0 & 0 \\
0 & 0 & 0 & 0 & 0 & 0 & 0 & 0 & 0 & 0 & -1 & 0.5 & 0 & 0 & 0 & 0 & 0 & 0 \\
0 & 0 & 0 & 0 & 0 & 0 & 0 & 0 & 0 & 0 & 0 & 0 & 0 & -1 & 0.5 & 0 & 0 & 0 \\
0 & 0 & 0 & 0 & 0 & 0 & 0 & 0 & 0 & 0 & 0 & 0 & 0 & 0 & 0 & 0 & -1 & 0.5 \\
0 & -1 & 0 & 0 & 1 & 0 & 0 & 1 & 0 & 0 & 0 & 0 & 0 & 0 & 0 & 0 & 0 & 0 \\
-1 & 0 & 0 & 1 & 0 & 0 & 1 & 0 & 0 & 0 & 0 & 0 & 0 & 0 & 0 & 0 & 0 & 0 \\
0 & 0 & 0 & 0 & k_{13} & 0 & 0 & 0 & 0 & 0 & k_7 & 0 & 0 & k_8^* & 0 & 0 & 0 & 0 \\
0 & 0 & 0 & 0 & 0 & 0 & 0 & 0 & 0 & 0 & k_7 & 0 & 0 & 0 & 0 & 0 & k_9 & 0 \\
0 & 0 & 0 & k_{14} & 0 & 0 & 0 & 0 & 0 & k_{10} & 0 & 0 & k_{11}^* & 0 & 0 & 0 & 0 & 0 \\
0 & 0 & 0 & 0 & 0 & 0 & 0 & 0 & 0 & k_{10} & 0 & 0 & 0 & 0 & 0 & k_{12} & 0 & 0
\end{Bmatrix}$$

Compared with the Jacobian matrix D in the bifurcation case, $D_{stenosis}$ introduces four new terms, which are k_{13}, k_{14}, k_8^* and k_{11}^*.

$k_{13} = \frac{\mu K_v}{2\pi r_{d1}^3} + \frac{\rho K_t}{2A_{d1}^2}(\frac{A_{d1}}{A_s} - 1)^2 \mid x_5 \mid *2 + L_s \frac{\rho K_u}{A_{d1}}$

$k_{14} = \frac{\mu K_v}{2\pi r_{d1}^3} + \frac{\rho K_t}{2A_{d1}^2}(\frac{A_{d1}}{A_s} - 1)^2 \mid x_4 \mid *2 + L_s \frac{\rho K_u}{A_{d1}}$

$k_8^* = -\frac{dP(0,x_{14})}{dA} - \rho K_t (x_{14})^2 \mid x_5 \mid x_5 - L_s \frac{\rho K_u}{(x_{14})^2}(x_5 - (q_{d1})_0^{n-1/2})$

$k_{11}^* = -\frac{dP(0,x_{13})}{dA} - \rho K_t (x_{13})^2 \mid x_4 \mid x_4 - L_s \frac{\rho K_u}{(x_{13})^2}(x_4 - (q_{d1})_0^{n})$

And the convergence criterion for the Newton method is,

$$| \boldsymbol{x}_{j+1} - \boldsymbol{x}_j | \leq 1e-8 \tag{A.4}$$

A.3 Iteration Method Solving Three Daughter Vessels Bifurcation with Stenosis Model

The governing equation at bifurcation provides 24 equations and 24 unknowns.

$x_1 = (q^p)_M^{n+1}$ $x_2 = (q^p)_M^{n+1/2}$ $x_3 = (q^p)_{M+1/2}^{n+1/2}$

$x_4 = (q^{d_1})_0^{n+1}$ $x_5 = (q^{d_1})_0^{n+1/2}$ $x_6 = (q^{d_1})_{-1/2}^{n+1/2}$

$x_7 = (q^{d_2})_0^{n+1}$ $x_8 = (q^{d_2})_0^{n+1/2}$ $x_9 = (q^{d_2})_{-1/2}^{n+1/2}$

$x_{10} = (A^p)_M^{n+1}$ $x_{11} = (A^p)_M^{n+1/2}$ $x_{12} = (A^p)_{M+1/2}^{n+1/2}$

$x_{13} = (A^{d_1})_0^{n+1}$ $x_{14} = (A^{d_1})_0^{n+1/2}$ $x_{15} = (A^{d_1})_{-1/2}^{n+1/2}$

$x_{16} = (A^{d_2})_0^{n+1}$ $x_{17} = (A^{d_2})_0^{n+1/2}$ $x_{18} = (A^{d_2})_{-1/2}^{n+1/2}$

$x_{19} = (q^{d_3})_0^{n+1}$ $x_{20} = (q^{d_3})_0^{n+1/2}$ $x_{21} = (q^{d_3})_{-1/2}^{n+1/2}$

$x_{22} = (A^{d_3})_0^{n+1}$ $x_{23} = (A^{d_3})_0^{n+1/2}$ $x_{24} = (A^{d_3})_{-1/2}^{n+1/2}$

$f_{stenosis1} : -x_1 + (q_P)_M^n - \frac{\Delta t}{\Delta x}(\frac{x_3^2}{x_{12}} + B(M+1/2, x_{12}) - (R_2)_{M-1/2}^{n+1/2}) + \frac{\Delta t}{2}(F(M+1/2, x_3, x_{12})$
$+ \frac{dB(M+1/2, x_{12})}{dx} + (S_2)_{M-1/2}^{n+1/2})$

$f_{stenosis2,3,19} : -x_{4,7,19} + (q_{d_1,d_2,d_3})_0^n - \frac{\Delta t}{\Delta x}((R_2^{d_1,d_2,d_3})_{M+1/2}^{n+1/2} - B(-1/2, x_{15,18,24}) - \frac{x_{6,9,21}^2}{x_{15,18,24}})$
$+ \frac{\Delta t}{2}(S_2^{d_1,d_2,d_3})_{1/2}^{n+1/2} + F(-1/2, x_{6,9,21}, x_{15,18,24}) + \frac{dB(-1/2, x_{15,18,24}}{dx})$

$f_{stenosis4} : -x_{10} + (A^P)_M^n - \frac{\Delta t}{\Delta x}(-x_3 - (q^P)_{M-1/2}^{n+1/2})$

$f_{stenosis5,6,20} : -x_{13,16,22} + (A_{d_1,d_2,d_3})_0^n - \frac{\Delta t}{\Delta x}(-x_{6,9,21} + (q_{d_1,d_2,d_3})_{M+1/2}^{n+1/2})$

$f_{stenosis7} : -x_2 + \frac{1}{2}(x_3 + (q_P)_{M-1/2}^{n+1/2})$

$f_{stenosis8,9,21} : -x_{5,8,20} + \frac{1}{2}(x_{6,9,21} + (q_{d_1,d_2,d_3})_{1/2}^{n+1/2})$

$f_{stenosis10} : -x_{11} + \frac{1}{2}(x_{12} + (A_P)_{M-1/2}^{n+1/2})$

$f_{stenosis11,12,22} : -x_{14,17,23} + \frac{1}{2}(x_{15,18,24} + (A_{d_1,d_2,d_3})_{M+1/2}^{n+1/2})$

$f_{stenosis13,14} : -x_{2,1} + x_{5,4} + x_{8,7} + x_{20,19}$

$f_{stenosis15} : -(f_P)_M^{n+1/2}(1 - \sqrt{\frac{(A_0^P)_M^{n+1/2}}{x_{11}}}) + (\Delta P_{d1})_0^{n+1/2} + (f_{d_1})_0^{n+1/2}(1 - \sqrt{\frac{(A_0^{d_1})_0^{n+1/2}}{x_{14}}})$

$f_{stenosis16,23} : -(f_P)_M^{n+1/2}(1 - \sqrt{\frac{(A_0^P)_M^{n+1/2}}{x_{11}}}) + (f_{d_2,d_3})_0^{n+1/2}(1 - \sqrt{\frac{(A_0^{d_2,d_3})_0^{n+1/2}}{x_{17,23}}})$

where

$(\Delta P_{d1})_0^{n+1/2} = \frac{\mu K_v}{2\pi r_p^3} x_5 + \frac{\rho K_t}{2A_{d1}^2}(\frac{A_{d1}}{A_s} - 1)^2 x_5 \mid x_5 \mid + L_s \frac{\rho K_u}{A_d 1}(x_5 - (q_{d1})_0^{n-1/2})$

$f_{stenosis17} : -(f_P)_M^{n+1}(1 - \sqrt{\frac{(A_0^P)_M^{n+1}}{x_{10}}}) + (\Delta P_{d1})_0^{n+1} + (f_{d_1})_0^{n+1}(1 - \sqrt{\frac{(A_0^{d_1})_0^{n+1}}{x_{13}}})$

where

$(\Delta P_{d1})_0^{n+1} = \frac{\mu K_v}{2\pi r_p^3} x_4 + \frac{\rho K_t}{2A_{d1}^2}(\frac{A_{d1}}{A_s} - 1)^2 x_4 \mid x_4 \mid + L_s \frac{\rho K_u}{A_d 1}(x_4 - (q^{d1})_0^n)$

$f_{stenosis18,24} : -(f_P)_M^{n+1}(1 - \sqrt{\frac{(A_0^P)_M^{n+1}}{x_{10}}}) + (f_{d_2,d_3})_0^{n+1}(1 - \sqrt{\frac{(A_0^{d_2,d_3})_0^{n+1}}{x_{16,22}}})$

The first-order accuracy Newton-Raphson scheme is used to solve the 24 unknowns and 24 equations.

$$\boldsymbol{x}_{j+1} = \boldsymbol{x}_j - D_{stenosis}^{-1} \boldsymbol{f}_{stenosis} \tag{A.5}$$

where $\boldsymbol{x}$ represents $\left[x_1, x_2, \cdots x_{24}\right]^T$ and $\boldsymbol{f}_{stenosis}$ represents $\left[f_1, f_2, \cdots f_{24}\right]^T$; $D_{stenosis}$ is the Jacobian matrix. The jacobian matrix is presented below.

$$
D_{stenosis} = \begin{Bmatrix}
-1 & 0 & k_1 & 0 & 0 & 0 & 0 & 0 & 0 & 0 & 0 & k_2 & 0 & 0 & 0 & 0 & 0 & 0 & 0 & 0 & 0 & 0 & 0 & 0 \\
0 & 0 & 0 & -1 & 0 & k_3 & 0 & 0 & 0 & 0 & 0 & 0 & 0 & 0 & k_4 & 0 & 0 & 0 & 0 & 0 & 0 & 0 & 0 & 0 \\
0 & 0 & 0 & 0 & 0 & 0 & -1 & 0 & k_5 & 0 & 0 & 0 & 0 & 0 & 0 & 0 & 0 & k_6 & 0 & 0 & 0 & 0 & 0 & 0 \\
0 & 0 & \delta_t/\delta_x & 0 & 0 & 0 & 0 & 0 & 0 & -1 & 0 & 0 & 0 & 0 & 0 & 0 & 0 & 0 & 0 & 0 & 0 & 0 & 0 & 0 \\
0 & 0 & 0 & 0 & 0 & \delta_t/\delta_x & 0 & 0 & 0 & 0 & 0 & 0 & -1 & 0 & 0 & 0 & 0 & 0 & 0 & 0 & 0 & 0 & 0 & 0 \\
0 & 0 & 0 & 0 & 0 & 0 & 0 & 0 & \delta_t/\delta_x & 0 & 0 & 0 & 0 & 0 & 0 & 0 & -1 & 0 & 0 & 0 & 0 & 0 & 0 & 0 \\
0 & -1 & 0.5 & 0 & 0 & 0 & 0 & 0 & 0 & 0 & 0 & 0 & 0 & 0 & 0 & 0 & 0 & 0 & 0 & 0 & 0 & 0 & 0 & 0 \\
0 & 0 & 0 & 0 & -1 & 0.5 & 0 & 0 & 0 & 0 & 0 & 0 & 0 & 0 & 0 & 0 & 0 & 0 & 0 & 0 & 0 & 0 & 0 & 0 \\
0 & 0 & 0 & 0 & 0 & 0 & 0 & -1 & 0.5 & 0 & 0 & 0 & 0 & 0 & 0 & 0 & 0 & 0 & 0 & 0 & 0 & 0 & 0 & 0 \\
0 & 0 & 0 & 0 & 0 & 0 & 0 & 0 & 0 & 0 & -1 & 0.5 & 0 & 0 & 0 & 0 & 0 & 0 & 0 & 0 & 0 & 0 & 0 & 0 \\
0 & 0 & 0 & 0 & 0 & 0 & 0 & 0 & 0 & 0 & 0 & 0 & 0 & -1 & 0.5 & 0 & 0 & 0 & 0 & 0 & 0 & 0 & 0 & 0 \\
0 & 0 & 0 & 0 & 0 & 0 & 0 & 0 & 0 & 0 & 0 & 0 & 0 & 0 & 0 & 0 & -1 & 0.5 & 0 & 0 & 0 & 0 & 0 & 0 \\
0 & -1 & 0 & 0 & 1 & 0 & 0 & 1 & 0 & 0 & 0 & 0 & 0 & 0 & 0 & 0 & 0 & 0 & 0 & 1 & 0 & 0 & 0 & 0 \\
-1 & 0 & 0 & 1 & 0 & 0 & 1 & 0 & 0 & 0 & 0 & 0 & 0 & 0 & 0 & 0 & 0 & 0 & 1 & 0 & 0 & 0 & 0 & 0 \\
0 & 0 & 0 & 0 & k_{13} & 0 & 0 & 0 & 0 & 0 & k_7 & 0 & 0 & k_8^* & 0 & 0 & 0 & 0 & 0 & 0 & 0 & 0 & 0 & 0 \\
0 & 0 & 0 & 0 & 0 & 0 & 0 & 0 & 0 & 0 & k_7 & 0 & 0 & 0 & 0 & 0 & k_9 & 0 & 0 & 0 & 0 & 0 & 0 & 0 \\
0 & 0 & 0 & k_{14} & 0 & 0 & 0 & 0 & 0 & k_{10} & 0 & 0 & k_{11}^* & 0 & 0 & 0 & 0 & 0 & 0 & 0 & 0 & 0 & 0 & 0 \\
0 & 0 & 0 & 0 & 0 & 0 & 0 & 0 & 0 & k_{10} & 0 & 0 & 0 & 0 & k_{12} & 0 & 0 & 0 & 0 & 0 & 0 & 0 & 0 & 0 \\
0 & 0 & 0 & 0 & 0 & 0 & 0 & 0 & 0 & 0 & 0 & 0 & 0 & 0 & 0 & 0 & 0 & 0 & -1 & 0 & k_{23} & 0 & 0 & k_{24} \\
0 & 0 & 0 & 0 & 0 & 0 & 0 & 0 & 0 & 0 & 0 & 0 & 0 & 0 & 0 & 0 & 0 & 0 & 0 & \delta_t/\delta_x & -1 & 0 & 0 & \\
0 & 0 & 0 & 0 & 0 & 0 & 0 & 0 & 0 & 0 & 0 & 0 & 0 & 0 & 0 & 0 & 0 & 0 & -1 & 0.5 & 0 & 0 & 0 & \\
0 & 0 & 0 & 0 & 0 & 0 & 0 & 0 & 0 & 0 & 0 & 0 & 0 & 0 & 0 & 0 & 0 & 0 & 0 & 0 & -1 & 0.5 & & \\
0 & 0 & 0 & 0 & 0 & 0 & 0 & 0 & 0 & 0 & k_7 & 0 & 0 & 0 & 0 & 0 & 0 & 0 & 0 & 0 & k_{25} & 0 & & \\
0 & 0 & 0 & 0 & 0 & 0 & 0 & 0 & 0 & k_{10} & 0 & 0 & 0 & 0 & 0 & 0 & 0 & 0 & 0 & 0 & k_{26} & 0 & &
\end{Bmatrix}
$$

Compared with the Jacobian matrix D in the bifurcation case, $D_{stenosis}$ introduces four new terms,

which are k_{13}, k_{14}, k_8^* and k_{11}^*.

$k_{13} = \frac{\mu K_v}{2\pi r_{d1}^3} + \frac{\rho K_t}{2A_{d1}^2}(\frac{A_{d1}}{A_s} - 1)^2 \mid x_5 \mid *2 + L_s \frac{\rho K_u}{A_{d1}}$

$k_{14} = \frac{\mu K_v}{2\pi r_{d1}^3} + \frac{\rho K_t}{2A_{d1}^2}(\frac{A_{d1}}{A_s} - 1)^2 \mid x_4 \mid *2 + L_s \frac{\rho K_u}{A_{d1}}$

$k_8^* = -\frac{dP(0,x_{14})}{dA} - \rho K_t (x_{14})^2 \mid x_5 \mid x_5 - L_s \frac{\rho K_u}{(x_{14})^2}(x_5 - (q_{d1})_0^{n-1/2})$

$k_{11}^* = -\frac{dP(0,x_{13})}{dA} - \rho K_t (x_{13})^2 \mid x_4 \mid x_4 - L_s \frac{\rho K_u}{(x_{13})^2}(x_4 - (q_{d1})_0^{n})$

And the convergence criterion for the Newton method is,

$$\mid \boldsymbol{x}_{j+1} - \boldsymbol{x}_j \mid \leq 1e-8 \tag{A.6}$$

REFERENCES

[1] World Health Organization. *The world health report 2002: reducing risks, promoting healthy life*. World Health Organization, 2002.

[2] Kathleen Strong, Colin Mathers, and Ruth Bonita. "Preventing stroke: saving lives around the world". In: *The Lancet Neurology* 6.2 (2007), pp. 182–187.

[3] Wenjuan Xu et al. "Prevalence and outcome of young stroke patients with middle cerebral artery stenosis". In: *BMC neurology* 21.1 (2021), pp. 1–10.

[4] Mohamad El Amki and Susanne Wegener. "Improving cerebral blood flow after arterial recanalization: a novel therapeutic strategy in stroke". In: *International journal of molecular sciences* 18.12 (2017), p. 2669.

[5] David S. Liebeskind. "Collateral circulation". In: *Stroke* 34.9 (2003), pp. 2279–2284.

[6] Neil M Borden. *3D angiographic atlas of neurovascular anatomy and pathology*. Cambridge University Press, 2006.

[7] Bernard J. Alpers, Richard G. Berry, and Richard M. Paddison. "Anatomical studies of the circle of Willis in normal brain". In: *AMA Archives of Neurology Psychiatry* 81.4 (1959), pp. 409–418.

[8] *Circle of wills*. 2008. URL: https://courses.lumenlearning.com/suny-ap1/chapter/circulation-and-the-central-nervous-system/.

[9] Maurice Tatelman. "Pathways of cerebral collateral circulation". In: *Radiology* 75.3 (1960), pp. 349–362.

[10] Matthew A Ziegler et al. "Marvels, mysteries, and misconceptions of vascular compensation to peripheral artery occlusion". In: *Microcirculation* 17.1 (2010), pp. 3–20.

[11] Fun-Sun F. Yao, Manuel L. Fontes, and eds Vinod Malhotra. "Yao Artusio's anesthesiology: problem-oriented patient management." In: (2008).

[12] Hiroyuki Kawano et al. "Relationship between collateral status, contrast transit, and contrast density in acute ischemic stroke". In: *Stroke* 47.3 (2016), pp. 742–749.

[13] LCS Souza et al. "Malignant CTA collateral profile is highly specific for large admission DWI infarct core and poor outcome in acute stroke". In: *American Journal of Neuroradiology* 33.7 (2012), pp. 1331–1336.

[14] Andreas MJ Frölich et al. "Time-resolved assessment of collateral flow using 4D CT angiography in large-vessel occlusion stroke". In: *European radiology* 24 (2014), pp. 390–396.

[15] Matthew B Maas et al. "Collateral vessels on CT angiography predict outcome in acute ischemic stroke". In: *Stroke* 40.9 (2009), pp. 3001–3005.

[16] Roland N. Pittman. "Regulation of tissue oxygenation". In: *Colloquium series on integrated systems physiology: from molecule to function* 3.3 (2011), pp. 1–100.

[17] Colin Gerald Caro et al. *The mechanics of the circulation*. Cambridge University Press, 2012.

[18] Bruce Blaus. "Medical gallery of Blausen medical 2014". In: *Wiki J Med* 1.2 (2014), p. 10.

[19] ROBERT M. Olson. "Aortic blood pressure and velocity as a function of time and position". In: *Journal of applied physiology* 24.4 (1968), pp. 563–569.

[20] Yubing Shi, Patricia Lawford, and Rodney Hose. "Review of zero-D and 1-D models of blood flow in the cardiovascular system". In: *Biomedical engineering online* 10.1 (2011), p. 32.

[21] Pablo Javier Blanco et al. "Comparison of 1D and 3D models for the estimation of fractional flow reserve". In: *Scientific reports* 8.1 (2018), p. 17275.

[22] Yuan-cheng Fung. *Biomechanics: circulation*. Springer Science Business Media, 2013.

[23] Charalambos Vlachopoulos, Michael O'Rourke, and Wilmer W Nichols. *McDonald's blood flow in arteries: theoretical, experimental and clinical principles*. CRC press, 2011.

[24] Mette S Olufsen. "Structured tree outflow condition for blood flow in larger systemic arteries". In: *American journal of physiology-Heart and circulatory physiology* 276.1 (1999), H257–H268.

[25] Jordi Alastruey et al. "Pulse wave propagation in a model human arterial network: assessment of 1-D visco-elastic simulations against in vitro measurements". In: *Journal of biomechanics* 44.12 (2011), pp. 2250–2258.

[26] Yuan-cheng Fung. *Biomechanics: mechanical properties of living tissues*. Springer Science & Business Media, 2013.

[27] Anita A Harteveld et al. “Data on vessel wall thickness measurements of intracranial arteries derived from human circle of Willis specimens”. In: *Data in brief* 19 (2018), pp. 6–12.

[28] Y Tardy et al. “Non-invasive estimate of the mechanical properties of peripheral arteries from ultrasonic and photoplethysmographic measurements”. In: *Clinical Physics and Physiological Measurement* 12.1 (1991), p. 39.

[29] Anton Sidawy. “Rutherford’s Vascular Surgery and Endovascular Therapy”. In: *Journal of vascular surgery* 68.5 (2018), pp. 1611–1612.

[30] Gerard J Tortora and Bryan H Derrickson. *Principles of anatomy and physiology*. John Wiley & Sons, 2018.

[31] N Stergiopulos, J -J Meister, and N Westerhof. “Simple and accurate way for estimating total and segmental arterial compliance: the pulse pressure method”. In: *Annals of biomedical engineering* 22 (1994), pp. 392–397.

[32] Li John Kj. *Dynamics of the vascular system*. Vol. 1. World scientific, 2004.

[33] Patrick Segers et al. “Assessment of distributed arterial network models”. In: *Medical and Biological Engineering and Computing* 35 (1997), pp. 729–736.

[34] Ansaar T Rai et al. “Cerebrovascular geometry in the anterior circulation: an analysis of diameter, length and the vessel taper”. In: *Journal of neurointerventional surgery* 5.4 (2013), pp. 371–375.

[35] Charles S Peskin. “Flow patterns around heart valves: a numerical method”. In: *Journal of computational physics* 10.2 (1972), pp. 252–271.

[36] John KJ Li. *The arterial circulation: physical principles and clinical applications*. 3rd ed. Springer Science Business Media, 2000.

[37] Vanessa Dıaz-Zuccarini and Jacques LeFèvre. “An energetically coherent lumped parameter model of the left ventricle specially developed for educational purposes”. In: *Computers in biology and medicine* 37.6 (2007), pp. 774–784.

[38] Gary Drzewiecki et al. “Modeling of mechanical dysfunction in regional stunned myocardium of the left ventricle”. In: *IEEE transactions on biomedical engineering* 43.12 (1996), pp. 1151–1163.

[39] Jerry F Green and Nicholas C Miller. “A model describing the response of the circulatory system to acceleration stress”. In: *Annals of Biomedical Engineering* 1.4 (1973), pp. 455–467.

[40] David S Berger and JK-J Li. "Temporal relationship between left ventricular and arterial system elastances". In: *IEEE transactions on biomedical engineering* 39.4 (1992), pp. 404–410.

[41] Silvio Cavalcanti and Enzo Belardinelli. "Modeling of cardiovascular variability using a differential delay equation". In: *IEEE Transactions on biomedical engineering* 43.10 (1996), pp. 982–989.

[42] Thomas Heldt et al. "Computational modeling of cardiovascular response to orthostatic stress". In: *Journal of applied physiology* 92.3 (2002), pp. 1239–1254.

[43] GIANCARLO Pennati, M Bellotti, and R Fumero. "Mathematical modelling of the human foetal cardiovascular system based on Doppler ultrasound data". In: *Medical engineering & physics* 19.4 (1997), pp. 327–335.

[44] K Lu et al. "A human cardiopulmonary system model applied to the analysis of the Valsalva maneuver". In: *American Journal of Physiology-Heart and Circulatory Physiology* 281.6 (2001), H2661–H2679.

[45] Jon B Olansen et al. "A closed-loop model of the canine cardiovascular system that includes ventricular interaction". In: *Computers and biomedical research* 33.4 (2000), pp. 260–295.

[46] Ying Sun et al. "A comprehensive model for right-left heart interaction under the influence of pericardium and baroreflex". In: *American Journal of Physiology-Heart and Circulatory Physiology* 272.3 (1997), H1499–H1515.

[47] Mauro Ursino and Elisa Magosso. "Role of short-term cardiovascular regulation in heart period variability: a modeling study". In: *American Journal of Physiology-Heart and Circulatory Physiology* 284.4 (2003), H1479–H1493.

[48] Mauro Ursino and Carlo Alberto Lodi. "A simple mathematical model of the interaction between intracranial pressure and cerebral hemodynamics". In: *Journal of Applied Physiology* 82.4 (1997), pp. 1256–1269.

[49] Mauro Ursino and Elisa Magosso. "Acute cardiovascular response to isocapnic hypoxia. I. A mathematical model". In: *American Journal of Physiology-Heart and Circulatory Physiology* 279.1 (2000), H149–H165.

[50] D Elad et al. "Numerical schemes for unsteady fluid flow through collapsible tubes". In: *Journal of biomedical engineering* 13.1 (1991), pp. 10–18.

[51] WE Bodley. "The non-linearities of arterial blood flow". In: *Physics in Medicine & Biology* 16.4 (1971), p. 663.

[52] JJ Wang and KH Parker. "Wave propagation in a model of the arterial circulation". In: *Journal of biomechanics* 37.4 (2004), pp. 457–470.

[53] J Lee and N Smith. "Development and application of a one-dimensional blood flow model for microvascular networks". In: *Proceedings of the Institution of Mechanical Engineers, Part H: Journal of Engineering in Medicine* 222.4 (2008), pp. 487–511.

[54] Spencer J Sherwin et al. "Computational modelling of 1D blood flow with variable mechanical properties and its application to the simulation of wave propagation in the human arterial system". In: *International journal for numerical methods in fluids* 43.6-7 (2003), pp. 673–700.

[55] Irina Surovtsova. "Effects of compliance mismatch on blood flow in an artery with endovascular prosthesis". In: *Journal of biomechanics* 38.10 (2005), pp. 2078–2086.

[56] N Stergiopulos, DF Young, and TR Rogge. "Computer simulation of arterial flow with applications to arterial and aortic stenoses". In: *Journal of biomechanics* 25.12 (1992), pp. 1477–1488.

[57] James B Bassingthwaighte, Larry S Liebovitch, and Bruce J West. *Fractal physiology*. Springer, 2013.

[58] M Zamir. "Nonsymmetrical bifurcations in arterial branching." In: *The Journal of general physiology* 72.6 (1978), pp. 837–845.

[59] Cecil D Murray. "The physiological principle of minimum work: I. The vascular system and the cost of blood volume". In: *Proceedings of the National Academy of Sciences* 12.3 (1926), pp. 207–214.

[60] HB Atabek and HS Lew. "Wave propagation through a viscous incompressible fluid contained in an initially stressed elastic tube". In: *Biophysical Journal* 6.4 (1966), pp. 481–503.

[61] HB Atabek. "Wave propagation through a viscous fluid contained in a tethered, initially stressed, orthotropic elastic tube". In: *Biophysical journal* 8.5 (1968), pp. 626–649.

[62] John R Womersley. *An elastic tube theory of pulse transmission and oscillatory flow in mammalian arteries*. 614. Wright Air Development Center, 1957.

[63] Mitchel J Colebank et al. "A multiscale model of vascular function in chronic thromboembolic pulmonary hypertension". In: *American Journal of Physiology-Heart and Circulatory Physiology* 321.2 (2021), H318–H338.

[64] John R Womersley. "Method for the calculation of velocity, rate of flow and viscous drag in arteries when the pressure gradient is known". In: *The Journal of physiology* 127.3 (1955), p. 553.

[65] Maxwell Lewis Neal and Roy Kerckhoffs. "Current progress in patient-specific modeling". In: *Briefings in bioinformatics* 11.1 (2010), pp. 111–126.

[66] Jennifer A Moore et al. "Computational blood flow modeling based on in vivo measurements". In: *Annals of biomedical engineering* 27 (1999), pp. 627–640.

[67] Charles A Taylor et al. "Predictive medicine: computational techniques in therapeutic decision-making". In: *Computer Aided Surgery: Official Journal of the International Society for Computer Aided Surgery (ISCAS)* 4.5 (1999), pp. 231–247.

[68] Charles A Taylor, Thomas JR Hughes, and Christopher K Zarins. "Finite element modeling of blood flow in arteries". In: *Computer methods in applied mechanics and engineering* 158.1-2 (1998), pp. 155–196.

[69] Frank JH Gijsen et al. "A new imaging technique to study 3-D plaque and shear stress distribution in human coronary artery bifurcations in vivo". In: *Journal of biomechanics* 40.11 (2007), pp. 2349–2357.

[70] Beverly T Tang et al. "Abdominal aortic hemodynamics in young healthy adults at rest and during lower limb exercise: quantification using image-based computer modeling". In: *American Journal of Physiology-Heart and Circulatory Physiology* 291.2 (2006), H668–H676.

[71] David A Vorp. "Biomechanics of abdominal aortic aneurysm". In: *Journal of biomechanics* 40.9 (2007), pp. 1887–1902.

[72] S Malatos, A Raptis, and M Xenos. "Advances in low-dimensional mathematical modeling of the human cardiovascular system". In: *J Hypertens Manag* 2.2 (2016), pp. 1–10.

[73] Andriy Fedorov et al. "3D Slicer as an image computing platform for the Quantitative Imaging Network". In: *Magnetic resonance imaging* 30.9 (2012), pp. 1323–1341.

[74] Luca Antiga et al. "An image-based modeling framework for patient-specific computational hemodynamics". In: *Medical & biological engineering & computing* 46 (2008), pp. 1097–1112.

[75] G Porenta, DF Young, and TR Rogge. "A finite-element model of blood flow in arteries including taper, branches, and obstructions". In: (1986).

[76] Philippe Reymond et al. "Validation of a one-dimensional model of the systemic arterial tree". In: *American Journal of Physiology-Heart and Circulatory Physiology* 297.1 (2009), H208–H222.

[77] Kim H Parker and CJH Jones. "Forward and backward running waves in the arteries: analysis using the method of characteristics". In: (1990).

[78] Kim H Parker. "An introduction to wave intensity analysis". In: *Medical & biological engineering & computing* 47 (2009), pp. 175–188.

[79] AW Khir and KH Parker. "Wave intensity in the ascending aorta: effects of arterial occlusion". In: *Journal of biomechanics* 38.4 (2005), pp. 647–655.

[80] Robert A Bleasdale et al. "Wave intensity analysis from the common carotid artery: a new noninvasive index of cerebral vasomotor tone". In: *Heart and vessels* 18 (2003), pp. 202–206.

[81] Yi-Hui Sun et al. "Wave-intensity analysis: a new approach to coronary hemodynamics". In: *Journal of applied physiology* 89.4 (2000), pp. 1636–1644.

[82] Ellen H Hollander et al. "Negative wave reflections in pulmonary arteries". In: *American Journal of Physiology-Heart and Circulatory Physiology* 281.2 (2001), H895–H902.

[83] Masaki Nie et al. "Helium inhalation enhances vasodilator effect of inhaled nitric oxide on pulmonary vessels in hypoxic dogs". In: *American Journal of Physiology-Heart and Circulatory Physiology* 280.4 (2001), H1875–H1881.

[84] David Bessems, Marcel Rutten, and Frans Van De Vosse. "A wave propagation model of blood flow in large vessels using an approximate velocity profile function". In: *Journal of Fluid Mechanics* 580 (2007), pp. 145–168.

[85] N Westerhof et al. "Forward and backward waves in the arterial system". In: *Cardiovascular research* 6.6 (1972), pp. 648–656.

[86] Warfarin-Aspirin Symptomatic Intracranial Disease (WASID) Study Group et al. "Prognosis of patients with symptomatic vertebral or basilar artery stenosis". In: *Stroke* 29 (1998), pp. 1389–1392.

[87] EC/IC Bypass Study Group*. "Failure of extracranial–intracranial arterial bypass to reduce the risk of ischemic stroke: results of an international randomized trial". In: *New England Journal of Medicine* 313.19 (1985), pp. 1191–1200.

[88] Leo N Hopkins et al. "Vertebrobasilar insufficiency: part 2: microsurgical treatment of intracranial vertebrobasilar disease". In: *Journal of neurosurgery* 66.5 (1987), pp. 662–674.

[89] J Bogousslavsky et al. "Atherosclerotic disease of the middle cerebral artery." In: *Stroke* 17.6 (1986), pp. 1112–1120.

[90] LR Caplan, PB Gorelick, and DB Hier. "Race, sex and occlusive cerebrovascular disease: a review." In: *Stroke* 17.4 (1986), pp. 648–655.

[91] Lindsay Symon, Susumu Ishikawa, and John S Meyer. "Cerebral arterial pressure changes and development of leptomeningeal collateral circulation". In: *Neurology* 13.3 (1963), pp. 237–237.

[92] Soonchan Park et al. "Computational modeling with fluid-structure interaction of the severe m1 stenosis before and after stenting". In: *Neurointervention* 8.1 (2013), pp. 23–28.

[93] Linfang Lan et al. "Sustaining cerebral perfusion in intracranial atherosclerotic stenosis: the roles of antegrade residual flow and leptomeningeal collateral flow". In: *Journal of Cerebral Blood Flow & Metabolism* 40.1 (2020), pp. 126–134.

[94] Donald F Young and Frank Y Tsai. "Flow characteristics in models of arterial stenoses—II. Unsteady flow". In: *Journal of biomechanics* 6.5 (1973), pp. 547–559.

[95] Colin Clark. "The fluid mechanics of aortic stenosis—I. Theory and steady flow experiments". In: *Journal of biomechanics* 9.8 (1976), pp. 521–528.

[96] K Lance Gould. "Noninvasive assessment of coronary stenoses by myocardial perfusion imaging during pharmacologie coronary vasodilatation: I. Physiologic basis and experimental validation". In: *The American journal of cardiology* 41.2 (1978), pp. 267–278.

[97] Fuyou Liang et al. "A computational model study of the influence of the anatomy of the circle of Willis on cerebral hyperperfusion following carotid artery surgery". In: *Biomedical engineering online* 10 (2011), pp. 1–22.

[98] Wei-Jian Jiang et al. "Angioplasty and stenting". In: *Intracranial Atherosclerosis* (2008), pp. 181–193.

[99] Wei-Jian Jiang et al. "Stenting of symptomatic M1 stenosis of middle cerebral artery: an initial experience of 40 patients". In: *Stroke* 35.6 (2004), pp. 1375–1380.

[100] Jessica J Steventon et al. "Cerebrovascular function in the large arteries is maintained following moderate intensity exercise". In: *Frontiers in Physiology* 9 (2018), p. 1657.

[101] Kevin S Heffernan et al. "Arterial stiffness and cerebral hemodynamic pulsatility during cognitive engagement in younger and older adults". In: *Experimental Gerontology* 101 (2018), pp. 54–62.